Image Analysis of Cardiac Computed Tomography Towards Regional Functional Analysis

Michael Weiseng Tee

Christ Church

University of Oxford

A thesis submitted for the degree of

Doctor of Philosophy

Trinity 2015

I dedicate this to my mum and dad.

Acknowledgements

I would like to firstly thank my supervisors Professor J. Alison Noble, DPhil at the University of Oxford, UK and Professor David A. Bluemke MD PhD at the National Institutes of Health (NIH) in Washington DC, USA. I am eternally grateful for their support, mentorship and thoughtful guidance. It has been an honour to work with them and look forward to long lasting friendship with them both.

I would also like to thanks to all my colleagues whose support and involvement has been invaluable. This includes but is not limited to Ken Wong, Marcus Chen, Jack Yao, Joao Lima, Al Lardo, Craig Emter, Davis Vigneault, Richard Stebbing, Joao Domingos, Sana Fathima, Chris Bridge, John McMingle, Ana Namburete, Viet Sandfort, Marissa Mallek, Harry Griffin, Andrew Sams, Cynthia Davies-Venn, Mark Ahlman, Selwaness, Mariana Selwaness, Rob Evers, Chia-Ying Liu, Fabio Ramans, Colin Yi, Samuel Won, and everyone else I failed to mention from the United States and the United Kingdom. Sincere thanks are also due to Professor Vicente Grau at the University of Oxford and Professor Albert de Roos for agreeing to be the examiners of this thesis. I am inspired by their work and deeply appreciate their time.

I would also like to acknowledge the programs and training grants which have supported me pursuing my interest in medicine and science including: the National Institutes of Health (Intramural Training Research Fellowship), Oxford University (Oxford-Cambridge Fellowship), Case Western Reserve University (Medical Scientist Training Program grant), and Cleveland Clinic Lerner College of Medicine. In particular I would like to thank Dr. Kathleen Franco, Dean James Young, Professor Cliff Harding, Professor George Dubyak, Dr. Craig Blackstone, Dr. Richard Siegel, and Dr. Michael Lenardo who first made this possible.

Finally, I want to acknowledge my friends and family. The friends I have made through OXCAM, CCLCM, Case Western Reserve University, the University of Oxford and the NIH and who have become part of my life in one form or another have deeply shaped the individual I am today and have brought my life so much joy. I wish to acknowledge my family (William Tee, Mary Lim, Jason Tee, and Thomas Tee) whose loving support and encouragement has been the foundation from which I have been able to pursue my ambitions. This thesis and all the happiness behind it is theirs as well as mine.

Statement of Originality

The work presented herein was performed by me and in no way forms part of another thesis from this or any other university. Contributions made by others have been acknowledged. This work was performed under the supervision of Professor J Alison Noble within the Institute of Bio-medical Engineering under the Division of Medical Sciences at the University of Oxford and Professor David A. Bluemke of the National Institutes of Health.

Michael W Tee,

Oxford University

Trinity Term 2015

Abstract

Global assessment of myocardial function is widely performed by estimating ejection fraction (EF), but many common cardiac diseases initially affect the myocardium on a regional, rather than global, basis. Computed tomography (CT), most commonly applied to assess the coronary arteries, is a prime candidate for such regional analysis. This doctoral thesis makes steps towards regional CT functional analysis with two clinical and two technical contributions.

The first clinical contribution focuses on evaluating the feasibility and utility of functional analysis with currently available CT technology. Our study found that CT strain analysis could identify regional wall motion abnormalities in cardiomyopathy that are not otherwise detected using conventional metrics of myocardial function such as EF.

In order for cine CT of the heart to become routine clinical practice, improvements need to be made to the image acquisition protocol. The second clinical contribution focus on making these improvements with results pointing to the possibility of one millisievert range cine CT images with high (<50 milliseconds) temporal resolutions.

Moving to technical considerations, a key concern has been how to better characterise the myocardium in CT. To address this, the first technical contribution examines the use of feature-based attribute vectors, which were found to improve image registration towards deriving more reliable motion estimations.

The second technical contribution focus on developing a pipeline tailored towards CT strain analysis. Noting that CT naturally provides information in 3D, a 3D hyperelastic biomechanical model fitting method was evaluated. Analysis of an infarction model demonstrated that regional myocardial strain can be estimated in the 3D space and areas of infarction can be detected.

By considering both technical and clinical perspectives, these advances will contribute to the the field of regional cardiac functional analysis towards improving patient care.

Contents

List of Figures

List of Tables

List of Abbreviations

1D, 2D, 3D . One-, Two-, or Three-Dimensional, referring in this thesis to spatial dimensions in an image.

2D+t, 3D+t Two or Three spatial Dimensions plus a Time dimension, i.e. a temporal sequence of 2-D or 3-D images.

AEC . . . . . Automatic Exposure Control, a technique that performs automatic modulation of the tube current in CT.

AIDR3D . . . Adaptive Iterative Dose Reduction 3D Reconstruction, iterative reconstruction algorithm that works in both raw data and image data space to improve image quality

AHA . . . . . American Health Association, is a non-profit organization in the United States that fosters appropriate cardiac care in an effort to reduce disability and deaths caused by cardiovascular disease and stroke. Provides research funding and guidelines.

AP . . . . . Anterior-Posterior, referring to a direction in the patient of a CT scan.

ARVD . . . . Arrhythmogenic right ventricular dysplasia, an nonischemic inherited cardiomyopathy characterised by hypokinetic areas of the free wall of the RV, fibrofatty replacement of the RV myocardium, and is associated with arrhythmias originating in the RV.

ASE . . . . . American Society of Echocardiography, a professional organization of physicians, cardiac sonographers, nurses and scientists involved in echocardiography providing research grants and guidelines.

AUC . . . . . Area Under Curve, a measure of classifier accuracy obtained via ROC curves.

AVI . . . . . Audio Video Interleaved, a multimedia container format.

BMI . . . . . Body Mass Index, a numerical computation regarding height and weight used as a proxy for body fat percentage.

CAD . . . . . Coronary Artery Disease, diseases caused by a slow build up of fatty deposits on the inner wall of the blood vessels that supply the heart muscle with blood. Includes stable angina, unstable angina, myocardial infarction, and sudden coronary death

CT . . . . . Computed Tomography, imaging modality based on X-rays, subject of Appendix A.

CCT . . . . . Cardiac Computed Tomography, referring to any CT imaging done for the purpose of cardiac examination.

CMR . . . . . Cardiac Magnetic Resonance, referring to any MR imaging done for the purpose of cardiac examination.

CNR . . . . . Contrast-to-Noise Ratio, a measure of image quality.

CRT . . . . . Cardiac Resynchronization Therapy , sometimes called biventricular pacing, a therapy in which a small electrical impulses is sent to both lower chambers of the heart to help them beat together in a more synchronized pattern as a treatment for HF.

CSPAMM . . Complementary SPAtial Modulation of Magnetization, an extension to SPAMM to better handle tag line fading during diastole.

DANTE . . . Delays Alternating with Nutations for Transient Excitation, a segmented k-space gradient echo pulse sequences used to create MR tag lines. Alternative to SPAMM.

DENSE . . . Displacement ENcoding with Stimulated Echoes, a functional CMR pulse sequence used to create maps of myocardial displacement with high resolution.

DLP . . . . . Dose-Length Product, product of the $CTDI_{vol}$ and the scan length for a group of CT scans. This number can be summed over the entire exam to give an estimate of the total radiation dose.

EACVI . . . . European Association of CardioVascular Imaging, a key society dedicated to cardiovascular imaging in Europe.

ECG . . . . . ElectroCardioGraphy, the process of recording the electrical activity of the heart.

EF . . . . . Ejection Fraction, a measurement of the percentage of blood leaving your heart each contraction.

EDV . . . . . End Diastolic Volume, the volume of the heart chamber during diastole.

ESV . . . . . End Systolic Volume, the volume of the heart chamber during systole.

FA . . . . . Feature Asymmetry, a metric based on the monogenic signal for better detection of edges in images.

FE . . . . . Finite Element,a numerical method for approximating solutions to boundary value problems for partial differential equations.

HARP . . . . Harmonic Phase, a medical image analysis technique capable of extracting and processing motion information from tagged MR.

HF . . . . . Heart Failure, general term applied when the heart is unable to pump sufficiently to maintain blood flow to meet the needs of the body.

HFpEF . . . . Heart Failure with preserved Ejection Fraction, a term to describe the manifestation of signs and symptoms of HF with an Ejection Fraction greater than 55%.

HOCM . . . . Hypertrophic Obstructive CardioMyopathy, a disease in which the heart muscle (myocardium) becomes abnormally thick (hypertrophied).

HR . . . . . Heart Rate, a metric of how frequent the heart pumps per unit time (most often in terms of minutes).

HU . . . . . Hounsfield Unit, a linear transformation of the original linear attenuation coefficient measurement.

LGE . . . . . Late Gadolinium-Enhanced, an MR protocol that involves acquiring an image minutes after contrast injection in order to visualise myocardial fibrosis.

LOSO . . . . Leave-One-Subject-Out, a cross validation method useful in the case of small datasets.

LV . . . . . Left Ventricle, one of the four cardiac chambers.

LVRWM . . . Left Ventricular Regional Wall Movement, a visual scale for quantifying difference in heart motion.

MDCT . . . . MultiDetector Computed Tomography, refers to CT scanners where there a 2D array of detector elements allows for volume acquisitions.

MESA . . . . Multi-Ethnic Study of Atherosclerosis, a medical research study involving more than 6,000 men and women from six communities in the United States.

MR . . . . . Magnetic Resonance, a imaging modality based on the use of magnetic fields and radio waves.

MTT . . . . . Multimodality Tissue Tracking, a software (Toshiba, v.6.0, Tokyo, Japan) for regional strain calculation based on feature tracking.

PC . . . . . Phase-Contrast, a MR technique directly encoding regional velocity by manipulating the phase of the magnetization.

ROI . . . . . Region Of Interest, a selected subset of samples or areas within a dataset identified for a particular purpose.

ROC . . . . . Receiver Operating Characteristic curve, a representation of classifier performance over a range of threshold values.

RV . . . . . Right Ventricle, one of the four cardiac chambers.

SAX . . . . . Short AXis view, a cardiac view that displays cross-sections of the LV and RV.

SCMR . . . . Society for Cardiovascular Magnetic Resonance, an international non-profit medical society focused on CMR imaging to improve patient outcomes through education, training, standards, research and development.

SENC . . . . Strain-ENCoding, a technique directly encoding regional strain of the heart into the acquired MR images.

SNR . . . . . Signal-to-Noise Ratio, a measure of image quality.

SPAMM . . . SPAtial Modulation of Magnetization, a segmented k-space gradient echo pulse sequences used to create MR tag lines. Alternative to DANTE.

SQUEEZ . . Stretch QUantifier for Endocardial Engraved Zones), an algorithm which allows evaluation of endocardial deformation designed for CT analysis.

SR . . . . . Strain Rate, the first derivative of strain in respect to time, and is a metric for the rate of change in strain of a material.

SSDE . . . . . Size Specific Dose Estimate, a new metric of radiation dose which accounts for patient size and is calculated from console-displayed $CTDI_{vol}$.

SSFP . . . . . Steady State Free Precession, a type of gradient echo MR pulse sequence in which a steady, residual transverse magnetisation is maintained between successive cycles often used for its superiority cine assessment of cardiac function.

TDI . . . . . Tissue Doppler Imaging, a echocardiographic technique that uses Doppler principles to measure the velocity of myocardial motion.

TTE . . . . . Trans-Thoracic Echocardiography, the use of an ultrasound transducer placed on the external. chest wall

TTC . . . . . TriphenylTetrazolin-Chloride, a staining agent used in histology to detect infarction. Specifically, a redox indicator whose presence indicates cellular respiration.

"If the hand be held between the discharge-tube and the screen, the darker shadow of the bones is seen within the slightly dark shadow-image of the hand itself... For brevity's sake I shall use the expression 'rays'; and to distinguish them from others of this name I shall call them 'X-rays'." Discovery of a new kind of radiation, named it X-ray.

—Wilhelm Rontgen, 1895

1 Introduction

Contents

1.1 Motivation

The primary objective of this thesis is to improve cardiac computed tomography (CCT) imaging capabilities in order to diagnose cardiac diseases earlier and to monitor medical therapies. Today, CCT is used mainly for calculating stenosis for stent placement and is an established technology for assessing coronary heart disease (5). CCT technology continues to develop with reductions in radiation dosing requirements and improvements in image resolution. With

these improvements, cardiologists and radiologists agree that a great abundance of clinically relevant information has yet to be tapped into with this modality.

One specific area of interest has been quantifying regional motion of the heart. With the understanding that regional changes in the heart precede changes in global metrics of function, using regional information can detect cardiac disease long before the need for expensive and highly invasive surgeries and treatments. Our mission is to take steps towards enabling CCT technology to quantify these regional functional changes that occur earlier in the disease process.

My role entailed developing and executing a strategy to achieve this goal, which I approached from both a clinical and technical perspective.

1.2 Contribution

The contributions made in this thesis can be broken down into clinical contributions and technical contributions. In this section, I provide a brief introduction to the two clinical contributions (chapters 4 and 5) and then the two technical contributions (chapters 6 and 7).

In **chapter 4**, we evaluate the feasibility for strain analysis in CCT towards detecting subtle disease in cases of normal ejection fraction (EF). At the moment, strain analysis is mainly done with ultrasound and cardiac magnetic resonance (CMR), however this chapter shows the potential of functional analysis with CCT as well.

In **chapter 5**, we develop an image acquisition protocol with a low radiation dose. This has led to an improved imaging protocol that allows for one mSv range cine CT images with high temporal resolution to be acquired.

In **chapter 6**, we develop a method to characterise myocardial tissue deformation in two dimensional images. We specifically evaluate the potential use of feature-based attribute vectors to better characterise pixels for image registration or tracking in CCT.

In **chapter 7**, we focus on development of an image processing pipeline enabling the use of cardiac modelling towards 3D CCT functional analysis. We examine a pipeline incorporating a deformable 3D biomechanical model that accounts for the hyperelastic properties of the heart.

1.3 Thesis Structure

Given the multi-disciplinary nature of this work, this thesis was written to appeal to both a clinical and engineering focused audience. Therefore, explanations have been given to keep both audiences informed. Further explanations can be found in the appendices.

Chapter 1 provides the motivation and context of this work, and outlines the structure of the rest of the thesis. This chapter also provides a list of prior publications and presentations given during the course of this doctoral training.

Chapter 2 provides a clinical review specifically introducing cardiovascular disease, global and regional clinic metrics of disease, functional cardiac imaging, cardiac strain, and comparisons between the modalities currently used for strain analysis.

Chapter 3 provides a technical review of the field of cardiac strain imaging, examining the main technical methodologies currently implemented in echocardiology, CMR, and CCT. In each of these modalities there is emphasis made in the introduction on the particular technique of interest related to regional analysis. For echocardiography that is speckle tracking (6). For CMR, it is tagged MR (7). And for CCT, it is SQUEEZ analysis (8).

Chapter 4 and **chapter 5** consist of the clinical research component of this thesis. The overarching goal of these chapters is to explore the clinical use and capabilities of functional analysis with CCT. They are therefore structured as clinical papers, with each chapter broken down into an introduction, methods, results and discussion section. In the clinical chapters, the introduction and methods focuses more on the clinical aspects of the research. For **chapter 4**, as

we investigate the potential clinical utility of strain analysis in Multidetector computed tomography (MDCT), we first provide an overview of the clinical utility of strain analysis in the introduction. In the methods of this chapter, there is a focus on the user level image analysis steps. For **chapter 5**, we focus on the image acquisition process in CT. Therefore in the introduction we review the key variable to consider when designing a CT image acquisition protocol and in the methods we go over the specific decisions we made in order to achieve our goal of low radiation dose and high temporal resolution cine CT images.

Chapter 6 and **chapter 7** describe the technical research contributions. These chapters' overarching goal is the development of an image processing methodology pipeline tailored for functional CCT analysis. Therefore, these chapters are structured as technical papers with more emphasis placed on the image processing methods used. Each chapter can generally be broken down into an introduction, experimental data, methods, results and discussion section. It is necessary to have a separate experimental data section and methods section as the focus in the method sections are the technical details of the method. **Chapter 6** summarises the potential different methods for motion estimation that could be pursued when we decided to focus on dense tracking via non-rigid registration. In this registration process we decided to focus on the goal of tissue characterisation in CCT via feature-based attribute vectors. The method section goes into the detail of feature-based attribute vectors. Finally, in **chapter 7**, the focus moves to deformable models where we introduce them and their current use. In the methods we go into the specific details of our method of a hyperelastic biomedical model towards strain quantification.

Chapter 8 consolidates and puts into context all the contributions of the thesis. Building off the experience and knowledge we have developed through the doctoral research, **chapter 9** forms predictions for the field as well as points to key areas of further work towards improving patient care.

1.4 Originality and Individual Role

The nature of the field and work meant that much of the work was collaborative. In general I was involved with developing, planning and executing the research described in each chapter. Details about the roles of collaborators for each contribution is listed below:

Chapter 4: This work involved the contribution of a multidisciplinary team of physicians, nurses, and technicians. I led this study and was involved with multiple aspects of the project. Cynthia Davies-Venn, Colin Yi, Fabio Raman, Song Tao Liu, Al Lardo, and Craig Emter were involved in the animal preparation and imaging. Samuel Won, a post-baccalaureate student, performed the histological analysis of fibrosis. Davis Vigneault and Fabio Raman assisted in the tagged MR images analysis. J. Alison Noble, Joao Lima, Craig Emter and David A. Bluemke all provided guiding input into this work.

Chapter 5: This work involved the contribution of a multidisciplinary team of physicians, nurses, and technicians. I led the project and was involved with multiple aspects of the study. Colin Yi (post-baccalaureate student) assisted in measurements for SNR and CNR reporting. Marissa Mallek and Andrew Sams (registered nurses) assisted with patient recruiting and scheduling. Veit Sandfort, J. Alison Noble, Marcus Y. Chen, and David A. Bluemke all provided guiding input into this work.

Chapter 6: This work involved the contribution of a number of individuals. The test dataset was provided by David A. Bluemke. I led this project and was involved with multiple aspects of the study including study design, programming implementation, and evaluation. Sana Fathima provided assistance with troubleshooting and programming for this work. J. Alison Noble, and David A. Bluemke provided guiding input into this work.

Chapter 7: This work involved the contribution of a number of individuals. Ken Wong and I led the development and implementation of this research. The dataset was provided by Marcus Chen. Ken Wong led the programming for

this work. Jack Yao, J. Alison Noble, and David A. Bluemke provided guiding input into this work.

1.5 Prior Publications

Below is my list of publications and presentations related to the thesis at the time of the thesis submission. It includes publications and presentations that are not directly part of this thesis but occurred or were produced during the course of the doctorate training.

1.5.1 Publications:

- (Writing) Feasibility of whole heart one mSv range high temporal resolution (50msec) cardiac function CT: 320 row detector. 2015
- (Writing) N-Dimensional Phase Unwrapping. ITK Insight. 2015
- (Accepted) Computed-Aided Infarction Identification from Cardiac CT Images: A Biomechanical Approach with SVM. MICCAI. 2015
- (Accepted) Normal values for cardiac magnetic resonance (CMR) imaging in adults and children. Journal of Cardiac Magnetic Resonance. 2014
- (Published) Myocardial strain estimation from CT: towards computer-aided diagnosis on infarction identification. Proc. SPIE 9414, Medical Imaging 2015: Computer-Aided Diagnosis, 941434 (March 20, 2015)
- (Published) Regional Strain Analysis with Multidetector CT in a Swine Cardiomyopathy Model: Relationship to Cardiac MR Tagging and Myocardial Fibrosis. Radiology. 2015 Apr 8:142339.
- (Published) The association between cardiovascular risk and cardiovascular magnetic resonance measures of fibrosis: the Multi-Ethnic Study of Atherosclerosis (MESA). J Cardiovasc Magn Reson. 2015 Feb 12;17(1):15.

- (Published) Imaging Techniques for Cardiac Strain and Deformation: comparison of Echocardiography, Cardiac Magnetic Resonance and Cardiac Computed Tomography, Expert Review of Cardiovascular Therapy, Feb;11(2):221-31.

- (Published) Application of Feature-Based Attribute Vectors for Improved Image Registration Towards Cardiac Motion Estimation in Cardiac Computed Tomography. Proceedings of Medical Image Understanding and Analysis. July 2013

1.5.2 Presentations Given:

Conference Oral Presentations

- 27 Nov- 2 Dec 2014 Radiological Society of North America (RSNA)

- 23-24 Jun 2014 NIH Oxford Cambridge (OxCam) and Medical Scientist Training Program (MSTP) Colloquium

- 27 Nov- 2 Dec 2011 Radiological Society of North America (RSNA)

Conference Poster Presentations

- 3-8 Mar 2015 European Society of Radiology (ESR)

- 17-19 Apr 2013 Medical Image Understanding and Analysis (MIUA)

- 3-7 Nov 2012 American Heart Association (AHA)

- 23-24 Jun 2012 NIH Oxford Cambridge (OxCam) and Medical Scientist Training Program (MSTP) Colloquium

- 15 Sept 2012 Oxford Imaging Festival

- 2-6 Oct 2011 - American Society of Radiation Oncology (ASTRO)

"Integriert man eine geeigneten Regularitatsbegingungen unterworfene Funktion zweier Veranderlichen X,y..." . Developed and published the mathematical foundations for reconstructing cross sectional images from transmission data providing a solution to the inverse problem of reconstruction.

—Johann Radon, 1917 (9)

2 Clinical Background

Contents

2.1 Introduction

This chapter's purpose is to provide some of the clinical background of this thesis in terms of the clinical need for regional strain analysis, clinically useful definition of strain, and to compare the main clinically used modalities for

such analysis. Specifically, we will introduce disease burden of cardiovascular disease, functional cardiac imaging as a means to address this issue, regional functional analysis, definition of strain, and comparison between the modalities currently used for strain analysis.

2.2 Disease Burden of Cardiac Disease:

Cardiovascular disease is the cause of one in four deaths worldwide (10). It has become evident that cardiovascular disease has been and continues to be a major issue with an increase of 31.2% in the number of deaths caused between 1990 and 2010. During this time frame, the most significant changes within this category were a 34.9% increase in deaths caused by ischemic heart disease, a 40.8% increase in deaths caused by cardiomyopathy and myocarditis, a 233.9% increase in deaths caused by atrial fibrillation and flutter, and a 34.8% increase in deaths caused by endocarditis to name a few (10). Although improvement in treatments has greatly helped with mortality rates, morbidity and cost to society remain high (11). In the face of such a large disease burden, there has been increased interest in earlier detection, prevention and treatment of cardiovascular disease, with a large component of this effort being in imaging.

2.3 Functional Cardiac Imaging

The heart is a highly specialized muscle, and assessment of its ability to contract and circulate blood would provide a fundamental measure of cardiac health. Measurement of left ventricular (LV) myocardial function often defines the extent and severity of myocardial disease. Because of this, a number of metrics have been developed to quantify myocardial function, including chamber areas, chamber volumes, peak flow velocity, and EF (12; 13; 14; 15).

2.3.1 Beyond Ejection Fraction and Towards Regional Analysis

The most frequently used clinical measure of myocardial function is EF, which measures *global* myocardial function defined as the change in volume of blood in the LV cavity, relative to the end diastolic volume (16). It is calculated as follows:

$$EF = \frac{EDV - ESV}{EDV} \tag{2.1}$$

where EF is ejection fraction, EDV is end distolic volume, and ESV is end systolic volume.

A reduction in EF is particularly ominous in systolic heart failure (HF), or following myocardial infarction. 30-40% of patients with heart failure with preserved ejection fraction (HFpEF) (17). Thus, in one of the most common causes of HF, EF does not always characterise the extent of disease. In large scale population trials, EF has also been recognized to lack predictive value in the subsequent development of cardiovascular events (18; 19). Given the near universal reporting of EF in clinical cardiology, this contradiction is quite striking.

A fundamental tenant of functional analysis of myocardial disease is that *regional* changes precede *global* changes. Many cardiac disorders do not affect cardiac function uniformly but affect the heart regionally. For instance, coronary artery disease, the most common cardiac condition, is a regional disorder that affects some territories of the heart more than others. Other common non-ischemic diseases of the myocardium are also frequently regional, such as septal forms of hypertrophic cardiomyopathy (HOCM). Even most nonseptal forms of HOCM are affects the heart regionally. Therefore, global measures such as EF may not be sensitive enough to capture these more localized changes. This has led to increased interest in indices that measure the local, or regional, degree of myocardial function.

2.4 Regional Myocardial Function

Relatively straightforward measures such as regional wall thickening (20) may be used to measure function. However, there is increasing interest in the use of regional myocardial strain, a multi-dimensional unitless measure of deformation, which can potentially better account for different heart sizes. Regional cardiac strain (i.e., deformation of the heart normalised to end diastole) of both systolic and diastolic function has the has been shown to capture subtle alterations that result from early disease of the myocardium.

2.5 Cardiac Strain

There are two established methods for assessing deformation: Lagrangian and Eularian strain. In order to understand the difference between these two, it is helpful to also consider strain rate (SR), which describes the rate of deformation.

Lagrangian strain (21) uses a single reference length (L_0), and is calculated as follows:

$$S_L(t) = \frac{L_t - L_0}{L_0} \tag{2.2}$$

where L_t represents the length at a given point in time and L_0 represents the reference length at the reference time t_0 (typically end diastole), as seen in Figure 2.1.

Lagrangian SR is the first derivative of Lagrangian strain:

$$SR_L(t) = \frac{dS_L(t)}{dt} = \frac{1}{L_0}\frac{dL_t}{dt} \tag{2.3}$$

Eularian (i.e., natural) strain $S_E(t)$ uses a reference length that changes as the object deforms and therefore provides information about instantaneous length change. Eularian SR is the temporal derivative of Eularian strain and describes the instantaneous rate of length change:

$$SR_E(t) = \frac{dS_E(t)}{dt} = \frac{1}{L_t}\frac{dL_t}{dt} \tag{2.4}$$

Note that Equation 2.4 differs from Lagrangian SR shown in Equation 2.3, in that the length of which it is normalised "L_t" changes over time. Eularian strain can be calculated by the integration of Eularian SR as follows:

$$S_E(t) = \int_{t_0}^{t} SR_E(t)dt = \int_{t_0}^{t} \frac{1}{L_t}\frac{dL_t}{dt}dt \tag{2.5}$$

Note that the reference length in Lagrangian strain calculation in Equation 2.2 is always constant at L_0 while Eularian strain has a variable reference length "L_t" as seen in Equation 2.5. The differences between Lagrangian and Eularian strain can be visualised in Figure 2.1.

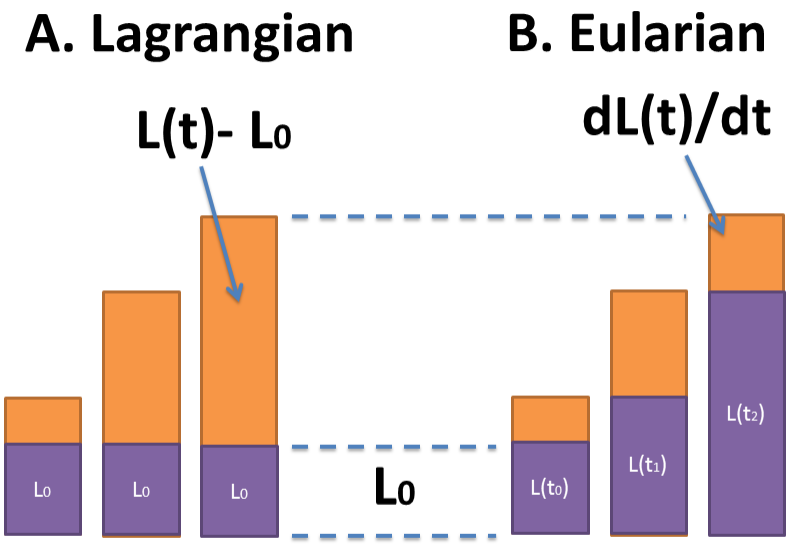

Figure 2.1: ***Graphical Representation of Lagrangian and Eularian Strain*** *Figure A. shows Lagrangian strain related to the baseline length L_0. Figure B. shows Eularian Strain as it relates to the variable baseline length L_{t-1}. This has been adapted from (1).*

The above 1D descriptions can be applied in all three orthogonal cylindrical directions: longitudinal, circumferential, and radial.

2.5.1 Multidimensional Deformation

The above concepts specifically refer to one dimensional motion (i.e. shortening and lengthening along the axis of the object). A 2D object is additionally capable of deforming perpendicular to its axis. This deformation is referred to as shear strain. The two on-axis *normal* strains and two shear strains can be expressed concisely as a strain tensor, $\in$:

$$\in = \begin{bmatrix} xx & xy \\ yx & yy \end{bmatrix}$$

where the diagonal elements (xx and yy) reflect the normal strain and the remaining elements refer to shear strain (xy and yx). This concept of normal and shear strain can be extended to higher dimensions. For three dimensional strain (22), there are three normal strains (xx,yy, and zz) and six shear strains (xy, xz, yx, yz, zx, and zy).

In cardiac imaging, it is standard practice to use a cylindrical coordinates in lieu of Cartesian coordinates, as the longitudinal, radial, and circumferential coordinates more closely reflect the anatomy of the heart. These cylindrical coordinates are demonstrated in Figure 2.2. In such a case, cardiac torsion (23; 24) can be described by the longitudinal-circumferential shear of the LV myocardial wall.

2.5.2 Conversion between Lagrangian and Eularian Strain

A following question is which strain (Lagrangian or Eularian) should be used as a surrogate for regional cardiac functional analysis. With tissue doppler imaging (TDI), where the reference length is different at each interrogation time point, Eularian strain can be directly calculated. Speckle tracking methods, where the baseline length is always known, lend themselves to Lagrangian strain. Luckily these two types of strain can be inter-converted by the follow equation:

$$S_L(t) = e^{S_E(t)} - 1 \tag{2.6}$$

For small deformation in the range of 5-10%, Eularian and Lagrangian strain are approximately equal. However, with larger deformations such as those that occur during ventricular contraction, there is a significant difference.

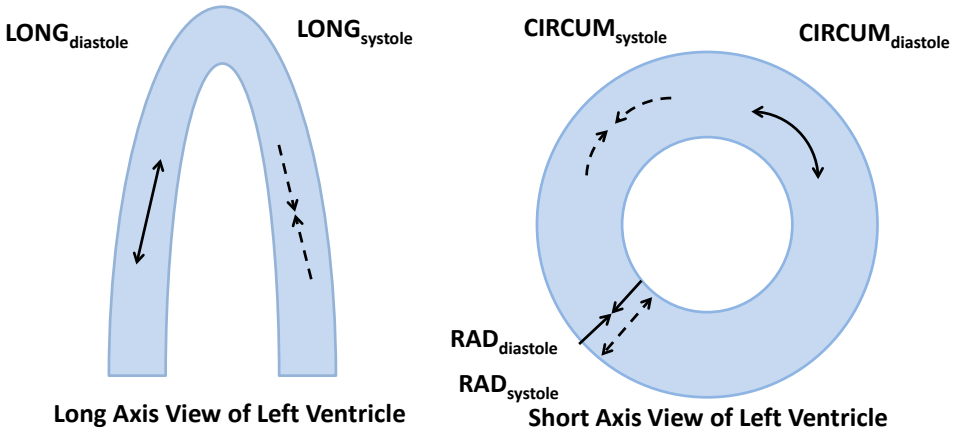

Figure 2.2: ***Graphic Representation of the Principal Myocardial Deformations.*** *Circumferential Strain (CIRCUM) Longitudinal strain (LONG), Radial strain (RAD). Note that during systole the heart muscle thickens. Adapted from (2).*

2.5.3 Comparison of Different Strain

Due to the 3D contraction pattern of the heart, there is no single "optimal" strain parameter that is most useful for all applications. In addition, the LV and RV have different contraction patterns so that different strain directions are likely to be more sensitive to myocardial dysfunction for each. To explain this difference between the LV and RV, it is useful to consider the directionality of the myofibres in each chamber (25). Myofibres in the RV are aligned in a more in a longitudinal direction than in the LV, and therefore longitudinal strain values are often a more sensitive indicator of RV dysfunction (25). In the LV, the magnitude of myocardial strain is larger in the radial and circumferential directions, which again may be explained by myofibre directions and interactions.

By definition, transmural thickening is positive whereas circumferential and longitudinal shortening is negative. Since circumferential strain will vary de-

pending on the short axis position, as referred to in Figure 4.1, the level of the heart is standardised as basal, middle (mid-ventricle), or apical. If unstated, it is often assumed that circumferential strain is in the mid-ventricle position. Circumferential strain and radial strain are obtained from a short axis (SAX) view of the heart, while longitudinal strain and radial strain is measured from the long axis orientation.

There has been various clinical studies performed comparing the different strains. For instance, in a study of use of LV strain as a predictor of response to cardiac resynchronization therapy (CRT), it was found that radial strain was a superior predictor to both circumferential and longitudinal shortening by echocardiography (26). In another study, change in specifically circumferential strain has been found to be useful for detecting acute increases in RV afterload (27; 28). Further studies will help validated such findings towards clinical application.

Finally, there have been a number of studies referring to principal strain (29; 30; 31). Principal strain, $\in$, refers to the case when there is no shear strain and is oriented in the direction of maximal myocardial contraction. It has been noted to change direction with ischemic injury (31). The greatest strain value is denounced as $\in_1$ followed by $\in_2$ and by $\in_3$.

2.6 Comparison Between Modalities for Regional Strain Analysis

The three main imaging modalities being considered for regional cardiac analysis are echocardiography, CMR, and CCT. Examples of these modalities can be seen in Figure 2.3. In this section, we will compare the current status of these modalities. Table 2.1 provides a comparison of these modalities according to a few key metrics including spatial resolution, temporal resolution, and duration of single study.

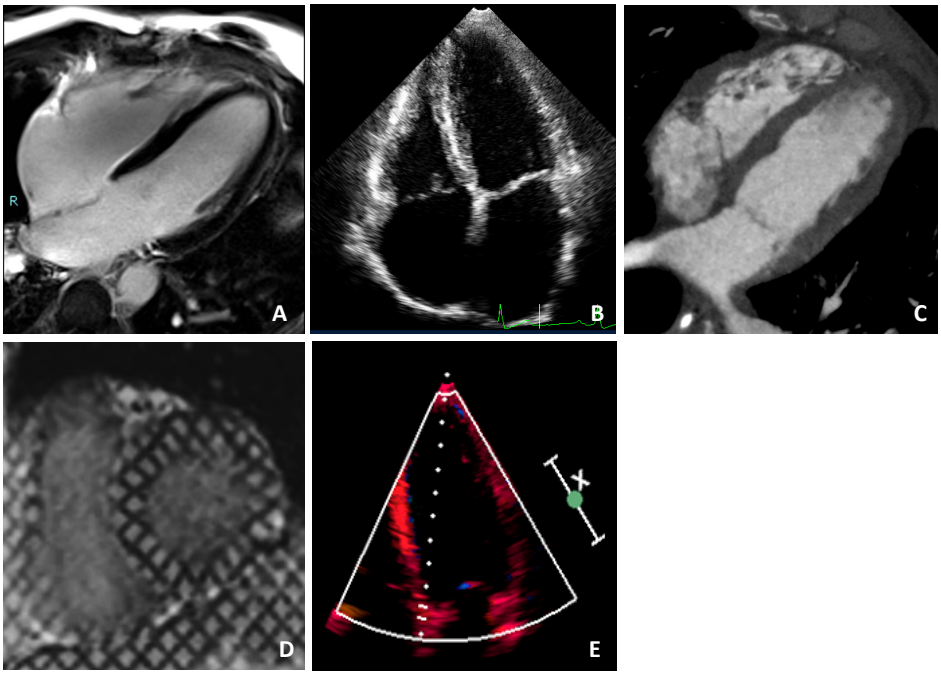

Figure 2.3: ***Comparison of Cardiac Imaging Modalities in the Four Chamber View.*** *(A) cMRI, obtained from 3 Tesla Siemens Verio. SSFP cine sequence used. (B) CCT, obtained from a 320 sliced Toshiba CT scanner. (C) Echocardiography, obtained from a Philips ie33 with a S5-1 probe. Additional image demonstrating (D) cardiac tagged MRI in short axis and (E) Tissue Doppler Echocardiography of the LV have been included. Images Courtesy of Chris T. Sibley (A and D), Paul Leeson (B), Eduardo Lima (E)*

Ultrasound (echocardiography) is the most widely used cardiac imaging technology in the United States. This can be attributed to its relative affordability, wide availability, and extensive validation. A limitation of echocardiography is the lack of an acoustic window for transducer placement for some patients and imaging planes. While efforts to address this have been made by fusion of image data from multiple angles (32; 33; 34; 35), the limitation in acoustic window makes it poorly suited for assessing the right ventricle (RV). A continuing issue plaguing echocardiography is the variation in repeated measurements due to its dependence on operator experience, machine settings, acoustic window and angle of incidence effects.

On the other hand, CMR has established itself as one of the more reliable

	CMR	Echocardiography	CCT
Spatial Resolution	1-2mm	<1mm	0.35-0.5mm
Temporal Resolution	25-50msec	10-25msec	83-175msec
Duration of single study	30-45 min	30min	10 min

Table 2.1: ***Comparison of Current CMR, CCT and Electrocardiography.*** *Comparison of main medical imaging modalities used in strain imaging in terms of spatial resolution, temporal resolution, and duration to perform a single study.*

and reproducible imaging modalities, especially for structural features. Work has continually been done to improve CMR, including developing techniques like tagged MR and HARP which are now considered the gold standard of cardiac strain imaging. Further discussions on these methods will be done in Chapter 3. However, despite these advances, the use of strain CMR has not been adapted into clinical practice. Practical drawbacks hinder its ability for clinical application, including gating issues, complex scanning protocols, prolonged scan times, claustrophobia, and economic expense. In addition, CMR is often contraindicated in patients with intracardiac devices due to the magnetic interaction with the cardiac device. The inability to study and treat this growing population leads to the need for alternative imaging strategies.

In many ways, CCT can be viewed as a compromise between echocardiography and CMR (see Table 2.1. CCT is easier to use, faster and more readily available then CMR, but provides better structural detail compared to echocardiography. From Table 2.1, it is possible to note the differences in temporal resolution, which can be considered to be sampling frequency. This is important to observe since temporal resolution can impact the strain and SR values produced, especially with speckle tracking methods since the speckle tracking method depends on smaller trackable motions from frame to frame. As noted in Table 2.1, CCT studies can potentially take a shorter amount of patient

time to perform. Considering the ease, speed, and innate 3D+t nature of the modality, it makes sense to explore its capabilities further as done in Chapter 4 and Chapter 7.

"A roentgenologic visualization of hte heart, in such a manner as to give a radiologic equivalent to its anatomical cross-section, has been an old problem in cardiac roentgenology...". Exploration of cross-sectional radiography of the heart.

—Gerhard Danelius, 1939 (36)

3 Technical Background

Contents

3.1 Introduction

In order to lay the groundwork for the rest of the thesis, this chapter will introduce the following topics related to the technical pipeline of obtaining strain measurements: methods of deformation analysis with CMR, methods of deformation analysis with echocardiography, methods of deformation analysis with CCT, and a general summary of these different methods.

Although analysis of cardiac deformation is well studied in CMR and echocardiography (and therefore the literature of normal strain values are currently based in these modalities as seen in Appendix B), currently there is no established method to obtain this information from CCT. In order to take steps towards establishing a method for cardiac deformation analysis in CCT, we shall first review the technical methodologies used for functional analysis in CMR, echocardiography, and CCT.

3.2 Deformation Analysis with Cardiac Magnetic Resonance

Detailed reviews of CMR deformation (37) and feature tracking (38; 39) are available in the literature. Here we will outline the key ideas only.

Cine MR is considered a reference method for obtaining global cardiac function measurements. However, the myocardium is relatively homogeneous on steady state free precession (SSFP) cine-MR (40) and therefore does not provide features which can be used to derive information on complex myocardial motion such as transmural shear or circumferential-longitudinal shear (torsion) (41).

Deriving this information has necessitated development of dedicated MR pulse sequences including tagged MR (7; 42; 43), phase-contrast (velocity encoding) (PC), displacement encoding with stimulated echoes (DENSE), and strain-encoding (SENC)(44; 45). PC, DENSE and SENC are based on the idea of encoding the velocity, displacement or strain of the tissue into the image. Out of these methods, analysis of tagged MR is the more widely used, having been implemented in large clinical trials such as the Multi-Ethnic Study of Atherosclerosis (MESA) (46; 47).

3.2.1 Tagged Magnetic Resonance

The most commonly used research method, tagged MR (Figure 2.3), is obtained by applying a radio frequency pre-pulse which induces dark lines ("tags") on the cardiac image. MR tag lines are created with a segmented k-space gradient echo pulse sequences such as delays alternating with nutations for transient excitation (DANTE) or spatial modulation of magnetization (SPAMM) (42; 48). The tag lines are applied at end diastole following the detection of the R wave on ECG (7) and are oriented perpendicular to the imaging plane. By applying the pre-pulse multiple times in orthogonal directions, it is possible to create a grid on cine MR images. These tags then deform across the cardiac cycle as the heart moves. The resulting tags fade significantly by early diastole due to T1 relaxation, limiting the assessment of diastolic relaxation using this method.

In complementary SPAMM (CSPAMM), two images are acquired and then subtracted from each other, allowing improved imaging of diastolic function due to decreased tag fading. Unfortunately, the CSPAMM technique can suffer from image mis-registration of the two acquisitions. Further improvements in the quality of tagged MR have been developed, and include under-sampled projection reconstruction (49). However it currently remains a technique mostly used in research due to higher costs, availability, relative complexity of acquisitions, and time-consuming image analysis.

After tagged MR acquisition, a separate analysis tool is needed to extract regional strain values. These methods include feature-based tracking, deformable models, Gabor Filter Banks, optic flow methods, local sine wave modelling, and HARP. The HARP method is based on the concept that the harmonic phase of the SPAMM modulation at a material point in tissue will remain constant and is therefore trackable throughout the cardiac cycle (50).

Recently, feature tracking algorithms have been applied to CMR (51; 52). Global strain can be reliably and easily calculated by simply contouring the en-

docardial border and comparing the maximal and minimal border lengths (52). However, the more interesting "regional" strain proves more difficult, requiring accurate tracking of individual myocardial segments in multiple dimensions.

3.3 Deformation Analysis with Echocardiography

Currently, echocardiography is the most widely available clinical modality for motion estimation of the myocardium (53). Initial studies focused on TDI techniques (See Figure 2.3) that provided myocardial velocity only along the ultrasound beam. Therefore, results were dependent on the angle of the ultrasound probe with respect to the heart. As an alternative, an angle-independent method, termed speckle tracking (54), has more recently been investigated.

3.3.1 Speckle Tracking

Speckles are a unique pattern generated in an ultrasound image by the underlying tissue microstructure. Small particles within the tissue absorb part of the ultrasound beam causing the beam to re-radiate in all directions as a spherical field. These re-radiated spherical scatter-waves interfere with each other, creating a speckle pattern. This pattern remains temporally consistent for small deformations and can be used as a feature for motion tracking.

Speckle tracking methods can be based on either the radiofrequency signal or B-mode (brightness mode) image (6). The B-mode image is actually obtained from the RF signal after filtering, envelope detection and log compression. It is a real time grey scale 2D display of the ultrasound information. The benefit of using B-mode analysis includes lower data storage and higher temporal sampling (55). The majority of speckle tracking methods are based on a pixel-intensity based block matching approach where a square image block (speckle patch) in one image is defined and then best matched to the next image. The matching criterion is based on a similarity measure such as the sum

of squared difference, cross correlation, or mutual information. This matching occurs within a small, user defined neighbourhood to reduce the computational time. It is important that the speckle block be sufficiently large (20-40 pixels) (56) to avoid erroneous matches.

Strain analysis systems can be done from boundary tracking of the endocardial and epicardial contours. Segmentation of the boundaries can be done based on phase based acoustic features (57), intensity information (58) and speckle statistics (59). After segmentation of the endocardial and epicardial contours (60; 61) the correspondences between the two contours are estimated. Finally, the deformation between these two contours is estimated, reflecting the motion of the myocardium.

Boundary tracking may be improved by accounting for muscle fibre direction, (assuming a transversely isotropic linear-elastic model) (60; 61), a Kalman filter (62; 63) or active appearance model (39). From the end user perspective, the limiting factor is segmentation quality, with continue work being done in this area (1).

3.4 Deformation Analysis with Cardiac Computed Tomography

Over the past decade, there have been a number of advances in CCT in terms of image resolution and radiation reduction, as compared with echocardiography and CMR as seen in Table 2.1 (64; 65; 66; 67). Further information about CT can be found in Appendix A. A state of the art CCT system features 64 to 320 rows of detector elements, allowing the entire heart to be imaged in 3D at a resolution of 0.5 mm across multiple heartbeats. Such technological advancements allowed for the investigations in Chapter 4 and Chapter 7.

Currently though, the primary motivation for CCT has been depiction of coronary artery anatomy (68; 69; 70). A single "snapshot" of coronary anatomy is acquired during a limited portion of the cardiac cycle, usually during early

to mid-diastole. By imaging only a portion of the cardiac cycle, radiation dose can be substantially reduced. Current CCT scans can acquire images of the coronary arteries with only 1-3 mSV of radiation, compared to 5-10 mSv for diagnostic catheter-based coronary angiography (71; 72).

In order to assess myocardial function with CCT, the entire cardiac cycle needs to be imaged. This results in higher radiation dose compared to imaging coronary anatomy alone. On the other hand, patients with coronary artery disease or heart failure are likely to be older individuals for whom radiation exposure is somewhat less of a concern. The issue of radiation dose is further explored in Chapter 5 and Appendix C.

3.4.1 SQUEEZ

As can be noted, unlike echocardiography and CMR which can have physiological "tags", no such trackable markers exist with CCT. While we explore this issue further in chapter 6 and chapter 7, to circumvent this issue, McVeigh et al (8) created a metric to represent the local contraction of the endocardial surface called Stretch Quantifier for Endocardial Engraved Zones (SQUEEZ). This method does not obtain strain measurements but rather tries to represent the relative motion of surface features representing local contraction. A 3D model of the myocardium was created by endocardial surface extraction. A coherent point drift (CPD) non-rigid point registration algorithm was then used for surface warping. CPD allowed to align two N-Dimensional point sets and recover the correspondences. Afterwards, a mesh of triangles were created to encode features in the 3D volume from end diastole (used as the template) to end systole (used as the target). The derived measurement is, however, not the same physical measurement as strain and does not provide information about myocardial shortening. Also, at the moment, the mathematical relationship between the SQUEEZ measurements and strain has not been established.

Part I

Clinical Contributions

"A method is given of finding a real function in a finite region of a plane given its line integrals along all straight lines intersecting the region. The solution found is applicable to ... the determination of a variable x-ray absorption coefficient in two dimensions..." Described a technique for calculating the absorption distribution in the human body.

—Allan MacLeod Cormack, 1963 (73)

4

Evaluation of feasibility of functional CCT towards subtle disease detection

Contents

4.1 Abstract

Purpose: To investigate the use of cine multidetector computed tomography (MDCT) to detect changes in myocardial function in a swine cardiomyopathy model.

Methods: All animal protocols were in accordance with the 'Principles for the Utilization and Care of Vertebrate Animals Used in Testing Research and Training' and approved by the University of Missouri Animal Care and Use Committee. Strain analysis of cine MDCT images of the LV was optimized and analyzed with feature tracking software. The standard of reference for strain was harmonic phase analysis (HARP) of cardiac magnetic resonance (CMR) tagged images performed at 3.0-Tesla. An animal model of cardiomyopathy was imaged using both CMR and 320-slice MDCT at less than 50 msec temporal resolution. Three groups were evaluated: control group (n=5), aortic banding-induced myocardial hypertrophy group (n=5), and aortic banded-Cyclosporine A treated cardiomyopathy group (n=5). Histological samples of the myocardium were obtained for comparison to strain results. Dunnett's test was used for comparisons of the concentric remodelling group and eccentric remodelling group against control group.

Results: Collagen volume fraction ranged from 10.9 to 14.2%; lower collagen fraction values were seen in the control group compared to the cardiomyopathy groups ($p<0.05$). Ejection fraction and conventional metrics showed no significant differences between control and cardiomyopathy groups. Radial

strain for both CMR and MDCT was abnormal in both concentric remodelling (CMR 25.1 ± 4.2%; MDCT 28.4 ± 2.8%) and eccentric remodelling groups (CMR 23.2 ± 2.0%; MDCT 24.4 ± 2.1%) relative to controls (CMR 18.9 ± 1.9%; MDCT 22.0 ± 1.7%, $p<0.05$, all comparisons). Strain values for MDCT compared to CMR showed better agreement in the radial direction than in the circumferential direction ($r=0.55$, $p=0.03$ vs. $r=0.40$, $p=0.13$, respectively).

Conclusion: MDCT strain analysis has potential to identify regional wall motion abnormalities in cardiomyopathy that is not otherwise detected using conventional metrics of myocardial function.

Publication: This chapter is a based on the publication "Regional Strain by Multidetector Computed Tomography in Cardiomyopathy: Relationship to CMR tagging and Myocardial Fibrosis. *Radiology* (accepted November 2014)". This work involved the contribution of a multidisciplinary team of physicians, nurses, and technicians. I led this study and was involved with multiple aspects of the project. Cynthia Davies-Venn, Colin Yi, Fabio Raman, Song Tao Liu, Al Lardo, and Craig Emter were involved in the animal preparation and imaging. Samuel Won, a post-baccalaureate student, performed the histological analysis of fibrosis. Davis Vigneault and Fabio Raman assisted in the tagged MR images analysis. Veit Sandfort, J. Alison Noble, Joao Lima, Craig Emter and David A. Bluemke all provided guiding input into this work.

4.2 Introduction

4.2.1 Clinical Utility of Cardiac Strain Assessment

There is a growing body of evidence to suggest that myocardial deformation can provide incremental information useful in the clinical setting (56; 74; 75; 76; 77; 78). By understanding how myocardial deformation changes in different pathophysiologies, it maybe be possible to diagnose cardiac diseases at an earlier stage (2). A few examples of potential applications of myocardial strain estimation are shown in Table 4.1.

Disease and/or Therapy	Current Potential Cardiac Strain Application
Congenital heart disease	Potentially useful in monitoring treatment in congenital heart disease such as aortic coarctation, single ventricle, and tetralogy of Fallot (79; 80; 81; 82)
Cardiotoxicity with Cancer Therapy	Early detection of chemotherapy-mediated cardiotoxicity (83)
Hypertrophic Cardiomyopathy (HOCM)	Identification of preclinical disease in carriers of HOCM mutations (84)
Arrhythmogenic Right Ventricular Dysplasia (ARVD)	Strain analysis allows differentiation between manifest or borderline ARVD, and healthy volunteers even if ejection fraction is normal (85)
Coronary Artery Disease (CAD)	Early diagnosis of CAD (86)
Myocardial ischaemia	Diagnosis of early myocardial ischaemia (87; 88)
CRT	Use in HF and CRT to help direct pacing lead placement to the region with the most delayed mechanical contraction (89; 90).
Myocardial Fibrosis	A surrogate parameter of myocardial fibrosis (91; 92; 93)

Table 4.1: ***Cardiac Strain Potential Clinical Utility.*** *Examples of investigated disease models and therapy where strain analysis may prove of clinical benefit.*

While the focus of strain research has been on the LV, continued work is being done to investigate its utility in analysing the deformation of the left atrium (potentially useful in patients with atrial fibrillation) and right ventricle (RV) (94) (potentially useful in patients with pulmonary hypertension, systemic RV and repaired tetralogy of Fallot) (95).

4.2.2 Current Standard for Cardiac Strain Analysis

The current reference standard for functional analysis is tagged MR (96). However, tagged MR image acquisition and processing for strain analysis remains time consuming and is thus usually not performed for routine clinical studies. As an alterative, regional function analysis of the myocardium with MDCT has

been shown to identify focal wall motion abnormalities in a manner analogous to CMR strain (97) due to myocardial infarction (98), and interest is growing to explore this modality's capabilities further.

4.2.3 Potential Utility of Functional Analysis with CCT

In terms of clinical utility of regional cardiac strain analysis with CCT, there are two clear potential applications. Firstly, there is the treatment of HF with CRT which involves pacing simultaneously or with a slight delay, the RV and LV (89; 90; 99; 100). And secondly, there is the detection of subclinical cardiac disease often in cases of normal ejection fraction (101; 102; 103; 104; 105). The following discussion will explain the potential of CCT to impact these areas.

4.2.3.1 Application of Regional Wall Motion Quantification in Cardiac Resynchronization Therapy

In terms of clinical utility of regional cardiac strain analysis with CCT, a clear potential application is for the treatment of HF with CRT (25; 28; 74). Heart disease continues to be a lead causing of death in the United States, with HF affecting nearly 5.8 million in the USA alone (26; 27). For both mild HF (NYHA II) (75) and advanced HF (NYHA III-IV) (76; 77), CRT has been shown to decrease mortality, decrease the risk of HF events, induce favourable LV reverse remodelling and slow the progression of HF symptoms. However, there continues to be a high number of nonresponders to CRT, ranging from 10.8% to 50% (56; 78).

It is thought that better identification of CRT candidates, as well as better delivery of CRT, will improve the response rate to CRT. A number of clinical, laboratory, and pacing predictors have been explored in order to improve the rate of CRT response. One predictor that stands out is strain analysis, which a number of authors suggest to be a reliable and potentially superior method to other metrics in predicting CRT response (86; 105).

In addition, studies have indicated that placing of these leads should be made at the location with the most delayed mechanical contraction (74). It is thought that successfully locating the optimal location for the pacing leads could improve the rate of response (87).

CCT is currently being used in CRT, specifically for extracting the access path through coronary veins in LV lead placement (88). In order to incorporate functional information for improved lead placement, research has been done towards fusing CCT (for anatomical information) with CMR (for functional information) (106). Other studies, using CCT as a reference, examined its potential to fuse with echocardiography (83). However, instead of fusing modalities, another possibility would be to obtain functional information from CCT itself in a single examination.

4.2.3.2 Detection of Subclinical Cardiac Disease with Preserved Ejection Fraction

As discussed in Chapter 2, in ischaemic diseases it is found that the currently used standard metric for cardiac function, ejection fraction, may not be able to detect very early disease (17; 103). It has been noted that half of the patients with the clinical syndrome of HF in the community have preserved ejection fraction (HFpEF) (17; 107). This has led to the exploration of strain analysis, which has found that with HFpEF, both diastolic function (102) and systolic function (104; 105) may be affected.

Similar work has started to be conducted in non-ischaemic diseases towards detection of sub-clinical cardiac dysfunction, often in cases of normal EF (85; 101). A common feature of many non-ischaemic cardiomyopathies is the development of diffuse interstitial and replacement myocardial fibrosis (108). Depending on the extent of the disease, regional and global motion abnormalities are associated with interstitial fibrosis (109). Non-invasive detection of myocardial function abnormalities in diffuse disease is challenging and relies on quantitative analysis of myocardial strain (92; 93; 110). This clinical need

has also led to interest in investigating and optimizing the use of CT towards functional evaluation and analysis.

4.2.4 Rationale and Specific Aim

Given the interest in detection of sub-clinical disease, this chapter's purpose is to investigate the use of cine MDCT to detect changes in myocardial function in a swine cardiomyopathy model of sub-clinical disease. The hypothesis is that strain measurements would detect differences between the cardiomyopathy groups and the control group.

4.3 Material and Methods

4.3.1 Animal Preparation

All animal protocols were in accordance with the 'Principles for the Utilization and Care of Vertebrate Animals Used in Testing Research and Training' and approved by the University of Missouri Animal Care and Use Committee. The animals used in the current study were previously characterized (111; 112) in terms of concentric (hypertrophy) and eccentric (dilatation, increased mass) remodelling of the left ventricle (LV). In brief, intact male Yucatan miniature swine (27-30 kg; 8 months old) were matched for body mass and cardiac function. Animals were randomly assigned to control (n=5), aortic-banded (concentric hypertrophy) group (n=5), and aortic banded-Cyclosporine A treated cardiomyopathy (eccentric remodelling, heart failure) group (n=5). Mild hypertrophy/HF was induced by aortic banding for a period of 20 weeks (111; 112), using previously published techniques (112) with *in vivo* determination of LV and mean arterial pressure prior to humane euthanasia . Cross sections of LV matched to CMR/MDCT SAX images were formalin fixed, embedded in paraffin, and stained for assessment of fibrosis and collagen as previously described (113).

4.3.2 Region of Interest Definitions

The definitions of the Region of Interest (ROI) were adapted from the Society for Cardiovascular Magnetic Resonance (SCMR) and the European Association of Cardiovascular Imaging (EACVI)/American Society of Echocardiography (ASE)/Industry leaders consensus statements (1; 114).

Our ROIs were defined at the end-diastole phase of the cardiac cycle. End-diastole is defined by the closure of the mitral valve (i.e. the frame before mitral valve completely close). Other surrogate events which are time-related to the closure of the mitral value and this may be used as surrogates include the beginning of the QRS complex in an ECG, the ECG R-peak, the largest diameter or volume of the LV, or the peak left ventricular longitudinal strain. However, these surrogate markers may be suboptimal, such as in cases of conduction delays.

At end-diastole, segmentation should produce an endocardial border (the inner contour of the myocardium), an epicardial border (the outer contour of the myocardium) and a myocardial midline (the middle ROI axis, defined as the midpoint between the inner and outer ROI contours). Measurements should reflect the behaviour of the area they represent.

There are a number of LV segmentation models including the 16 segment, 17 segment, and 18 segment model of the LV (1); However, the most commonly used one used for strain analysis is the 16 segment model. The 16 segment model is similar to the 17 segment model, but without a separate region indicating the apex of the heart, since the apical cap does not contract.

In terms of the SAX division of the heart, this is done by first taking the length of the heart in the longitudinal view at end-diastole from the valvular plane to the bottom of the LV cavity. This length is then divided into thirds from the basal slice (nearest to the valvular plane), middle slice (between the basal and apical slice), and apical slice (nearest to the apex).

In the SAX view, the myocardium is further segmented. This further segmentation is also defined at end-diastole. In order to accurately segment the LV, the anterior RV insertion point and inferior RV insertion points are used as anatomical references (115). For the basal and middle slice with a total of 6 segments, the anterior RV insertion point defines the boundary between the anterior and anterior-septal segments, and the inferior RV insertion point defines the boundary between the inferior and inferior-septal segments. For the apical slice with four segments, the anterior RV insertion point defines the boundary between the anterior and septal segments, and the inferior RV insertion point defines the boundary between the inferior and septal segments. After establishing the septal boundaries, the rest of the segments can be established by dividing the sections equally. In the case of the basal and middle six segment slices, this would include dividing the septal segment into two equal segments (i.e. an inferior-septal and anterior-septal slice) and the rest into four equal segments (anterior, anterior-lateral, inferior-lateral, and inferior). For the apical four segment slices, there is one septal segment and the rest are from obtained from dividing the length into equal segments (i.e. anterior, lateral and inferior). Visual representation of this model can be seen in figure 4.1.

4.3.3 Strain

Average radial strain and circumferential strain were obtained in this study via SAX views of the heart. These strain values were calculated according to the following equations:

$$RS_{av} = 100 * \frac{L_{P_{endo(i)}P_{epi(i)}} L_{P_{endo(ref)}P_{epi(ref)}}}{L_{P_{endo(ref)}P_{epi(ref)}}} \tag{4.1}$$

where RS_{av} is the average radial strain, $L_{P_{endo(i)}P_{epi(i)}}$ is the length between point $P_{endo(i)}$ and point $P_{epi(i)}$ at time i, and $L_{P_{endo(ref)}P_{epi(ref)}}$ is the length between point $P_{endo(ref)}$ and point $P_{epi(ref)}$ at the reference time (which is the time at end diastole).

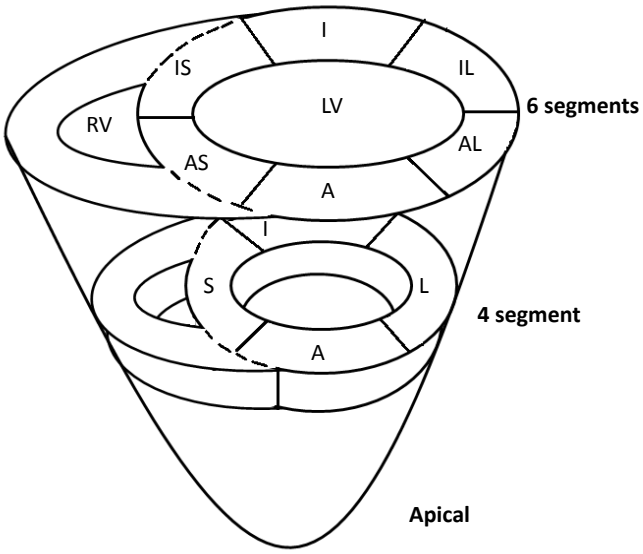

Figure 4.1: ***Graphic Representation of Heart Segmentation.*** *Model of the ventricles of the heart showing the location of the right ventricle (RV) and left ventricle (LV) as well as standardised terms used to divide the heart. Anterior (A), Anterolateral (AL), Anteroseptum (AS), Inferior (I), Inferolateral (IL), Inferoseptum (IS), Lateral (L), Septal (S) in terms of six segments (such as the basal and middle slices) and four segments (such as the apical slice in the 16 segment model.*

$$CS_{av} = 100 * \frac{L_{P_{mid(i-10)}P_{mid(i+10)}} L_{P_{mid(ref-10)}P_{mid(ref+10)}}}{L_{P_{mid(ref-10)}P_{mid(ref+10)}}} \tag{4.2}$$

where CS_{av} is the average circumferential strain, $L_{P_{endo(i)}P_{epi(i)}}$ is the length between point $P_{mid(i-10)}$ and point $P_{mid(i+10)}$ at time i, $L_{P_{endo(ref)}P_{epi(ref)}}$ is the length between point $P_{mid(ref-10)}$ and point $P_{mid(ref+10)}$ at the reference time which is the time at end diastole.

The points from equations 4.1 and equation 4.2 correspond to the points labelled in Figure 4.2.

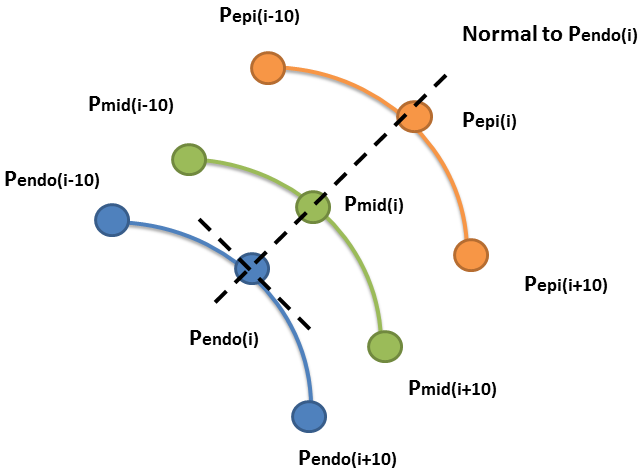

Figure 4.2: ***Points Illustration for Strain Calculation.*** *The points used to calculated radial and circumferential strain in equations 4.1 and 4.2 are shown here.*

4.3.4 CMR Scanning Parameters and Analysis

CMR images were obtained on a 3.0-Tesla scanner (Biograph mMR, Siemens Medical Solutions, Erlangen, Germany), with a phase array coil. Grid short-axis tagged CMR images were acquired using an electrocardiographically triggered fast gradient echo sequence, with a spatial modulation of magnetization (field of view 360 mm to 400 mm, slice thickness of 6 mm, gap of 4 mm, phase resolution of 75% to 85%, repetition time/echo time of 15.5/2.3 ms, flip angle of 10 °, matrix size of 256 x 256, tag distance of 6 mm, segmentation factor of 3, temporal resolution of 16 msec). Tagged images were analysed by the reference standard method, HARP (Diagnosoft, v.4.3.1, Morrisville, NC) (116).

Imaging for myocardial scar was performed using late gadolinium-enhanced (LGE) CMR after intravenous infusion of gadopentetate dimeglumine (0.15 mmol per kilogram of body weight, Magnevist; Bayer Healthcare Pharmaceuticals, Wayne, NJ) via a 20-gauge peripheral catheter. Phase-sensitive inversion-

recovery LGE CMR imaging was performed 15 minutes after injection.

4.3.5 Multidetector Computed Tomography Scanning

MDCT images were acquired on a Toshiba Aquilion 320 One Vision scanner (Toshiba medical systems, Otawara, Japan) with echocardiographic monitoring. A 60 mL bolus of nonionic iodixanol contrast agent (Visipaque 320 mg iodine/mL, GE Healthcare, Oslo, Norway) was used at a 5 ml/sec flow rate at a dose of 2 ml/kg, followed by a saline bolus chaser using a double-head power injector. Bolus tracking was performed to yield homogenous enhancement of the ventricular cavity (117).

Cine cardiac image was acquired using gantry rotation time 275 msec, tube current 350-450 mA, tube voltage 120kV, collimation 0.5 mm, isotropic image matrix 512 x 512 pixels, and 3-4 RR interval segmented acquisition (average temporal resolution 49 ms). MDCT images were reconstructed with multiple segment iterative reconstruction algorithms (AIDR3D standard; Toshiba Medical Systems). Twenty images were reconstructed every 5% over the RR interval.

Images were transferred to a dedicated offline workstation, Vitrea 2 (Vital Images, Minnetonka, Minnesota). Images were reformatted into apical, middle, and basal short-axis views, according to the 16 segment model (AHA) with 5 mm slice thickness. Window level was adjusted to optimize the contrast between tissue and blood. Cine images were stored in the audio video interleave (AVI) uncompressed format.

4.3.6 MDCT Feature Tracking

Cine MDCT audio video interleave (AVI) images were uploaded into multimodality tissue tracking (MTT) software (Toshiba, v.6.0, Tokyo, Japan) for regional strain calculation (98). MTT was used to calculate strain between sequential image frames, from systole to diastole, using an on-screen pixel pattern template matching technique adapted from echocardiography (20). After

semi-automatic contouring of the endo- and epi-cardial borders, multiple tracking points (small pixel patterns representing tissue contours) were identified. Around each tracking point, a template image (10 x 10 mm) was assigned. By searching in the following frame for the most similar template image, the new location of the tracking point was determined. A squared error function was used to test for template similarity. From these correspondences made between frames, motion vectors were created and strain was quantified, as seen in Figure 4.3.

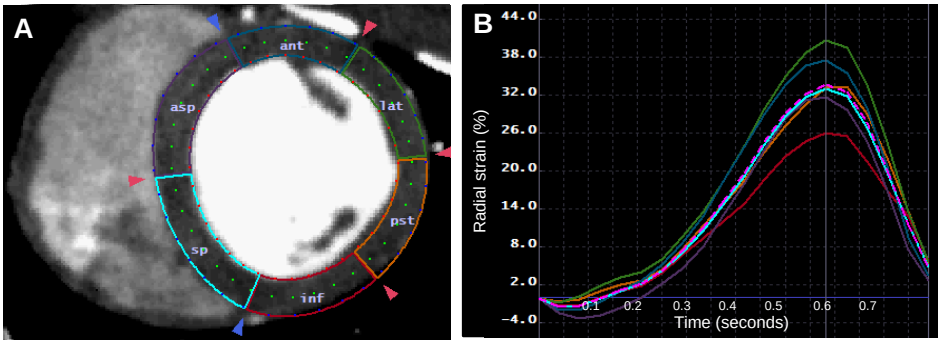

Figure 4.3: ***Multi-Modality Tissue Tracking (MTT) Analysis for Multidetector Computed Tomography (MDCT) Images.*** *(A) American Heart Association (AHA) segmentation of middle LV short axis into anterior (ant), anterior septal (asp), inferior (inf), lateral (lat), septal (sp) and posterior (pst) segments at end-diastole and (B) strain curve. The y-axis represents percentage radial strain. The x-axis represents time during the cardiac cycle. Tracing of endo- and epi-cardial borders was performed at end diastole.*

The inferior and anterior insertion points of the RV on the inter-ventricular septum were used as references for cardiac segmentation. End-systole was determined as the time of aortic valve closure. Segments with inadequate tracking were excluded from strain analysis. After successful tracking, the magnitude and timing of peak systolic radial strain for each of the six equiangular segments was extracted and used for further analyses. To compare strain measurements by MDCT to those by tagged CMR, MDCT data were also grouped according to the AHA-segment analysis, using tagged CMR images' anatomic landmarks and intracavitary diameter. Two experienced cardiovascular imaging re-

searchers (M.W.T. and F.S.R., with 8 and 3 years of experience, respectively) evaluated image quality independently.

4.3.7 Statistical Methods

Data are presented as mean ± SE. Dunnett's test was used for comparisons of the concentric remodelling group and eccentric remodelling group against control group. Validation Comparison of strain values for HARP and MTT were evaluated using linear-regression analysis and Bland-Altman plots. Intra- and inter-observer variability in MDCT strain measurements were evaluated for the mid-slice using the intraclass correlation coefficient (ICC) in a two-way random model (ICC <0.40 = poor; ICC $\leq$ 0.40 to 0.75 = good; ICC >0.75 = excellent agreement). Statistical differences were considered significant at a p value $\leq$ 0.05. Statistical analyses were performed using MedCalc 12.2.1 (MedCalc Software, Mariakerke, Belgium) and R (R Foundation for Statistical Computing, Vienna, Austria).

4.4 Results

4.4.1 Histology

Histological analysis was performed in fifteen animals. Animals in the control group showed evidence of less collagen compared to concentric and eccentric remodelling groups, Figure 4.4. Overall, the mean collagen volume fraction (CVF) was 10.9% for controls compared to 14.2% and 12.5% in the concentric and eccentric remodelling groups, respectively ($p \leq 0.05$ for both comparisons, Tables 4.3). No focal scars were detected by LGE CMR or histology.

4.4.2 Imaging Analysis

CMR and/or MDCT imaging was available in twelve out of fifteen animals (2 controls and 1 concentric remodelling animal were excluded due to inadequate image quality). This resulted in a total of 192 segments available for function

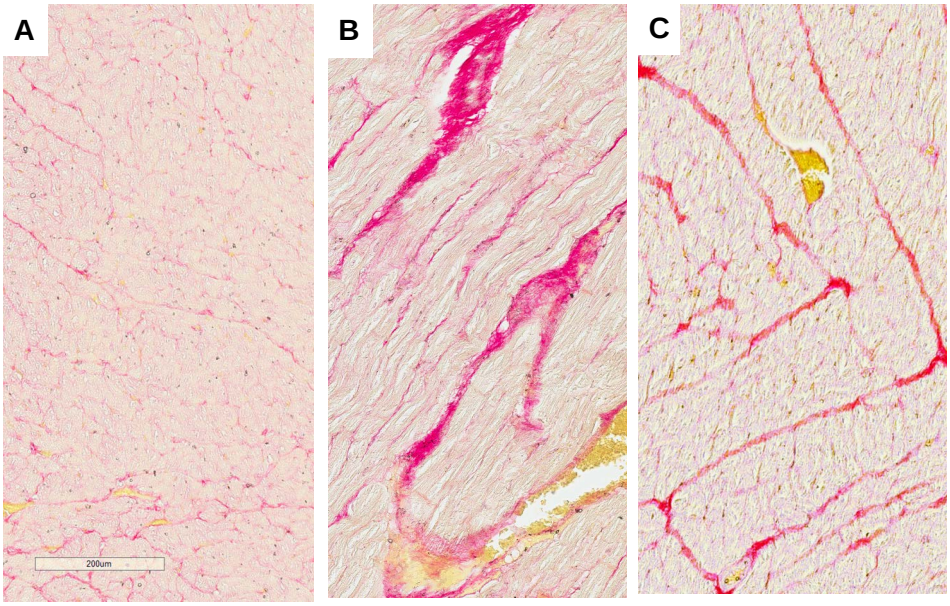

Figure 4.4: ***Representative Histology of Three Different Groups.*** *Histology was performed with Picrosirius Red staining for collagen. Collagen is the pink/red stained areas. (A) Control Group with 10% collagen volume fraction (CVF). (B) Concentric Remodelling Group with 15% CVF (C) Eccentric Remodelling Group with 13% CVF. Scale Bar represents 200 μm.*

analysis, of which 167 (87%) were analysable by both CMR and MDCT. Global and regional measures of left ventricular structure obtained from MDCT, CMR and histology are presented in Table 4.2 and Table 4.3.

LV mass was greatest in the eccentric remodelling group (103 g) compared to concentric remodelling (87g) and control groups (85g) ($p<0.05$, eccentric vs. control group). When adjusted for body weight or end-diastolic volume, LV mass was not significantly different. Conventional function metrics obtained by both MDCT and CMR, such as ejection fraction (EF), were lower in the eccentric remodelling group compared to control but were not statistically significant (e.g., ejection fraction, 47% vs. 54% by MDCT, respectively, $p \leq 0.05$). Similarly, comparisons between controls vs. cardiomyopathy groups showed no statistically significant group differences in conventional parameters such as stroke volume, end-diastolic volume, and end-systolic volume (Table 4.2). Mean wall thickness was measured to be greater in both MDCT and CMR

	Control mean ± SE	Concentric remodelling mean ± SE	Eccentric remodelling mean ± SE
LV ESV (mL)	31.9 ± 2.7	24.3 ± 1.6	42.7 ± 3.2
LV EDV (mL)	70.4 ± 7.2	56.5 ± 5.8	80.3 ± 4.0
LV SV (mL)	38.5 ± 5.1	32.2 ± 5.2	37.6 ± 2.2
LV EF (%)	54.2 ± 2.3	55.8 ± 3.6	47.0 ± 2.5
LV Mass (g)	84.9 ± 4.1	86.9 ± 2.7*	103.0 ± 2.5*
LV Mass/ EDV (g/mL)	1.3± 0.1	1.6± 0.2	1.2 ± 0.1
LV Mass/Body Weight (g/kg)	2.3 ± 0.1	2.3 ± 0.1	2.3 ± 0.1

Table 4.2: ***Global Metrics of LV Structure from MDCT.*** *Mean ± standard error (SE). EDV, end diastolic volume; ESV, end systolic volume; LV, left ventricle; SV, stroke volume; MDCT, multidetector computed tomography; M/V, LV mass/LV volume. * indicates significant difference from control group ($p<0.05$).*

in the concentric remodelling group compared to control, but was not significantly different (11.8 mm vs. 10.8 mm, respectively, $p \leq 0.05$). In contrast to the above metrics, mean radial and circumferential strain for both MDCT and CMR were significantly different in the cardiomyopathy groups compared to the controls (Table 4.3.), suggesting greater sensitivity of the strain measures.

Figure 4.5 depicts comparison of strain values for MDCT vs. tagged CMR for each of the AHA 16 segments. For peak radial strain, CMR absolute strain values were higher than MDCT values with a mean ± SE difference of -3.0 ± 4.2%. For peak circumferential strain, CMR absolute strain values were lower than MDCT values, with a mean difference of -2.4 ± 2.3%. Strain values for MDCT compared to CMR showed better agreement in the radial direction than in the circumferential direction (r=0.55, p=0.03 vs. r=0.40, p=0.13, respectively). Inspection of the Bland-Altman plot did not reveal any systematic bias.

There was good inter-observer agreement (ICC= 0.45) and excellent intra-observer agreement (ICC=0.85). MTT for MDCT strain analysis required 69 ± 2 seconds per 2D slice, compared to HARP for tagged CMR analysis which required 175 ± 4 seconds per 2D slice.

	Control mean ± SE	Concentric remodelling mean ± SE	Eccentric remodelling mean ± SE
Function, Wall Thickness			
CMR, End Systolic thickness (mm)	10.8 ± 0.4	11.8 ± 0.8	12.1 ± 0.5
CMR, End Diastolic thickness (mm)	7.7 ± 0.3	8.0 ± 0.7	8.0 ± 0.3
CMR, percentage wall thickness change (%)	42.9 ± 2.9	45.3 ± 7.5	41.2 ± 3.7
MDCT, End Systolic thickness (mm)	11.7 ± 0.6	11.7 ± 0.6	11.6 ± 0.6
MDCT, End Diastolic thickness (mm)	7.9 ± 0.1	7.9 ± 0.1	7.8 ± 0.2
MDCT, percentage wall thickness change (%)	49.2 ± 7.7	49.8 ± 8.2	49.4 ± 8.2
Function, Strain			
CMR, Radial strain (%)	18.9 ± 1.9	25.1 ± 4.2*	23.2 ± 2.0*
CMR, Circumferential strain (%)	-12.6 ± 1.0	-13.8 ± 1.1*	-10.2 ± 0.9*
MDCT, Radial strain (%)	22.0 ± 1.7	28.4 ± 2.8*	24.4 ± 2.1*
MDCT, Circumferential strain (%)	-8.6 ± 1.1	-11.7 ± 1.6*	-9.7 ± 1.4*
Histology			
Collagen volume fraction (%)	10.9 ± 0.7	14.2 ± 0.8*	12.5 ± 0.5*

Table 4.3: ***CMR Versus MDCT Regional Function vs. Histology.*** *Mean ± standard error (SE). CMR, cardiac magnetic resonance; EF, ejection fraction; MDCT multidetector computed tomography; LV, left ventricle. * indicates significant differences from control group ($p<0.05$).*

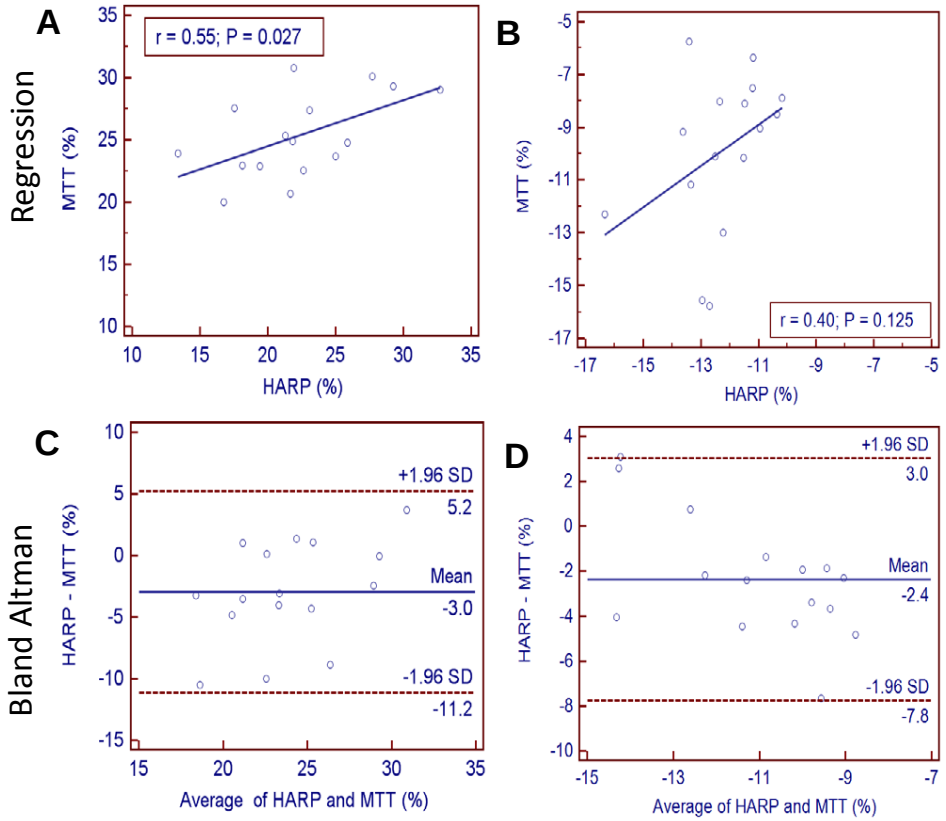

Figure 4.5: ***Strain Comparison.*** *Comparison of strain values for HARP (harmonic phase analysis of tagged CMR images) and MTT (multimodality tissue tracking analysis of MDCT images) according to the AHA 16-segment model. For radial strain, regression analysis (A) and Bland Altman analysis (C) between MDCT and tagged CMR. For circumferential strain, regression analysis (B) and Bland Altman analysis (D) between MDCT and tagged CMR.*

4.5 Discussion

Comprehensive evaluation of myocardial disease involves both global and regional evaluation of myocardial function. In this study, we evaluated animals displaying both eccentric and concentric myocardial remodelling (111), along with supporting histologic analysis. We found that mean radial and circumferential strain, measured by both MDCT as well as CMR, were significantly different in the diseased groups compared to the controls. The results indicate that MDCT segmental strain analysis has the potential to detect abnormalities in myocardial function in cardiomyopathy in a manner similar to CMR strain

analysis.

Previous studies have shown that MDCT can accurately assess global metrics of myocardial structure and function, such as EF, LV mass and volumes (118; 119). In such studies, CMR is frequently the standard of reference — a method we continue in the current study.

However, myocardial disease usually proceeds from a regional to global abnormalities. Regional analysis of myocardial structure has been investigated by cine MDCT and is typically evaluated in a semi quantitative fashion; wall motion is scored visually as normokinetic, hypokinetic, akinetic or dyskinetic (118; 120). Alternatively, percentage change in wall thickness can also quantify regional myocardial function (121; 122). These anatomic approaches are particularly effective for evaluation of myocardial scar related to infarction. This has led to research such as ours investigating the quantification of regional cardiac strain.

An aspect of the current study is the comparison of both the reference standard (CMR) as well as MDCT to relevant histologic changes in the myocardium. In addition, we focused on a disease model where indices of global function or wall thickening measure showed only subtle changes in response to the disease process. Previously, Helle-Valle, et al (98) showed abnormalities by MDCT regional strain (123) in 16 patients with myocardial infarction. For myocardial infarction, LGE CMR presents a standard of reference that has been shown to have excellent agreement to histologic analysis for focal scars. However, approximately 50% of patients with heart failure have normal ejection fraction, typically without focal myocardial scar. The pathophysiology of HFpEF is very challenging to identify using conventional anatomic CMR or MDCT indices of structure and function, and often includes myocardial remodelling and fibrosis (124; 125). Collagen deposition in the myocardium is a common endpoint of many diseases of the myocardium, as well as a mechanism that is also present in advanced aging (126). As hypertension progresses and becomes severe, left ventricular remodelling occurs. In this study, the degree of

systolic hypertension was insufficient to result in large functional change, but definite differences between control and cardiomyopathy groups were identified when regional left ventricular function was evaluated.

Our results showed that radial strain obtained by MDCT was in better agreement with radial strain obtained by CMR, compared to comparisons of circumferential strain (Figure 4.5). Radial strain evaluation may be a strength of MDCT due to the high spatial resolution of the method (less than 1 mm). This should allow accurate tracking of high contrast regions at the endocardial and epicardial borders. However, for mid wall circumferential strain, no CT features are typically available for tracking. By comparison, CMR grids allow accurate tracking of mid-wall circumferential strain. In our study as well as that of Helle-Valle (98), MDCT showed improved speed of analysis compared to CMR tagging.

4.5.1 Limitation

Limitations of this study include high temporal resolution for cine MDCT function, which may result in high radiation exposure. Technological innovations in model-based iterative reconstruction and low kVp imaging are tools that have resulted in lower radiation dose. The number of animals in each group was small, and larger sample sizes may have shown that global function parameters could detect differences between groups. Ultimately, translational studies in humans are needed, although generally histologic information is not available in human studies.

While our work has established the feasibility of deformation analysis with CCT, continued work needs to be done to make this analysis part of clinical practice. This includes further development and validation of the methods for analysis. More specifically, currently MTT is designed for CMR and echocardiography images. In order to improve the analysis results for CCT, additional work needs to be done to tailor MTT for CCT images.

4.5.2 Conclusion

In conclusion, our results suggest that cine MDCT can be used to detect regional dysfunction in an experimental model of cardiomyopathy in a manner comparable to CMR tagging. This study points to the potential of cine MDCT to allow comprehensive evaluation of myocardial function.

"This article describes a technique in which X-ray transmission readings are taken through the head at a multitude of angles: from these data, absorption values of the material contained within the head are calculated on a computer and presented as a series of pictures of slices of the cranium". Conduct the first clinical CT examination.

—Sir Godfrey Newbold Hounsfield, 1972 (127)

5

Development of CCT Image Acquisition Protocol for Functional Analysis

Contents

5.1 Abstract

Purpose: The latest generation of MDCT scanners offers substantial reductions in radiation exposure for patients combined with high temporal resolution. The purpose of this study was to develop and implement an optimal imaging

protocol for low dose, high temporal resolution functional images as part of a complete cardiac exam.

Methods: A 320-detector row system (Aquilion ONE ViSION, Toshiba Medical systems) was used to for cardiac evaluation. Optimization for functional imaging includes using a three heartbeat acquisition for high temporal resolution, low energy (80kV, 80mA) at high gantry rotation (0.275 s gantry rotation) for lowering radiation dose, and quadra-phasic contrast injection protocol to reduce contrast dose and streak artefacts while maintaining right sided opacification. Third generation adaptive iterative dose reduction image reconstruction was used. Signal to noise (SNR) and contrast to noise (CNR) ratios as well as overall image quality were assessed.

Results: Cardiac functional imaging was performed at radiation levels down to sub-millisievert (mSv) dose (range 0.90-2.4 mSv, median 1.27 (1.16-1.43) mSv) in 52 subjects (mean age 65.5 $\pm$ 6.6) who were referred for coronary artery evaluation. Our protocol provided cine MDCT images with temporal resolution of <50msec and the mean myocardial SNR was 13.6 $\pm$ 6.0 with CNR of 11.4 $\pm$ 5.6 relative to blood pool. Commercial softwares, Vitrea (Vital Images, Minntonka, MN, USA) and syngo.via (Siemens Healthcare, Erlangen, Germany), automatically tracked and calculated RV and LV function.

Conclusion: 320-slice MDCT can perform function imaging of the heart with high image quality and high temporal resolution (<50msec) using approximately 1.2 mSv range radiation compared to approximately 6.3 mSv reported by previous studies. High temporal resolution imaging of the cardiac myocardium is feasible at low radiation doses resulting in comprehensive evaluation of cardiac function and anatomy.

Publication: Work in this chapter has been accepted for presentation at the European Society of Radiology. This work involved the contribution of a multidisciplinary team of physicians, nurses, and technicians. I led and was involved with multiple aspects of the study. Colin Yi (post-baccalaureate student) assisted in measurements for SNR and CNR reporting. Marissa Mallek

and Andrew Sams (registered nurses) assisted with patient recruiting and scheduling. Veit Sandfort, J. Alison Noble, Marcus Y. Chen, and David A. Bluemke all provided guiding input into this work.

5.2 Introduction

From the development of CT technology in the 1970s, CT use in medical imaging has been rapidly increasing (5). For instance the United States and United Kingdom have shown a 20 fold and 12 fold increase in the number of CT performed respectively between 2010 and 1990 (128). This grow is projected to continue (128).

This increase in use led to continue technological advances, especially in terms of multidetector computer tomography (MDCT), which have resulted in lower radiation dose and higher resolution for imaging of the coronary arteries. This has subsequently led to MDCT being proven to be robust and accurate for detection of coronary artery stenosis (129). 64-slice MDCT was compared against the standard of invasive coronary angiography for diagnosis of coronary artery disease and was shown to have a sensitivity of 97%, specificity of 79% and negative predictive value of 96% (130).

The increased research on MDCT for routine coronary imaging (131; 132; 133; 134) leads one to wonder what other potential uses this modality might have. One such area is the potential for comprehensive evaluation of the myocardium, which requires characterization of cardiac function, at both a regional and global level (135).

In order to better investigate this potential use of CCT it is important to develop ways to improve the imaging acquisition protocol, specifically for routine clinical use. Important factors for such images to become part of routine clinical practice include low radiation dose and high temporal resolution. Both of these issues are discussed below.

5.2.1 Radiation Dose Background

With the continued development of different clinical uses for CT, there has been increased concern about radiation-induced cancers (128). In order to address these concerns, steps have been made to reduce radiation exposure (136). Basic information about radiation dose can be found in Appendix C.

5.2.2 Radiation Dose of Cardiac Function Exams

Currently, it is commonly thought that cardiac wall motion functional analysis requires 6.32 mSv (4.69-8.89mSv)of radiation (13; 137). However, myocardial function analysis can be performed at higher noise levels and subsequently lower radiation doses than required for coronary artery evaluations due to robustness of the analysis to noise. With newly developed technology and acquisition methods, it may be possible to produce CCT images for functional analysis at lower radiation exposures than currently widely accepted.

5.2.3 Temporal Resolution of Cardiac Function Exams

While spatial resolution can be considered image detail, temporal resolution can be considered the smallest window of time captured and is an important factor to consider with cardiac functional analysis. Temporal resolution preservation is well investigated in echocardiography and CMR (138; 139). Investigators have begun investigating improvements in the temporal resolution of cardiac CT (140). Enhanced temporal resolution improves the quantitative assessment of LV function (141; 142), and regional function analysis.

5.2.4 Methods of Decreasing Radiation Dose and Improving Temporal Resolution

We will now discuss a few key variables that affect both radiation dose and temporal resolution.

5.2.4.1 Patient Selection

CT scans should only be performed when the benefits of the scan outweighs the potential risk of radiation exposure. A number of societies including the Society of Cardiovascular Computed Tomography, the American College of Radiology, the AHA, the ASE, the American Society of Nuclear Cardiology, the North American Society for Cardiovascular Imaging, the Society for Cardiovascular Angiography and Interventions, and the SCMR came together to develop guidelines for appropriate use of CT (5).

5.2.4.2 Tube Potential

Tube potential (electrical potential across the X-ray tube) determines the energy of the X-ray beam and is measured in peak kilovoltage (kVp). It is common to see CT studies in adults performed at 120 kVp. It is known, however, that reducing the tube potential from 120 to 100 kVp can reduce radiation up to 53% (143). This reduction in radiation comes at a cost of increasing noise by up to 26% (143). All other factors held constant, radiation dose change between two different kVps is approximately proportional to the square of the percentage change in tube potential as expressed in the following equation:

$$\Delta CTDI_{vol} \propto \left(\frac{kV_{new}}{kV_{old}}\right)^{n} \tag{5.1}$$

where $CTDI_{vol}$ is Volume Computed Tomography Dose Index, kV_{new} is the new tube potential, kV_{old} is the old tube potential, n $\approx$ 2 to 3. It is therefore understood that tube potential can play an important role in radiation dose. For example, if kV_{new} is 80 and kV_{old} is 120 and we approximate n to be 2.5, this will give a = $\Delta CTDI_{vol}$ of .36 or a 64% reduction in radiation dose if mA is held constant.

5.2.4.3 Tube Current

Tube current (mA) is the number of electrons accelerated across the X-ray tube per unit of time and is therefore proportional to the number of X-rays being

produced (X-ray fluence). This metric is directly proportional to radiation dose as seen in the equation below:

$$\Delta CTDI_{vol} \propto \Delta TubeCurrent \tag{5.2}$$

where $CTDI_{vol}$ is Volume Computed Tomography Dose Index.

5.2.4.4 Exposure Time

Another important factor relating to radiation dose is exposure time, with an increase exposure time leading to an increase radiation exposure. A number of factors relate to exposure time, including the detector configuration, pitch of the scan, and gantry rotation time. We shall now go into detail on each of these terms.

Detector configuration is formed by the number of channels or arrays (a) and the width of each channel (T). The configuration can be used to calculate the scan coverage according to the following:

$$coverage = aT \tag{5.3}$$

For example, a 2 row detector with 0.5 mm width of each channel (i.e. 2 x 0.5) provides 2 mm of coverage.

A CT scan's pitch is the ratio of table movement to the detector collimation. This is an important consideration in helical scans, as the amount of overlap between beam width at each view angle can affect radiation dose (i.e. more overlap (high pitch) would indicate more radiation exposure).

Finally, there is gantry rotation time which defines the amount of time required to complete one 360^o rotation of the X-ray tube and detector around the subject. Faster gantry rotation time implies shorter exposure time and therefore lower radiation doses. In addition, faster gantry rotation time improves the temporal resolution of the images. In order to reconstruct an image, only $180°$ [1] of data is required since the remaining $180°$ are simply a mirror image

[1] Technically $180°$ plus the fan angle.

of the first. This is due to the fact that it does not matter which direction a photon travels through tissue, it will be attenuated the same amount. Therefore, if the gantry rotation time is 0.275 s, then the temporal resolution of the image is 0.138 s.

5.2.4.5 Multi-Segment Reconstruction

A key consideration with functional imaging is temporal resolution. Accepted temporal resolutions for different modalities are presented in Table 2.1. Multi-segmental image reconstruction combines consistent projection data belonging to the same motion state from a number of consecutive heartbeats to fill all needed projections for a complete image. By doing so, it is capable of increasing the temporal resolution of CT images (144). This works because a multi-cycle approach reduces the rotational arc of the gantry required to produce an image.

The maximal temporal resolution (TR_{max}) can be calculated as follows:

$$R_{max} = \frac{G_{RT}}{2M} \tag{5.4}$$

where R_{max} is the maximal temporal resolution, G_{RT} is the gantry rotation time, and M is the number of segments in adjacent heartbeats from which projection data are used for image reconstruction (145).

5.2.4.6 Image Reconstruction

Towards our goal of low noise images, post-processing becomes an important factor. Iterative reconstruction is a statistical reconstruction method where project data is predicted based on assumptions about the initial attenuation coefficients of all voxels. The subsequent predicted data is compared to measured projection data and the voxel attenuation values are modified until an acceptable error level is achieved. This technique is associated with lower noise levels than the previous standard of filtered back projection, and therefore a lower tube potential and current can be used (146).

5.2.5 Rationale and Specific Aim

Continued interest in evaluating regional cardiac function beyond the LV (147) and improved visualization of all chambers of the heart may prove useful. Given the possibility of using a state-of-the-art 320 detector row MDCT (133), capable of imaging the entire heart within a single heartbeat and without additional radiation exposure due to over scanning (148), steps towards whole heart functional analysis can be achieved.

5.3 Materials and Methods

5.3.1 Cine CT as Part of Complete Cardiac Exam

A key goal of the development of this protocol is to have it be a part of a complete cardiac exam. Research suggest that a dedicated scan with consistent multiphase CNR is possible (149). This is opposed to ECG-based dose modulation, where tube current varies according to the phase within the cardiac cycle. With this consideration in mind, the following protocol, as seen in figure 5.1, was created.

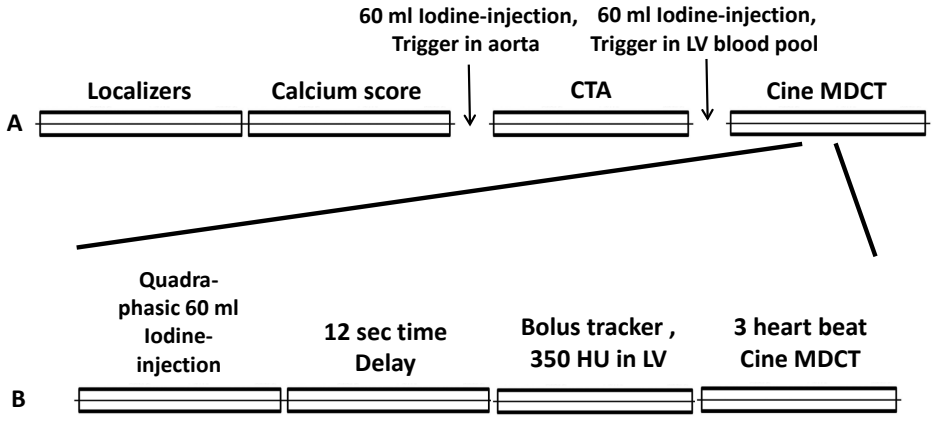

Figure 5.1: ***Calcium Score, Coronary and Functional Computed Cardiology Scan.*** *A. Dual injection CCT protocol with CTA (CT angiography) and cine CT for functional analysis. B. Details of cine CT protocol*

5.3.2 Rationale of Cine CT Parameters

As explained above, the ultimate goal of these images is to provide low radiation dose, high temporal resolution cine CT images that can be used for functional analysis of the heart. Having provided an introduction to the key variables affecting radiation dose and temporal resolution, we shall now discussed how each of these factors were incorporated into our specific exam.

5.3.2.1 Patient Selection

Based on this information from (5), the following exclusion criteria were used: patients who were pregnant, had a glomerular filtration rate <45 mL/min/m^2, or a body mass index (BMI) $\geq$ 30. These exclusion criteria are to avoid X-ray exposure to foetal development, avoid injecting contrast in patients who will have difficulty filtering and eliminating it, and to avoid patients where a potentially dangerous level of radiation exposure would be necessary to provide the necessary image quality, respectively.

5.3.2.2 Tube Potential

Given that myocardial functional imaging can potentially tolerate higher noise thresholds, it was decided that reduction of radiation was the priority. Therefore, any steps towards adjusting tube potential according to weight and size to tube potential was postponed till later iteration of the protocol. A key consideration at lower tube potentials is that there are higher attenuation values, especially for contrast agents like iodine. This is due to the increased linear attenuation coefficient of iodine relative to that of water (150). Additional information can be found in Appendix A.3. This fact can help reduce the amount of intravenous contrast needed for the scan. In order to ensure low radiation exposure, a tube potential of 80 kVp was selected in this study. Also, a beam at 80 kVp will have an average X-ray energy near 30 KeV which is near the k-edge of iodine. This level of tube potential is often considered to be on the lower range of tube currents used in CCT.

5.3.2.3 Tube Current

Unlike tube potential, tube current does not affect image attenuation values and reduction of tube current is the most frequently used method to affect radiation dose. In order to ensure low radiation exposure, a tube current of 80 mA was selected in this study, considered to be on the lower range of tube currents used in CCT.

5.3.2.4 Exposure Time

In this study, a detector width of 0.5 mm was used for 320 channels (i.e. a detector configuration of 320 x 0.5 mm), giving a 16 cm coverage (i.e. beam collimation of 16 cm). Given that the 320 slice scanner used in this study is able to cover the the entire heart with one rotation of the gantry, there is no pitch in this examination. The scanner in this study allows for fast gantry rotation times of 0.275 s which was used.

5.3.2.5 Multi-Segment Reconstruction

Given this information, we decided to perform a three heart beat segmentation method towards improving temporal resolution. This allows for a maximal temporal resolution of approximately 48 milliseconds.

5.3.2.6 Image Reconstruction

Decisions were made about type of image reconstruction, kernel selection, post-processing slice thickness, and step intervals.

The specific image reconstruction method selected for this study is Adaptive Iterative Dose Reduction in 3D (AIDR 3D) (151; 152). AIDR 3D works in two stages. The first part adaptively removes photon noise in the 3D raw data domain, followed the second stage involving a model-based iterative noise reduction in the reconstruction process.

Another important consideration in image reconstruction is the reconstruction kernel (also known as a referred to as a filter). The standard FC03 kernel

was used(153; 154) as it is meant for optimizing visualization of soft tissues such as the myocardium.

Finally, post-processing slice thickness can also affect the appears of the images. In order to maintain isotropic voxel for reformatting of images, 0.5 mm slice thickness was used. A method of post-processing to reduce noise would be to increase the slice thickness, however this may also have the effect of losing the isotropic voxel qualities possible with MDCT.

5.3.3 Summary of key MDCT Parameters

Cine MDCT imaging was performed with a second-generation, 320 x 0.5 mm detector row CT unit (Aquilion ONE ViSION Edition; Toshiba Medical Systems, Otawara, Japan). Images were reconstructed with a 512 x 512 matrix and 0.5 mm z-thickness. AIDR 3D (Toshiba Medical Systems), with Kernel FC03 was used. Optimization for functional imaging included using a three heartbeat acquisition for high temporal resolution, and low energy (80 kV, 80 mA) at 0.275 s gantry rotation speed for lowering radiation dose at a high temporal resolution. Details of the scanner protocol for replication can be found in Figure 5.2.

5.3.4 Summary of Contrast Protocol and User Protocol

Contrast agents are selected based on two properties. One, they are nontoxic even at high doses they have a significantly different attenuation coefficient allowing for differentiation from surrounding tissues and two, they are nontoxic even at high doses. One such agent with these properties is iodine, which is used in this study. The contrast agent, Iopamidol (Isovue 370, Bracco Diagnostics, Princeton, NJ; 370 mg of iodine per milliliter).

The goal of this scan is to have clear visualization of all four chambers of the heart while limiting contrast use. To achieve this goal, contrast was injected via antecubital vein with a quadra-phasic protocol, which consists of 40 mL of contrast material then 16 mL of saline, then 20 mL of contrast,

and finally 20 mL of saline. Quadra-phasic contrast injection protocol has the benefits of reducing contrast dose and streak artifacts, while maintaining right sided opacification. Breath-hold contrast-enhanced images were triggered within 1 second of a threshold of 350 HU by using bolus tracking within the left ventricle. Bolus tracking images were initiated 12 seconds after the start of contrast material administration.

5.3.4.1 Detailed Scanner Protocol

Detailed scanner parameters are shown in Figure 5.2. The two "Scanogram" are the CT localiser radiograph, which is often acquired to allow the user to prescribe the start and end locations of the scan range. The Scan and View (S and V) mid volume is used to plan a single CT scan, in our case the CCT. "SureStart" allows for contrast bolus tracking. Finally, "Volume" is the cine MDCT settings, which is the clinical data of interest. With this information it is possible to programme other scanners and replicate our scans.

5.3.5 Study Protocol

This prospective study was performed as part of a single referral centre and is registered at clinicalTrials.gov (registration no. NCT01212900). The institutional review board approved the study and all patients provided written consent.

5.3.6 Study Cohort

Our study population included men and women $\leq$ 55 years of age who were candidates for lipid lowering therapy under the National Cholesterol Education Program - Adult Treatment Panel III guidelines, without contraindication to statin therapy. As previously mentioned, exclusion criteria included patients who were pregnant, had a GFR <45 mL/min/m^2, or a BMI $\geq$ 30.

Carotid Cardiac Function

EP No: 122

Scanogram - AP Scanogram Above shoulders to below liver									
Scan mode	**Start time (s)**	**Wait time (s)**	**kV**	**mA**	**Range (mm)**	**Direction**	**Display filter**	**Scano angle**	**CE**
Scanogram(AP)	0.00	0.00	120	50	500.0	OUT	Sharp (FL03)	0	OFF

Scanogram - Lateral Scanogram									
Scan mode	**Start time (s)**	**Wait time (s)**	**kV**	**mA**	**Range (mm)**	**Direction**	**Display filter**	**Scano angle**	**CE**
Scanogram(Lat)	0.00	0.00	120	100	500.0	IN	Sharp (FL03)	90	OFF

S&V - Mid volume															
Scan mode	**# of scan**	**Start time (s)**	**Wait time (s)**	**Collimation**	**Pitch**	**kV**	**mA**	**Rotation time (s)**	**Total scan time (s)**	**Range (mm)**	**Direction**	**CFOV**	**CE**	**CTDIvol (mGy)**	**DLP (mGy.cm)**
S&V	1	***	0	0.5 x 4	***	80	80	0.275	0.275	2	OUT	M	OFF	2.00(Body)	0.40(Body)

Reconstruction	**Slice thickness**	**Slice interval**	**DFOV**	**SURE IQ**	**Recon Process**	**FC**	**Boost 3D**	**OSR**	**Filter**	**SEMAR**
Axial1	2.0 mm	***	220	Sft Tissue - SureStart	OFF	10	OFF	***	OFF	***

SureStart - Trigger in the (LV) Left Ventricle at 180 HU															
Scan mode	**# of scan**	**Start time (s)**	**Wait time (s)**	**Collimation**	**Pitch**	**kV**	**mA**	**Rotation time (s)**	**Total scan time (s)**	**Range (mm)**	**Direction**	**CFOV**	**CE**	**CTDIvol (mGy)**	**DLP (mGy.cm)**
SureStart	***	***	14	0.5 x 4	***	80	80	0.275	40.425	0	***	M	ON	267.00(Body)	53.40(Body)

Reconstruction	**Slice thickness**	**Slice interval**	**DFOV**	**SURE IQ**	**Recon Process**	**FC**	**Boost 3D**	**OSR**	**Filter**	**SEMAR**
Axial1	2.0 mm	***	220	Sft Tissue - SureStart	AIDR 3D	10	OFF	***	OFF	***

Volume - 1cm above LM coronary to 1cm below apex of heart														
Scan mode	**# of**	**Start**	**Wait**	**Collimation**	**Pitch**	**kV**	**mA**	**Rotation**	**Total**	**Range**	**Direction**	**CFOV**	**CE**	**CTDIvol (mGy)**	**DLP (mGy.cm)**

	scan	**time (s)**	**time (s)**					**time (s)**	**scan time (s)**	**(mm)**					
Volume ECG Gated Prospective	1	0	0	0.5	***	80	80	0.275	3.176	140	OUT	M	ON	7.10(Body)	100.00(Body)

Reconstruction	**Slice thickness**	**Slice interval**	**DFOV**	**SURE IQ**	**Recon Process**	**FC**	**Boost 3D**	**OSR**	**Filter**	**SEMAR**
Volume1 (75%)	0.5 mm	0.25 mm	220	Cardiac - CTA	AIDR 3D Standard	3	OFF	Cardiac	OFF	OFF

Figure 5.2: ***Cardiac Function Toshiba Protocol.*** *The parameters necessary to program a Toshiba 320-row scanner to perform our scans.*

5.3.7 Estimation of Radiation Dose

5.3.7.1 Radiation Absorbed Dose in Computed Tomography

Volume Computed Tomography Dose Index, $CTDI_{vol}$, is a metric reported by manufacturers of CT scanners that provides information regarding the radiation dose of either a 16 cm (for head examination) or 32 cm (for body examination) diameter acrylic phantom (155). It is considered to be the international standardized parameter to measure CT scanner radiation output and has units of mGy (see appendix C for more info about radiation). However, it is important to remember that no information about patient size is included in $CTDI_{vol}$ and is not representative of patient dose.

The dose length product (DLP) is the CTDIvol multiplied by the scan length in cm and is measured in mGy.cm. DLP is used to calculate effective dose by a conversion factor of 0.014 $\frac{mSv}{mGy.cm}$ for the chest, according to standard methodology outlined in the most recent guidelines for chest scans (146; 156). This conversion factor accounts for the exposed body region and not the patient's age, sex or size.

5.3.7.2 Better Factoring of Body Size: Size Specific Dose Estimate

A noted issue with $CTDI_{vol}$ and DLP is that for a small or large patient, at a given scanner setting, the value is the same. The AAPM report 204 (157) describes a method to account for patient dimensions using a metric called size specific dose estimate (SSDE). These patient dimension metrics are the anterior-posterior (AP) width, lateral width, and a combination of AP and lateral measurements (i.e. effective patient diameter). Effective patient diameter as used in our study. Subsequent studies suggest using a combination of AP and lateral measurements whenever possible for the most accurate results (158). SSDE is calculated according to the following equation:

$$SSDE = f_{size} \cdot CTDI_{vol} \tag{5.5}$$

where SSDE is size specific dose estimate, and f_{size} is tabulated size-dependent conversion factors as provided in (157).

It is important to note that SSDE is still not the exact patient dose as other factors including scan length and patient tissue composition may differ from the assumption used to calculate SSDE. This leads to reporting CDTI, DLP, effective dose and SSDE.

5.3.8 Image Analysis

Images were transferred to a dedicated post-processing workstation (Vitrea, Vital Images, Minntonka, MN, USA). Image quality was accessed with standard indices including signal-to-noise (SNR) and contrast-to-noise ratio (CNR). Signal Intensity was defined as the attenuation value of a 30 mm^3 region-of-interest (ROI) obtained in the LV cavity and myocardium. The image noise was derived from the standard deviation of the CT attenuation value in the LV cavity. SNR was the signal intensity attenuation value divided by the SD. Finally, the CNR was defined as the difference between the attenuation values of the LV and myocardium divided by the image noise.

LV and RV functional analysis of the cine MDCT images were performed on a dedicated post-processing Vital, Vitrea and syngo.via workstation.

5.3.9 Statistical Analysis

Statistical analyses were performed with MedCalc 12.0 (MedCalc Software, Mariakerke, Belgium). Continuous variables are presented as mean ± standard deviation or the median with interquartile range (IQR). Categorical variables were expressed as percentages.

5.4 Results

5.4.1 Demographics

Overall, the age of the 52 subjects was 65.5 ± 6.6 years; 31 (59.6%) were male. The subjects had an BMI of 26.7 ± 2.3, with 37 (71%) patients being overweight or obese. The average heart rate (HR) of the subjects was 63.5 ± 9.8 beats/minute . It is important to note that HR ranged from 20 to 97. 38.5% (20 out of 52 patients) were on beta blockers due to a pre-existing condition.

Variable	Value
No. of men (n)	31 (59.6)
Mean age (year)	65.5 ± 6.6
Mean height (cm)	171.5 ± 8.7
Mean weight (kg)	77.6 ± 11.7
BMI (m/kg^2)	26.7 ± 2.3
HR (beats per minute)	63.5 ± 9.8
Beta blocker (n)	20 (38.5)
Median CTDIvol (mGy)	7.3 [6.9, 8.3]
Median DLP (mGy.cm)	90.6 [82.7, 101.9]
Median estimated effective dose (mSv)	1.27 [1.16, 1.43]
Mean effective patient diameter (cm)	25.8 ± 2.2
Median size-specific dose estimate (mGy)	10.6 [9.9, 11.9]

Table 5.1: ***Patient Characteristics and Radiation Dose Data (n=52).*** *mean ± SD, mean (%) or median [IQRs].*

5.4.2 Radiation Dose

The median dose-length product for all 52 scans was 90.6 [82.7, 101.9], corresponding to an estimated effective dose of 1.27 [1.16, 1.43] mSv. The radiation dose was less than 1mSv in 8% of the CT examinations (4 of 52 patients), less than 1.5 mSv in 84.6% (44 of 52 patients), and less than 2 mSv in 96.2% (50 of 52 patients).

The radiation dose data are summarized in Table 5.1. The median $CTDI_{vol}$ was 7.3 [6.9-8.3] mGy, and the mean effective patient diameter was 25.8 cm ±

2.2, yielding a median SSDE of 10.6 mGy [9.9, 11.9] mGy.

5.4.3 Image Quality

Image quality was diagnostic for assessment of regional wall motion abnormalities and global function in all subjects. The difference between three heart beat reconstruction and one heart beat reconstruction can be observed as seen in Table 5.2. The HU value of the blood pool and myocardium was not statistically different with the reconstruction as expected, although the standard deviation did change. The SNR was 13.6 ± 6.0 with CNR of 11.4 ± 5.6 for the three heart beat reconstruction compared to 8.8 ± 6.3 SNR and 7.2 ± 6.3 CNR for the one heart beat reconstruction (Table 5.2).

	3 Heart beat reconstruction	1 Heart beat reconstruction
Blood pool (HU)	548.3 ± 44.4	560 ± 70.8
Myocardium (HU)	87.7 ± 33.5	106.2 ± 63.6
SNR	13.6 ± 6.0	8.8 ± 6.3
CNR	11.4 ± 5.6	7.2 ± 6.3

Table 5.2: ***Spatial Resolution Quality.*** *means ± SD.*

Commercial available software automatically tracked the myocardium for functional analysis. Visual inspection of tracking shows videos with various commercial cardiac analysis systems (Figure 5.3). Visual inspection can also be performed across the cardiac cycle as seen in Figure 5.3.

5.5 Discussion

This study describes the feasibility of performing a cardiac CT scan for assessment of cardiac function with not only high temporal resolution of <50 msec, but also low radiation exposure. This achievement is possible due to several recent of advancements in cardiac CT technology (159), which includes development of a 320 detector row scanner. These systems provide excellent image quality for coronary evaluations over a wide range of body sizes and heart

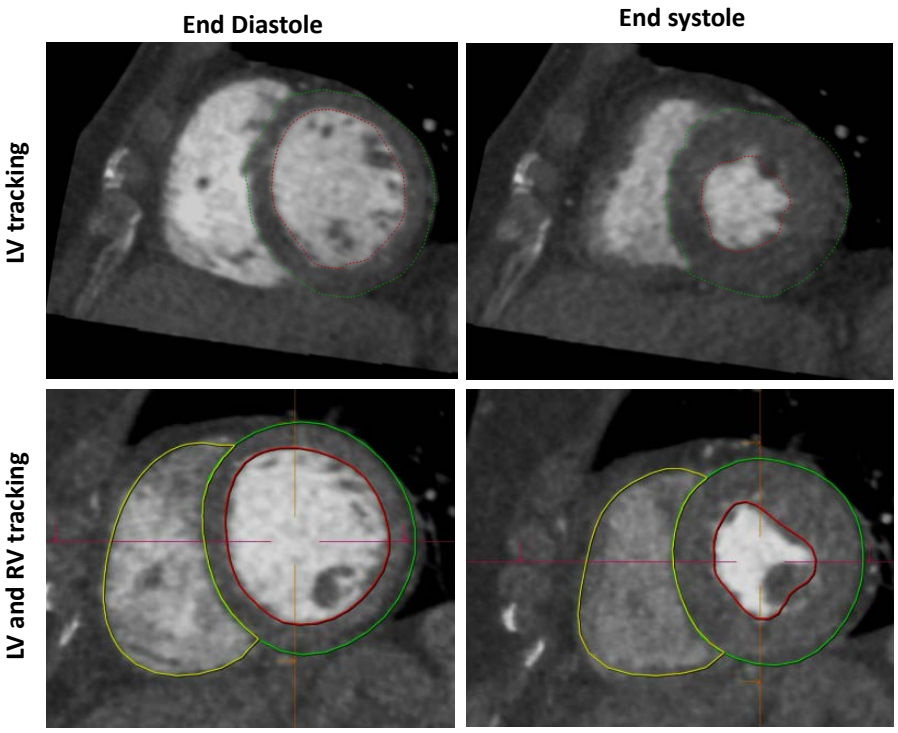

Figure 5.3: ***Segmentation for Functional Analysis.*** *Accurate segmentation of the left ventricle and right ventricle were observed by two different commercial packages: Vitrea (Vital Images, Minntonka, MN, USA), and syngo.via (Siemens Healthcare, Erlangen, Germany).*

rates at lower radiation doses than previous first-generation scanners (132). Evaluation of cardiac function is important in the assessment systolic function, especially in HF patients with intra-cardiac defibrillators and resynchronization devices who cannot have CMR, patients who are unable to lie flat or hold their breath for prolonged periods of time to complete a CMR, and where echocardiography is not adequate due to poor acoustic windows. Our study shows that radiation dose for the assessment of cardiac function is approximately 5 fold lower than conventional scans (137).

In terms of image quality, it was noted that our method leads to improved SNR and CNR ratios as well as a decrease in noise represented by standard deviation in HU as seen in Table 5.2. Also the difference between the HU attenuation of the myocardium and contrasted-enhanced blood pool shows a 5-fold difference. These spatial resolution parameters help explained the good

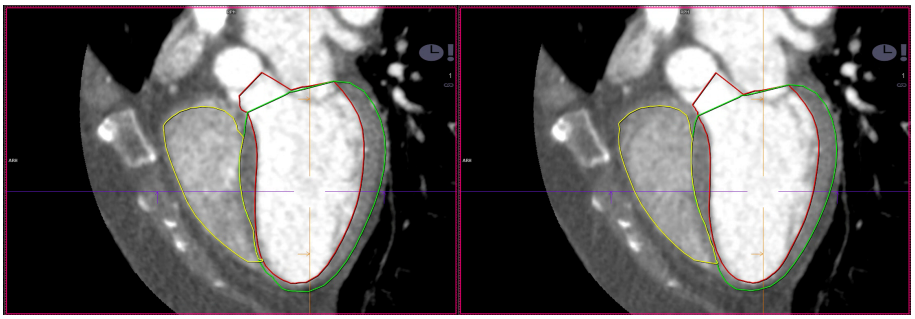

(a) *frame 1* **(b)** *frame 2*

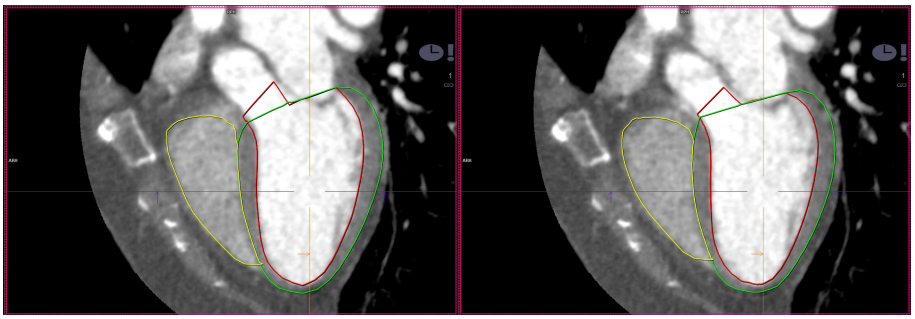

(c) *frame 3* **(d)** *frame 4*

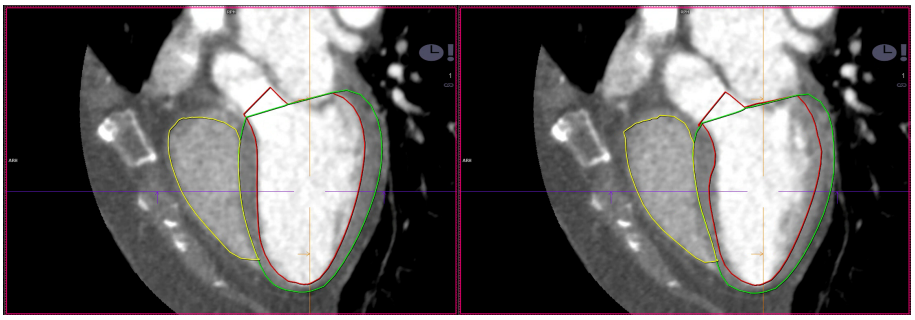

(e) *frame 5* **(f)** *frame 6*

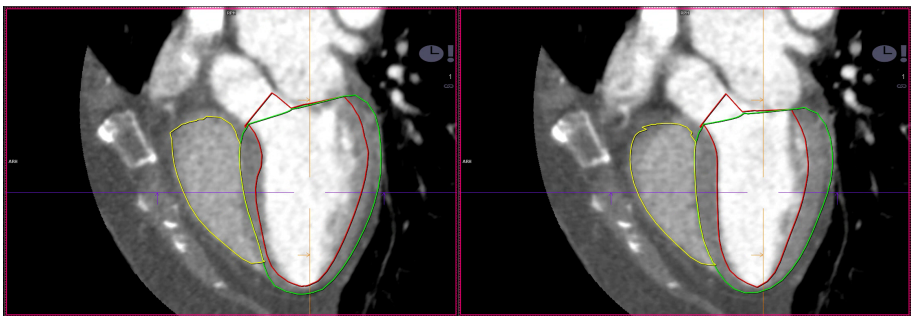

(g) *frame 7* **(h)** *frame 8*

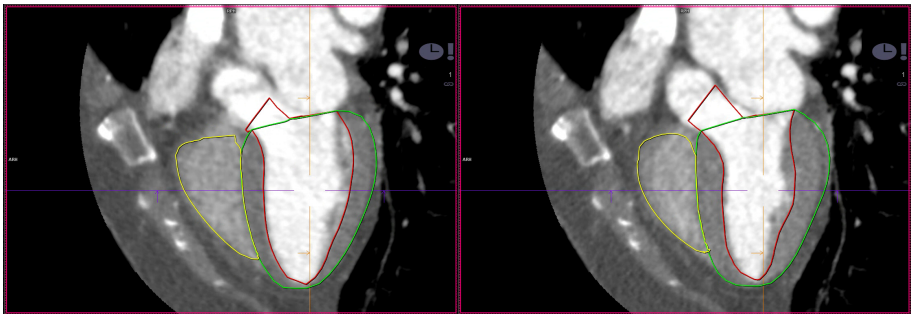

(i) *frame 9* **(j)** *frame 10*

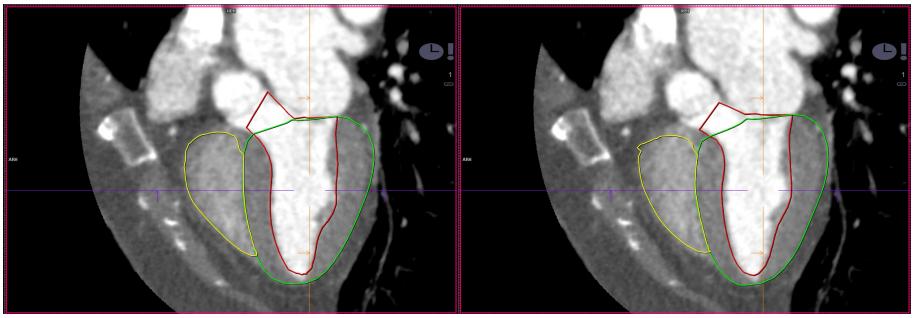

(k) *frame 11* **(l)** *frame 12*

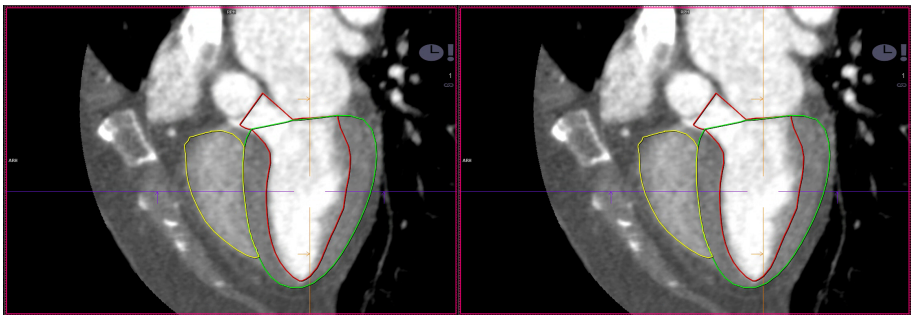

(m) *frame 13* **(n)** *frame 14*

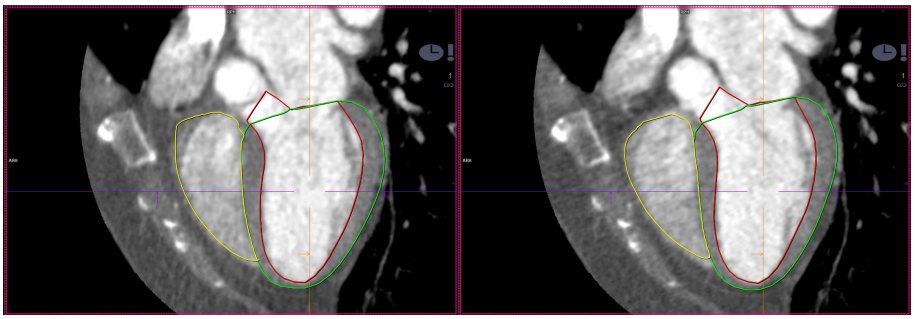

(o) *frame 15* **(p)** *frame 16*

Figure 5.3: ***Functional Analysis of LV and RV Across the Cardiac Cycle.*** *Visual inspection of the automatic tracking indicates the potential of accurate functional analysis these these images.*

performance in automatic tracking of the myocardium as noted in Figure 5.3 and Figure 5.3.

Although, once though that CT could only achieve temporal resolutions of 83 to 175 ms (160), it is now known that the temporal resolution with multi-segment reconstruction is approaching those of other modalities such as MR (34.3ms (161)) and echocardiography (between 33 to 66 ms (160)).

Changes to default acquisition protocols included using a three heartbeat acquisition with 0.275 s gantry rotation time for high temporal resolution, low energy (80 kV) to maximize contrast opacification and reduce radiation exposure, and a quadra-phasic contrast injection protocol to reduce overall contrast amount and streak artifacts while maintaining right sided opacification. AIDR3D working in both projection and image space also enabled reduction in radiation dose while reducing image noise and preserving image quality (162).

5.5.1 Future Direction for Functional cinCT Analysis

There are a number of next steps that have the potential to improve the images obtained from this protocol. These steps include the following:

- Allowing contrast dose to account for differences in patient size and heart rate
- Automatically adjusting tube potential and tube current according to patient size

5.5.1.1 Optimizing Contrast Related Factor: Account for Patient Size and Cardiac Output

In this investigation, a single injection protocol was used. There are two main patient-related factors influencing contrast enhancement that should be considered, including body weight and cardiac output.

Much like how the size of the patient affects image quality and radiation dose, it also affects the contrast dose (163). Because larger patients have a

larger blood volume, contrast medium administered to the blood compartment will be diluted more than that administered to smaller patients. The magnitude of contrast enhancement is inversely related to patient weight in a linear fashion. In order to ensure constant enhancement across a range of patient sizes, the amount of iodine (either by contrast medium volume or contrast medium concentration) should be scaled to patient weight.

Timing of enhancement is largely unaffected by patient size, but is, however, affected by patient cardiac output (164). As cardiac output decreases, the circulation of contrast medium slows and results in delayed contrast bolus arrival, and delayed peak enhancement. Results can be improved using bolus trackers though there can still be issues in cases of extremely low cardiac output such as HF. Often bolus trackers have an automatic termination function to prevent overexposure of radiation to the patient. Therefore, if the bolus does not reach the area of interest fast enough or not in a high enough concentration, the scan will not occur. In order to address this issue, cardiac output should be noted before examination whenever possible. In cases of low cardiac output, adjustments to the scan delay/bolus tracking should be made.

5.5.1.2 Optimizing Scanner Related Factors: Automatic Exposure Control

Modern scanners often provide Automatic Exposure Control (AEC), which automatically adapts the tube current or tube potential according to patient attenuation to achieve a specific image quality. An issue with using AEC is that is may increase $CTDI_{vol}$ for larger patients relative to a reference patient size. AEC systems can adjust according to a number of factors including angular tube current modulation, longitudinal tube current modulation, ECG-based tube current modulation, organ-based tube current modulation, and automatic tube potential selection.

It was decided in this study to not use AEC in order to better control radiation exposure and to observe the obtained image quality. However, in-

corporation of AEC into further studies could maintain the necessary image quality. Note that when AEC is used, factors such as pitch and exposure time may become independent of $CTDI_{vol}$.

5.5.2 Dual Source Computed Tomography Scanners

A key component of this method is the multi-segmental reconstruction. This methods works well towards improving temporal resolution, but it depends on a relatively stable heart rate. Without a stable heart rate, mis-registration between segments is a concern. As investigations into different cardiac diseases are performed, especially those involving irregular heart rates, other methods might need to be considered for acquiring these images. One such method is using dual source CT scanners.

Dual source technology can also provide a solution to improve temporal resolution. It involves using two X-ray sources at right angles to each other. These two X-ray sources are paired with two and two detectors and are then able to acquire raw data simultaneously in a single heart beat and therefore helps address the issues involving patients with irregular heart beats. In addition, it is possible that dual energy CCT (165) could improve the texture of the cardiac tissue based on the distribution of the iodinated contrast agent in the myocardium.

5.5.3 Conclusion

In conclusion, one mSv range functional cardiac CT with visualization of all 4 chambers and a temporal resolution of 50 milliseconds is feasible on a second generation 320 detector row system due to the combination of gantry rotation time of 0.275 s, multi-heart beat segmentation, iterative reconstruction, and wide area detector coverage.

Part II

Technical Contributions

"A sensitive method was developed for detecting stiffness changes in the left ventricle....". First cardiac strain calculation via in vitro tags.

— Israel Mirsky, 1973 (166)

6

Better Characterization of Myocardial Tissue in CCT

Contents

6.1 Abstract

As a result of technological advances in CCT, there has been increasing interest in investigating CCT's potential capabilities, including cardiac deformation estimation. Cardiac deformation estimation is useful for physicians to identify and quantify potential abnormality in moving segments of the myocardium. Our contribution is a first step towards more accurate motion estimation in CCT. A major issue with motion estimation in CCT is the fact that within the myocardium the tissue appears quite homogeneous and therefore is difficult to track. In order to better characterize the myocardial tissue with CCT, we implemented feature-based attribute vectors containing feature asymmetry (FA) information for image registration. Experimental results of attribute vectors on real clinical CCT data demonstrated reduction in registration error compared to registration done solely on intensity or FA information.

Publication: This section is based on the publication "Application of Feature-Based Attribute Vectors for Improved Image Registration Towards Cardiac Motion Estimation in Cardiac Computed Tomography. *Proceedings of Medical Image Understanding and Analysis*. July 2013." This work involved the contribution of a number of individuals. Test dataset was provided by David A. Bluemke. I led this study and was involved with multiple aspects of the study, including study design, programming implementation, and evaluation. Sana Fathima provided assistance with troubleshooting and programming for this work. J. Alison Noble and David A. Bluemke provided guiding input into this work.

6.2 Introduction

The goal of this chapter is to develop an image processing methodology tailored for functional CCT analysis. As discussed in Chapter 2, the number of CCT studies has increased dramatically as a result of improvements in temporal resolution, spatial resolution, and radiation dose reduction (66). Although

cardiac deformation is well explored in CMR and echocardiography, currently there is no established method to obtain this information from CCT. In order to build on current knowledge, we shall first review the technical methodologies used for functional analysis in CMR, echocardiography, and CCT.

6.2.1 Summary of Different Methods of Motion Estimation

There are a variety of different motion estimation methods developed to quantify the deformation of regional myocardial tissue in ultrasound and MR that may be applicable to CCT. It is possible to classify these methods into three broad categories: marker-based methods, boundary tracking methods, and dense tracking methods.

Marker-based methods include both invasive markers, such as sonomicrometry (24), and non-invasive intensity-based tagged, such as those found in tagged MR (167) or speckle tracking (6; 53). A significant issue with invasive markers is that the markers themselves can alter myocardial motion and are not used clinically due to the significant risk to patients. Existing clinical applications of non-invasive tagging include speckle tracking in echocardiography (6; 53) and tagged MR (167). Currently, CCT is unable to fully replicate the methods used in tagged MR (unable to alter image acquisition to produce tags) and speckle tracking (no speckle or equivalent in CCT images). In addition, pure intensity-based speckle tracking methods would most likely not be successful considering the homogeneous intensity of the tissue.

Boundary tracking methods involve edge detection and motion field estimation (61). However, only sparse displacement estimation along the boundaries can be produced due to the simplification of the problem to a surface model. In addition, boundary tracking methods can suffer from the aperture problem (44), making it difficult to distinguish different physical motions without additional information. These methods strongly depend on accurate segmentation of the myocardium and in general perform poorly within the myocardium (44).

The last general category of motion estimation methods is dense tracking methods, based on optical flow and non-rigid image registration techniques (24). The deformation of image is tracked utilizing the dense image information, in contrast with speckle tracking or boundary tracking methods. Methods applying parametric basis splines produce reasonable motion estimations (24).

6.2.2 Rationale and Specific Aims

Building off this last category of dense tracking, we now considered what is being tracked. As discussed in Chapter 3 the myocardium in CCT lacks a distinct signature pattern to allow for easy motion and strain detection. In order to address this issue, we explored the possibility of characterising the tissue motion via feature-based attribute vectors.

Attribute vectors (168) were originally proposed to improve registration of brain MR images and were subsequently applied to cardiac images (169). The benefit of an attribute vector is that any variable that can potentially characterize the point can be included as part of the vector.

FA (170) is one such variable. While image intensity has been found to be a good attribute for CT image registration, registration can be enhanced by using implicit structural features in a cardiac CT image such as endocardial and epicardial edges. Previous research suggests that local phase derived features such as FA can perform better than intensity based metrics (171). Therefore, we explored this in our research (170).

6.3 Experimental Data

For this preliminary work, a single CCT volume was obtained from a 320 row detector Toshiba Aquilion ONE ViSION CT scanner, chosen to facilitate the acquisition of isotropic volumes of an entire organ within a single rotation of the gantry. The subject was imaged to look for cardiac effects from chemotherapy and no cardiovascular disease was noted. The imaging protocol included ECG

triggering, and a split-bolus protocol with a dual-syringe injector and an initial bolus of contrast followed by saline. A single heart-beat volumetric acquisition was obtained with detectors width of 0.4 mm, voltage of 120 kV, and current from 150-500 mA. Temporal resolution of imaging was 137.5 ms. The matrix space of the original image volume was 512 by 512 by 320 voxels. From this volume, a clinically relevant 2D cardiac four-chamber view was selected for evaluation.

6.4 Methods

6.4.1 Feature-Based Attribute Vectors at Different Scales

The attribute vector (172) is designed to be a morphological signature that minimizes ambiguity in image matching and correspondence detection. If the attribute vector is rich enough to reflect the underlying anatomy, it is able to distinguish areas within the image.

In our work, feature-based attribute vectors are defined to contain a FA measure $a^f(x, y)$ in addition to image intensity information, $a^i(x, y)$. A multi-resolution approach is used, with three different scales, to generate an attribute vector $a(x, y)$ calculated on every pixel (x, y) in image $I(x, y)$ and represented by the equation,

$$a(x,y) = [[a_1^f(x,y) a_1^i(x,y)], [a_2^f(x,y) a_2^i(x,y)], [a_3^f(x,y) a_3^i(x,y)]] \tag{6.1}$$

where $[a_1^f(x, y) a_1^i(x, y)]$ represents fine-level attributes, $[a_2^f(x, y) a_2^i(x, y)]$ represents middle-level represents attributes and $[a_3^f(x, y) a_3^i(x, y)]$ represent coarse-level, global features.

6.4.2 Feature Asymmetry

The general idea of our local phase method is to employ the monogenic signal to characterize each pixel in terms of its local amplitude, local phase, and local

orientation. The monogenic signal is the isotropic extension of the analytic signal to N-dimensions (173; 174) making it useful for medical imaging. Structural information in images is principally contained in the local phase (LP). The 2D slice I^S is first convolved with a band-pass filter $b(x, y)$ to obtain,

$$I^B = [I^B_j(x, y) = b(x, y) * I^S_j(x, y); j = 1, 2, ...n] \tag{6.2}$$

where I^B is the band-pass image, j is the slice number, n is the number of slices, and $*$ denotes the 2D convolution operator. It is necessary to use a band-pass filter because structures exist in the signal at different scales. In order to to get useful information the scale of structure is chosen (i.e. central frequency is selected). Also, the selection of the bandpass filter $b(x, y)$ is an important aspect of the method, and in our proposed approach, an isotropic bandpass log-Gabor filter is chosen (170). The log-Gabor filter is defined in the frequency domain by:

$$b(\omega_x, \omega_y) = exp\left(-\frac{log\left(\frac{\sqrt{\omega_x^2+\omega_y^2}}{\omega_0}\right)}{2log(\sigma)^2}\right) \tag{6.3}$$

where (ω_x, ω_y) is the frequency domain representation of (x, y), ω_0 is the centre-frequency of the bandpass filter which governs what scale structures are picked out by the filter, and ω_0 is a shape parameter that governs the selectiveness of the filter. The log-Gabor is normally defined in the frequency domain because there is no closed-form expression for its time-domain form.

The monogenic signal image "I^M" of I^S is defined as $I^M = [I^B, h_1 * I^B, h_2 * I^B]$, where h_1 and h_2 are the convolution kernels of the Riesz transform [17] defined as:

$$h_1(x, y) = \frac{x}{2\pi(x^2 + y + 2)^{3/2}} \tag{6.4}$$

$$h_2(x, y) = \frac{y}{2\pi(x^2 + y + 2)^{3/2}} \tag{6.5}$$

The I^M components can be represented by scalar-valued even and odd filter responses:

$$e(x,y) = I^B(x,y) \qquad o(x,y) = \sqrt{h_1 * I^B + h_2 * I^B} \tag{6.6}$$

where $e(x,y)$ is the even response, $o(x,y)$ is the odd response, I^B is the log-Gabor bandpass filter image, and h_1 are the components of the Riesz transform.

From the even and odd responses, it is now possible to calculate FA.

$$a^f(x,y) = \frac{\lfloor |o(x,y)| - |e(x,y)| - T \rfloor}{A(x,y) + \epsilon} \tag{6.7}$$

where T is a threshold value that sets the sensitivity of the measure, $\lfloor \rfloor$ is a nontypical shorthand meaning that values less than zero are replaced with zero, and ϵ is a small number that avoids division by zero. Normalizing this by the local amplitude $A(x,y)$ gives a measure of symmetry that is independent of amplitude (i.e. a purely structural metric), which lies in the range between 1 and 0. Local amplitude $A(x,y)$ is calculated by:

$$A(x,y) = \sqrt{e(x,y)^2 + |o(x,y)|^2} \tag{6.8}$$

6.4.3 Registration Methodology Using Feature Attributes

Based on the non-rigid registration methods established in (24), we formulate the motion estimation problem as a hierarchical minimization of the energy function of images of M by N matrix size:

$$E = \sum_{x=1}^{M} \sum_{y=1}^{N} d(a_T(h(x,y)), a_R(x,y)) \tag{6.9}$$

where $a_R(x,y)$ represents the attribute vector of reference image, $a_T(h(x,y))$ represents the corresponding points in the transformed template image and $d(a_T(h(x,y)), a_R(x,y))$ represents the sum-of-squared difference between each attribute pair in the attribute vectors $a_R(x,y)$ and $a_T(h(x,y))$ summed over the entire images. This energy is minimized using a first derivative gradient descent optimization against each attribute class (i.e. FA followed by intensity).

6.4.4 Experimental Design

Validation of the registration was done by both visual and quantitative metrics. Visual validation was performed by examining the "difference image" between the deformed target image and the reference image. A smaller difference, indicated by a more homogeneous appearance, suggest a better registration. We also quantified the error using intensity difference, d_I, for individual points and using mean square error (MSE) (175) for the entire image.

6.5 Results

6.5.1 Visual Comparisons

We compare registration using intensity information alone, FA information alone, and a combination of the two via feature-based attribute vectors. Visual inspection of the registration method is shown in Figure 6.1, d-f. A decrease in the difference between the deformed target image and reference image can be observed as a decrease in the visibility of the difference image (i.e. a more homogeneous difference image). Note that when the target image is deformed with attribute vectors (f), the difference image is more homogeneous than when intensity information alone (d) or FA information alone (e) is used.

6.5.2 Quantified Comparisons

From these difference images we can quantify the registration error. In Table 6.1, we quantify the registration error for points located in the LV wall (which are candidates for cardiac strain analysis) as well as additional clinically relevant points. As seen in Table 1, there is a general trend toward smaller registration error (175) with feature-based attribute vectors, compared with registration error obtained from either intensity or FA information alone.

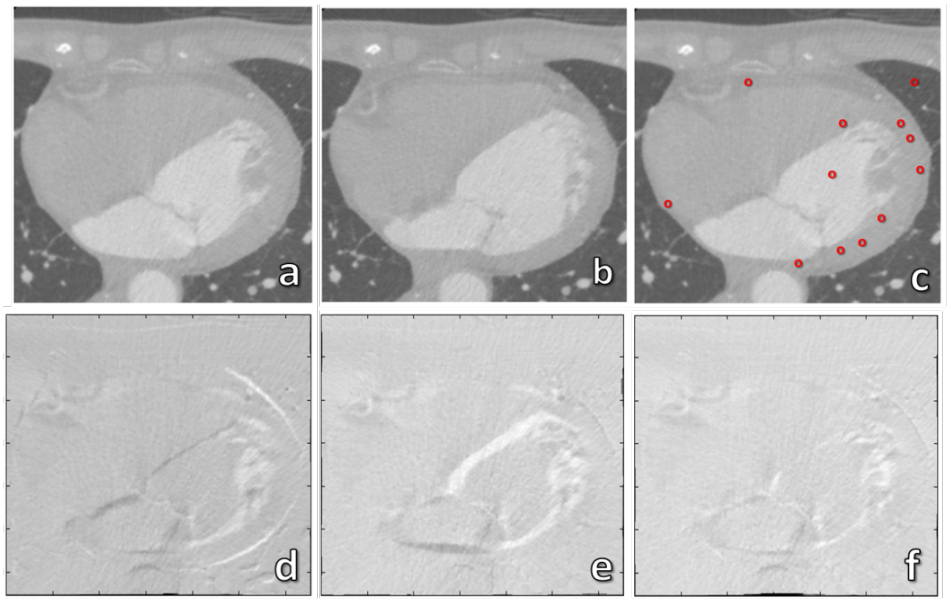

Figure 6.1: ***Visualization of Registration Error.*** *(a) Reference (fixed) image (b) Template (deformed) image (c) Clinically significant points manually selected for quantification in Table 6.1. Difference images between deformed template image and reference image based on (d) intensity information only (e) FA information only (f) attribute vector composed of both FA information and intensity information.*

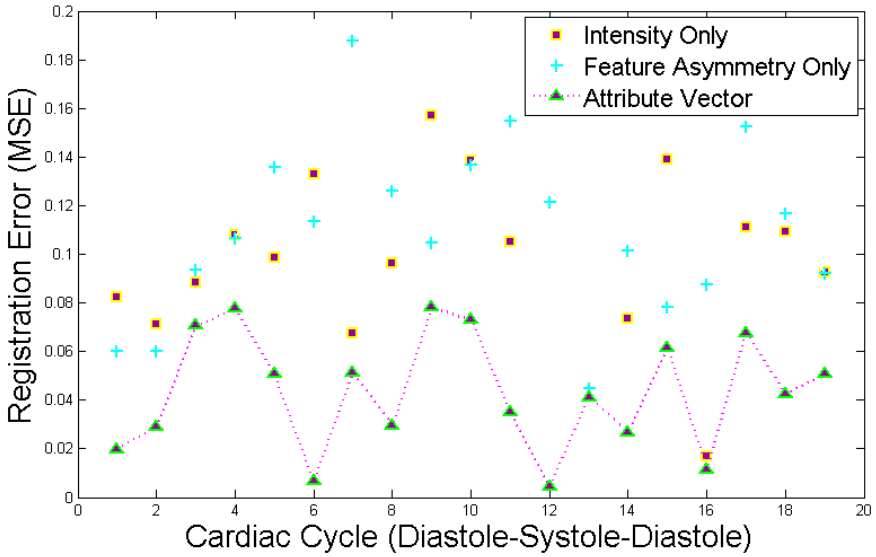

Figure 6.2: ***Quantification of Registration Error Across Cardiac Cycle.*** *Demonstration of the utility of feature-based attribute vectors in reducing registration error (MSE) across a cardiac cycle. Line indicates registration error obtained with feature-based attribute vectors.*

Location	Intensity only	FA only	Attribute Vector
LV wall	3.07	2.72	1.56
LV wall	2.51	2.76	1.95
LV wall	1.22	0.81	0.65
LV wall	4.73	9.50	3.41
LV wall	2.30	2.35	2.03
LV wall	3.65	5.29	3.06
LV wall	0.36	1.06	0.48
LA wall	1.53	1.29	1.1
RV wall	1.96	5.49	1.43
RA wall	0.36	1.06	0.48
LV cavity	0.22	0.81	0.65
lung	1.31	1.95	1.25

Table 6.1: ***Quantification of Registration Error.*** *The intensity difference, d_I, of clinically relevant points were obtained. d_I is to the power of 10^{-2}. Left ventricle (LV), right atrium (RA), right ventricle (RV), left atrium (LA).*

6.5.3 Quantified Comparisons Across Cardiac Cycle

In Figure 6.2, the registration errors, expressed as mean square error (MSE) (175), from the attribute vectors is lower than the registration error observed with the use of FA alone or image intensity alone across the cardiac cycle (from frame 0 to frame 20).

6.6 Discussion

The main contribution is to propose a new image registration method in CCT images, which uses FA within attribute vectors (feature-based attribute vectors).

In our results, we can visually see an improvement in registration with the feature-based attribute vector when compared to registration using intensity or FA information alone. Looking at clinically significant points (i.e. LV, etc.), we have quantified the improvement in registration. Finally, looking across the cardiac cycle, we have found that feature-based attribute vectors consistently showed a lower registration error compared to using intensity information alone

or FA information alone across the cardiac cycle.

6.6.1 Limitation

In Chapter 4, we saw that there are available methods are for 2D strain analysis of CCT. However, as a 2D method, it does not utilize the unique 3D isotropic resolution of cardiac CT image data and therefore does not account for motion outside the image plane. In order to take advantage of the 3D+t nature of CCT data, we next explored the use of a hyperelastic biomedical model in Chapter 7.

6.6.2 Conclusion

Feature-based attribute vectors can be used to better characterize pixels for image registration in CCT.

"Production of in vivo images of the human heart, with delineation of the individual cardiac chambers and myocardial wall thickness, was accomplished by coupling a relatively simple electrocardiographic gating device to a translate-rotate type of computed body tomographic scanner". First attempt at cardiac CT.

—Stuart S. Sagel , 1977 (176; 177)

7

Three-Dimensional Model Based Pipeline for CCT Functional Analysis

Contents

7.1 Abstract

As CCT becomes more commonly available in clinical practice, there is increased interest in regional myocardial strains estimated from CT that has the potential for early quantification and detection of cardiac dysfunction. In our framework, the frame-to-frame displacements on the heart surfaces are computed using B-spline deformable image registration based on mutual information, which are enforced as boundary conditions to a hyperelastic biomechanical model to estimate the myocardial strains. Three principal strains and six strains in cylindrical coordinates can be estimated, and their regional strains are computed in terms of the American Heart Association (AHA) nomenclature (17 zones).

The potential of the estimated strains to identify myocardial infarction in cardiac CT was investigated in this study. Ten canine cardiac CT sequences with artificially induced myocardial infarction were acquired with the infarcted regions identified from perfusion CT on the AHA nomenclature. For each subject, the maximum zonal strain magnitude in the whole cardiac cycle was selected for each zone, and the largest one among all 17 zones was used to compute the normalised zonal strains. As infarcted tissues are usually less contractile, in this preliminary study, the zonal strain magnitudes were used as the inputs to a threshold classifier. Leave-one-subject-out cross validation showed that, by using 'optimal' thresholds computed from ROC curves, the normalised radial strain has the highest performance (TPR: 0.73 ± 0.17, FPR: 0.07 ± 0.04, AC1 coefficient: 0.74 ± 0.15), followed by the normalised first principal strain

(TPR: 0.72 ± 0.20, FPR: 0.14 ± 0.10, AC1 coefficient: 0.66 ± 0.20). We also found that the normalised zonal strains outperform the unnormalised ones.

Publication: This chapter is based on the publication "Myocardial strain estimation from CT: towards computer-aided diagnosis on infarction identification. *Proceedings of the International Society for Optics and Photonics.* (accepted December 2014)". This work had contributions from a number of individuals. Ken Wong and I led development and implementation of this research. The dataset was provided by Marcus Chen. Ken Wong led the programming. Jack Yao, J. Alison Noble, and David A. Bluemke provided guiding input.

7.2 Introduction

As noted in (178), computational models are becoming a fundamental tool in cardiac research. Specifically, deformable biomechanical models have been proven useful in various subject areas and have been shown to be able to solve different types of problems (179; 180). These problems include image segmentation (181), image registration (182), and motion analysis (183; 184). Deformable models are often considered to be driven by internal forces and external forces. External forces are forces that move the model to fit the observations. Internal forces constrain the geometric flexibility of the model. 3D+t spatio-temporal CCT imaging can provide qualitative and quantitative information about the morphology, kinematic function and material properties of the heart. The use of such imaging technology may prove to be beneficial in the diagnosis and treatment of various cardiac diseases.

7.2.1 Rationale and Specific Aims

Cardiac deformation analysis in 3D space has historically been investigated with echocardiography(185; 186) and CMR (187; 188; 189). Extending this

work into CCT, we used a deformable model based approach (190), specifically using a hyperelastic biomechanical model.

7.3 Experimental Data

7.3.1 Animal Preparation

Ten mongrel dogs were used in this study according to protocols approved by the Animal Care and USE Committee of the National Institutes of Health (protocol number H-0104). Weights of the dogs ranged from 25-30 kg.

Anaesthesia was induced by subcutaneous acepromazine (0.2 mg/kg) followed by intravenous thiopental sodium (15mg/kg) and sustained with inhaled sevoflurane (0.5-2.0 %) after intubation. Surgical preparation included a snare around the left anterior descending coronary artery positioned distal to the first diagonal branch. At the start of coronary ischemia, iodine contrast was administered. Five minutes after iodine contrast was administrated, CT imaging was performed. At the end of the experiment the animals were euthanized using potassium chloride.

7.3.2 Multislice Computed Tomography

Multislice CT was performed with a 320 detector row scanner (Aquilion ONE ViSION Edition, Toshiba Medical Systems, Otawara, Japan). The scans were performed with 80 kV tube voltage, 750 mA tube current, 275 ms tube rotation time and a 0.5 mm slice thickness. Intravenous administration of iodinated contrast (Isovue 370, Bracco Diagnostics, Princeton, NJ, USA) was done at 2 mL/kg, divided into two injections to minimize beam hardening effects. The injection protocol occurred in the following sequence: 0.8 mL/kg of contrast at 0.8 mL/s, 0.8 mL/kg saline bolus at 0.8 mL/s, 1.2 mL/kg of contrast at 1.2 mL/s, and finally 1.2 mL/kg saline bolus at 1.2 mL/s. Images were reconstructed at 0.5 mm slice thickness using standard cardiac kernels (FC03) with iterative reconstruction (AIDR3D) at multiple cardiac phases.

7.4 Methods

Myocardial strain estimation can be achieved through biomechanic modelling with finite elements (FE) and deformable image registration, as demonstrated in Figure 7.1. A FE LV model was obtained via image segmentation of the end-diastolic image on each dataset. This provides the tetrahedral mesh of the LV, which is then partitioned into the 17 AHA zones. This heart model is then registered to the first frame of a subject's specific dataset. With the displacement boundary conditions from a separately performed image registration as well as biomechanical properties used as prior knowledge, the FE mesh was then deformed through the biomechanical model to estimate the myocardial strains.

In order to address the lack of distinct patterns or contrast within the myocardium, we implemented a set of constraints on how a surface could deform. These constraints include a smoothness assumption and an incompressibility assumption. While the issue of lack of characterisation of the myocardium still exists, as Chapter 4 illustrates, such characterisation may not be necessary to produce results with CT comparable to the current standard of tagged MR.

Below we discuss each key component of this method: the FE modelling, displacement boundary conditions, and the biomechanics-based myocardial strain estimation.

7.4.1 Finite Element Model

The FE method (191) is a numerical technique developed first for solid mechanics. In our FE method, triangle surface meshes of the myocardium are first created and then used to create a tetrahedral volume mesh according to the following method (192). Figure 7.2 illustrates an FE model of the LV. We chose a tetrahedral mesh over a hexhedra in order to better capture finer geometric details (193). In addition, tetrahedra allow for computations of stiffness matrices, where hexahedra require numerical Gaussian integration which

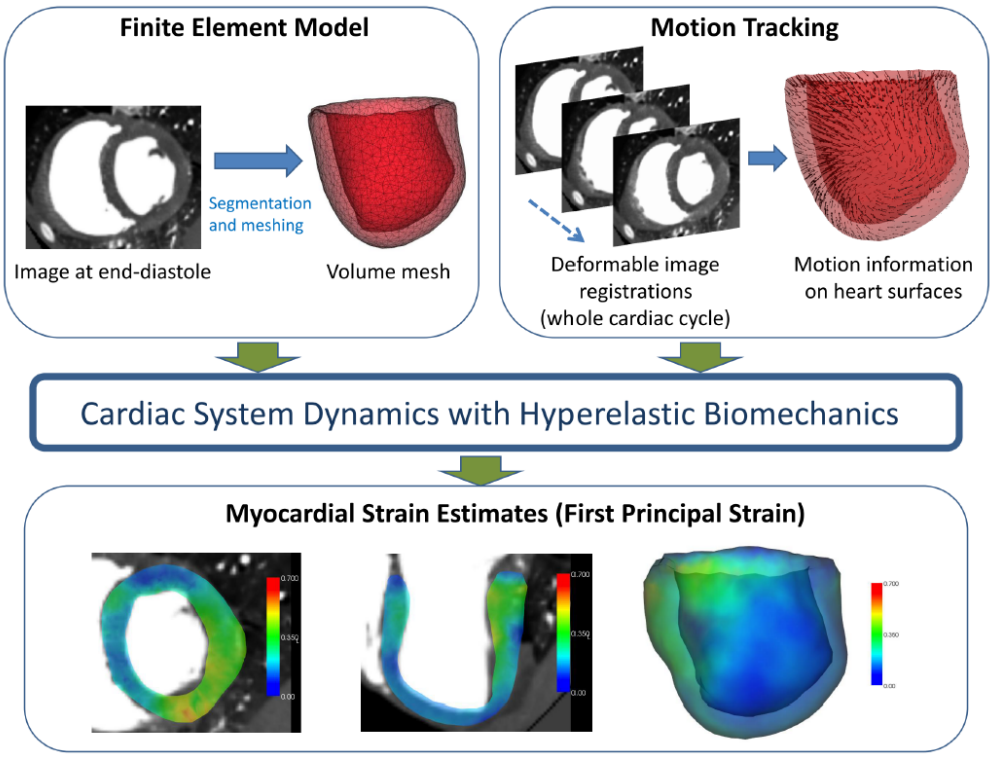

Figure 7.1: ***Biomechanics-Based Myocardial Strain Estimation.*** *Our pipeline can be summarised as follows: image information from the registration is used to determine heart boundary displacements (Fb), which are then used as inputs into the mechanical model (Equation 7.2) in order to calculate internal displacements (F), which are then used to calculate strains.*

is significantly more time consuming.

7.4.2 Displacement Boundary Conditions by Deformable Image Registration

Image-derived displacement boundary conditions, F_b, are required to deform the FE mesh [1]. Without these boundary conditions, the resulting displacement field can lack smoothness and loses clinical meaning. This happens with block matching methods without additional constraints. To address this issue, deformable image registrations based on B-spline interpolation and mutual information were performed on the entire sequence to provide the motion

[1]For clarification, the phrase "boundary conditions" is a mathematical term. The system equation has an infinite number of solutions, so the "boundary conditions" need to be enforced for a unique solution.

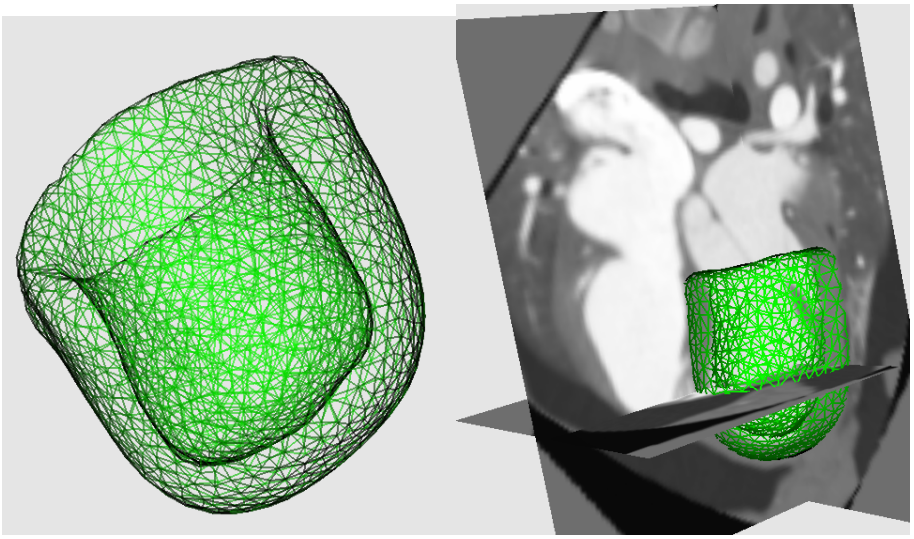

(a) *Tetrahedral Mesh of LV* **(b)** *FEM Overlayed on MDCT Image*

Figure 7.2: ***Finite Element Model.*** *The appearance of an FEM of the LV with and without MDCT.*

information on the heart surfaces.

7.4.3 Hyperelastic Biomechanical Model Towards Strain Estimation

Displacement fields from simple image registration can only provide useful information of the salient features such as cardiac boundaries. In order to address this issue, a deformable model can be a useful solution. Among the different algorithms (194), biomechanical models have attracted much attention for medical image analysis (195). For cardiac tissue that undergoes large deformation, the hyperelastic (i.e. finite strain elasticity) material model can be used to define the biomechanical deformable model (196). The simplest hyperelastic material model is a Saint-Venant-Kirchhoff model. It models the tissue as nearly incompressible and as an isotropic material (197):

$$\psi(\epsilon) = \frac{1}{2}\lambda(J-1)^2 + \mu Tr\left(\bar{\epsilon}^2\right) \tag{7.1}$$

where ψ is strain-energy density, J is the determinant of the deformation gradient tensor F, and $\bar{\epsilon}$ is the isovolumetric part of the Green-Lagrange strain

tensor $\epsilon = \frac{1}{2}(F^T F - I)$. Both F and $\bar{\epsilon}$ therefore can be calculated from F which is computed from the nodal displacements. The first term of equation 7.1 accounts for volumetric elastic response and the second term accounts for isovolumetric (i.e. constant-volume) elastic response. λ represents the bulk modulus, and μ represents the shear modulus. Both moduli are constants that characterises the material whose values are obtained from the literature. In this case, the bulk modulus needs to be large enough for tissue incompressibility. According to the consensus statement by the European Association of Cardiovascular Imaging/ American Society of Echocardiogrpahy/ Industry Task force (1), it is appropriate to assume incompressibility of cardiac tissue. Tr means "trace", or the sum of the diagonal components of a matrix.

In our case, with equation 7.1, the second Piola-Kirchhoff stress tensor "$\frac{\delta\psi}{\delta\epsilon}$" and the elasticity tensor "$\frac{\delta\psi^2}{\delta\epsilon^2}$" can be computed by taking the first and second derivatives of equation 7.1 and embedding into the FE-based total-Lagrangian cardiac system dynamics for the myocardial deformation:

$$M\ddot{u} = C\dot{u} = K\Delta u = F_b - F_t \tag{7.2}$$

where M is the empirically determined mass matrix, C is the empirically determined damping matrix, K is the stiffness matrix produced from the Saint-Venant-Kirchhoff model and comprises both the second Piola-Kirchhoff stress tensor $\frac{\delta\psi}{\delta\epsilon}$ and elasticity tensor $\frac{\delta\psi^2}{\delta\epsilon^2}$ (i.e. the hyperelastic material properties and incompressibility of equation 7.1 is embedded into the stiffness matrix), $\ddot{u}$ is the acceleration vector, $\dot{u}$ is the velocity vector, and Δu is the incremental nodal displacements vector. F_b contains the displacement boundary conditions from image registration as discussed in section 7.4.2 and F_t contains the internal stresses, which are nonlinear with respect to the cardiac deformation and also comprise the second Piola-Kirchhoff stress tensor $\frac{\delta\psi^2}{\delta\epsilon}$.

Δu, the incremental displacement vector caused by the force difference $F_b - F_t$, is the only unknown of equation 7.2 when the Newmark method for temporal

integration, a numerical method used to solve the matrix equation, is used (198). By solving equation 7.2 for the nodal displacements, Δu (and therefore strains) can be estimated from the image-derived motion.

7.4.4 Further Explanation of the Hyperelastic Biomechanical Model

To provide further explanation of our method, we shall start from the first time point. In equation 7.1, as we assume no deformation at the first time point, F starts as an identity matrix and thus $J = 1$ and $\epsilon = 0$. We use these values to compute the second Piola-Kirchhoff stress tensor $\frac{\delta\psi}{\delta\epsilon}$ and elasticity tensor $\frac{\delta\psi^2}{\delta\epsilon^2}$ at the first time point. After applying the boundary conditions F_b, through equation 7.2, their values change as the body is now deformed. Their new values are obtained by solving the MCK system equation for nodal displacement and therefore we can compute a new deformation gradient tensor F. With this F, it is possible to calculate a new J and a new $\bar{\epsilon}$. These values are then used to to compute a new second Piola-Kirchhoff stress tensor $\frac{\delta\psi}{\delta\epsilon}$ and elasticity tensor$\frac{\delta\psi^2}{\delta\epsilon^2}$. With this explanation it is possible to view equation 7.1 as a function of nodal displacements Δu.

7.4.5 Strain Calculation

The displacement vectors, Δu, can be used to calculate the deformation gradient tensor, F, which is then used to calculate strain, $\in$, according to the Green-Lagrange strain tensor equation:

$$\in = \frac{1}{2}F^T F - I \tag{7.3}$$

where Δu is the displacement gradient, F is the deformation gradient tensor, and E is strain tensor. From the strain tensor, three principal strains ($\in_1 > \in_2 > \in_3$) and six cylindrical strains with respect to the LV long axis ($\in_{rr}$, $\in_{\theta\theta}$, $\in_{zz}$, $\in_{r\theta}$, $\in_{rz}$, $\in_{z\theta}$ with r, θ, and z indicating the radial, circumferential, and longitudinal directions) are computed for the whole cardiac cycle. The

corresponding zonal strains are computed as the average nodal strains in the zones. To alleviate the effects of intersubject variability for each strain type, such as $\in_{rr}$, the zonal strains are normalised by the largest zonal strain magnitude among all zones in the whole cardiac cycle of each subject (199).

7.4.6 Cardiac Perfusion Defect

Image analysis for cardiac perfusion defects, our ground truth, was performed on a dedicated Vitrea (Vital Images, Minntonka, MN, USA) workstation. Infarction leads to reduction in myocardial blood supply, and a subsequent decrease in CT attenuation of the myocardium can be observed in ischaemic areas. The correlation between hypoenhancement and infarcted regions was previously validated through animal studies with postmortem triphenyltetrazolin-chloride (TTC) staining in histology (200). TTC is a redox indicator whose presence indicates cellular respiration. Healthy viable heart muscle will stain deep red from the cardiac lactate dehydrogenase, while areas of potential infarctions will be paler. As hypoenhancement lasts for several cardiac cycles, it can be a robust feature for infarct identification. The infarcted regions were identified by experts using perfusion CT with the heart being divided into the AHA zonal nomenclature (17 zones).

7.4.7 Experimental Design and Evaluation

To evaluate the effectiveness of our method and determine which strain (i.e. $\in_{rr}$, $\in_{\theta\theta}$, $\in_{zz}$, etc.) is best for disease detection, the following steps were performed. First, receiver operating characteristic (ROC) curves were produced with the different strains. From the ROC curves we were then able to calculate "area under the ROC curve" (AUC) values and to determine the optimal threshold strain values for distinguishing disease and healthy tissue. With these optimal thresholds, Leave-One-Subject-Out (LOSO) cross validations can be used to assess performance and used to calculated true positive rate (TPR),

false positive rate (FPR), and Gwet's AC1 coefficient (AC1). Details about each of these steps are provided below.

For each subject, the maximum zonal strain magnitude in the whole cardiac cycle was selected for each zone, and the largest one among all 17 zones was used to compute the normalised zonal strains (Figure 7.3). Using the expert-identified zonal infarction as the ground truth, the overall ROC curves of all strains were computed. ROC curves are a standard method of evaluating a classifier (i.e. in this case various peak average segmental strains) and are graphical plots that illustrate the performance of a metric for discrimination at various thresholds. Each point on the ROC curve represents a sensitivity/specificity pair corresponding to a particular threshold value of the classifier. Perfect discrimination (no overlap in the two distributions) has a ROC curve that passes through the upper left corner (100% sensitivity, 100% specificity). In other words, the closer the ROC curve is to the upper left corner, the higher the overall accuracy of the test. ROC can be used to calculate the AUC, a measure of how well a parameter can distinguish between two diagnostic groups (infarcted vs. normal). The higher the AUC value, the better the classifier is able to distinguish the two diagnostic groups.

Cross validation allows for assessment of how the results of a statistical analysis will generalise to an independent data set. Given the size of our dataset, leave-one-subject-out (LOSO) cross validation was performed. Let n be the number of subjects.

In each test, the zonal features of $n - 1$ subjects are used to train the classifier, which is then used to classify the zonal infarction of the left-out subject. Although more complex machine learning algorithms can be utilized, in this preliminary study the resulting zonal strain magnitudes were used as the inputs to a threshold classifier. This is based on the fact that infarcted tissues are usually less contractile and thus have smaller strain magnitudes.

The average performance can then be obtained after n tests and can be used to compute TPR, FPR, and Gwet's AC1. For determining the agreement

between the ground truth and the classification, the Gwet's AC1 agreement coefficient can be used. Compared to other metrics of agreement such as Cohen's kappa or Scott's pi, Gwet's AC1 does not depend upon the assumption of independence between the two measurements and therefore can be used in more contexts compared to kappa or pi.

For further evaluation, student t-tests were performed between the different strain magnitudes of the 110 normal compared to the 60 infarcted zones, in order to better understand the statistical distribution.

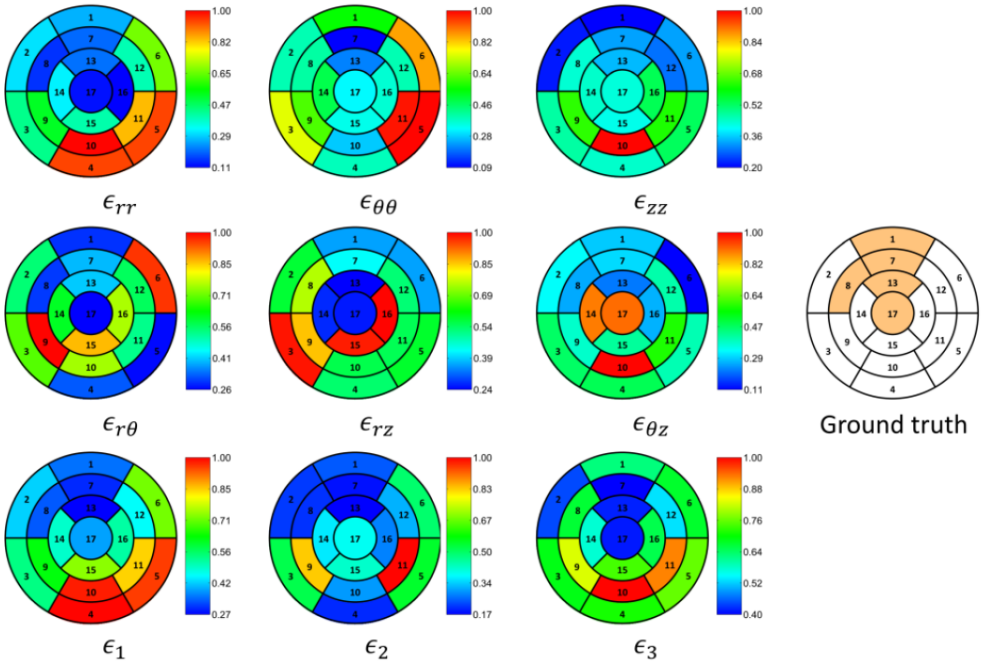

Figure 7.3: ***Normalised Zonal Strain Maps of the Same Subject from Figure 7.1.*** *Ground truth indicates infarcted zones, which were caused by left anterior descending artery blockage. Three principal strains ($\in_1 > \in_2 > \in_3$) and six cylindrical strains with respect to the LV long axis ($\in_{rr}$, $\in_{\theta\theta}$, $\in_{zz}$, $\in_{r\theta}$, $\in_{rz}$, $\in_{z\theta}$) with r, θ, and z indicating the radial, circumferential, and longitudinal directions were examined.*

7.5 Results

110 normal and 60 infarcted zones in total were identified by experts using perfusion CT with the heart divided by the AHA 17 segment zonal nomenclature.

Examining Figure 7.3, one can see that for the principal strain $\in_1$, $\in_2$, and $\in_{rr}$, there is a detectable decrease in strain (i.e. more blue) in the are of the infarction. The shear strain ($\in_{r\theta}$, $\in_{rz}$, $\in_{z\theta}$), on the other hand, showed little with the infarcted region.

7.5.1 Receiver Operating Characteristic (ROC) Curves

Figure 7.4 shows the overall ROC curves. Comparison of the AUC values shows the following results. For the normalised strain magnitudes, the radial strain ($\in_{rr}$) has the largest AUC (0.89), and first principal strain ($\in_1$) has similar performance (0.87). For the unnormalised strain magnitudes, again the radial strain performed best, while the first principal strain and circumferential strain ($\in_{\theta\theta}$) are similar.

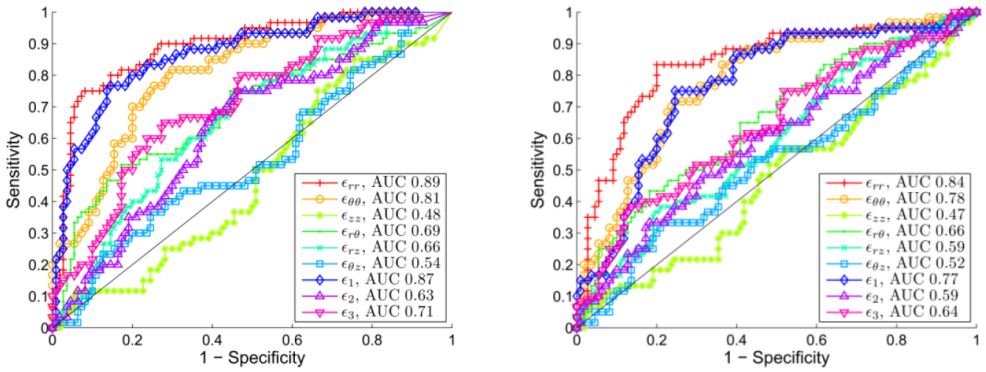

Figure 7.4: ***ROC Curves with Respect to Strain Magnitude Thresholds.*** *Left to right: normalised and unnormalised strain magnitudes. Three principal strains ($\in_1 > \in_2 > \in_3$) and six cylindrical strains with respect to the LV long axis ($\in_{rr}$, $\in_{\theta\theta}$, $\in_{zz}$, $\in_{r\theta}$, $\in_{rz}$, $\in_{z\theta}$) with r, θ, and z indicating the radial, circumferential, and longitudinal directions were examined.)*

For all strains, the normalised strains provide better performance. For strains $\in_{\theta_r}$and $\in_{zz}$, some ROC points are below the diagonal line, which means that the threshold classifier is improper for them. A possible reason is the similar statistical distribution of the strain magnitudes in the normal and infarcted zones (Table 7.1).

Table 7.1: ***Comparison of Strain Values Between Infarcted and Normal Zones.*** *110 normal and 60 infarcted zones strain value comparison.*

Normalized	ϵ_{rr}	$\epsilon_{\theta\theta}$	ϵ_{zz}	$\epsilon_{r\theta}$	ϵ_{rz}	$\epsilon_{\theta z}$	ϵ_1	ϵ_2	ϵ_3
p-value	0.00	0.00	0.81	0.00	0.00	0.45	0.00	0.00	0.00
Unnormalized	ϵ_{rr}	$\epsilon_{\theta\theta}$	ϵ_{zz}	$\epsilon_{r\theta}$	ϵ_{rz}	$\epsilon_{\theta z}$	ϵ_1	ϵ_2	ϵ_3
p-value	0.00	0.00	0.56	0.00	0.05	0.59	0.00	0.08	0.00

Table 7.2: ***Results of Leave-One-Subject-Out Cross Validations.*** *The true positive rate (TPR), fast positive rate (FPR), Gwet's AC1 coefficient (AC1), and optimal strain threshold (Threshold) are shown.*

Normalized	ϵ_{rr}	$\epsilon_{\theta\theta}$	ϵ_{zz}	$\epsilon_{r\theta}$	ϵ_{rz}	$\epsilon_{\theta z}$	ϵ_1	ϵ_2	ϵ_3
TPR	0.73±0.17	0.64±0.26	0.01±0.05	0.32±0.23	0.22±0.20	0.02±0.05	0.72±0.20	0.03±0.09	0.51±0.27
FPR	0.07±0.04	0.21±0.15	0.05±0.11	0.11±0.14	0.18±0.11	0.07±0.14	0.14±0.10	0.08±0.14	0.21±0.17
AC1	0.74±0.15	0.51±0.18	0.43±0.19	0.49±0.23	0.34±0.20	0.41±0.20	0.66±0.20	0.40±0.20	0.45±0.19
Threshold	0.28±0.01	0.46±0.03	0.15±0.05	0.27±0.02	0.28±0.06	0.13±0.07	0.41±0.00	0.19±0.08	0.65±0.01
Unnormalized	ϵ_{rr}	$\epsilon_{\theta\theta}$	ϵ_{zz}	$\epsilon_{r\theta}$	ϵ_{rz}	$\epsilon_{\theta z}$	ϵ_1	ϵ_2	ϵ_3
TPR	0.66±0.28	0.70±0.24	0.00±0.00	0.25±0.25	0.13±0.28	0.07±0.16	0.74±0.26	0.10±0.25	0.36±0.38
FPR	0.18±0.26	0.24±0.21	0.03±0.09	0.11±0.18	0.10±0.22	0.07±0.23	0.24±0.28	0.09±0.16	0.12±0.20
AC1	0.57±0.28	0.50±0.21	0.46±0.16	0.44±0.29	0.40±0.20	0.42±0.28	0.53±0.30	0.42±0.14	0.48±0.18
Threshold	0.24±0.04	0.09±0.00	0.02±0.00	0.03±0.01	0.04±0.01	0.01±0.01	0.38±0.00	0.02±0.00	0.15±0.00

7.5.2 Leave-One-Subject-Out Cross Validations

Table 7.2 shows the results of the leave-one-subject-out cross validations. Similar to the above discussion, for the normalised strain magnitudes, the radial strain gives the best performance, followed by the first principal strain. For the unnormalised strains, the performance between the radial, circumferential, and the first principal strains are similar, and they are far better than the other strains. Comparing between the normalised and unnormalised strains, we can see that for the radial strain and the first principal strain, normalisation can largely improve the true positive rate and the false positive rate. We can also see that the Gwets AC1 coefficients, which indicate the agreements between the expert identification and the strain threshold classifier, are much higher with strain normalisation.

7.6 Discussion

Must of the previous work done with CCT has been focused on globe metrics. Therefore, in terms of image processing, often the methods focus on segmentation of the chambers rather than creating regional correspondences needed for regional assessment. This work includes (201), which demonstrated that EF, EDV, ESV, and LV mass estimated with MDCT agreed and correlated well with estimated with MR (bias ± standard deviation, EF: -1.2% ± 4.6; r = 0.96, EDV: -0.35 mL ± 15.2; r = 0.97, ESV: 1.1 mL ± 8.6; r = 0.99, and LV mass: 2.5 mL ± 15.0; r = 0.96). The standard deviations noted here were significantly smaller than those noted between MR and echocardiography and between MR and SPECT. (202) demonstrated that regarding the EF, the agreement with MR was significantly superior for MSCT than for biplane cineventriculography (CVG) (± 10.2% vs. ± 16.8%; $p \leq 0.001$) and echocardiography (± 11.0% vs. ± 21.2%; $p \leq 0.001$).

Visual detection of differences in regional kinetics have been shown to be possible with CCT (203; 204; 205). (204) compared MDCT with gated SPECT and 2D echocardiography with visual assessment of regional wall motion (LVRWM) with a 3-point scale using a 17-segment model (a 3-point scale of 1=normokinesia, 2=hypokinesia, 3=akinesia or dyskinesia). They found that LVRVM agreement was 95% (κ =0.66) between gated SPECT and MDCT, and 96% (κ =0.73) between 2D echocardiography and MDCT.

Additional studies found similar agreement with LVRWM assessment correlation between the MDCT and 2-dimensional transthoracic echocardiography (TTE) (κ = 0.61) (206). A separate study with the methodology demonstrated similar agreement between two-dimensional transthoracic echocardiography (2D-TTE) and MDCT (κ = 0.70). In (204), LVRVM agreement was 95% (kappa=0.66) between gated SPECT and MDCT, and 96% (kappa=0.73) between 2D echocardiography and MDCT. (207) found similar results with a 320-detector CT and electrocardiography, with agreement for assessment of

LVRWM between 2D-echocardiography and MDCT being excellent ($\kappa = 0.76$). Additional studies were performed to compare MDCT with the current standard of MR. These studies also found similar agreements (86.7% $\kappa = 0.81$) (208), and (90% $\kappa = 0.78$) (209).

The next logical step would be quantification of these differences, which this work hopes to take steps towards addressing. Using a hyperelastic biomechanical model, regional myocardial strains can be estimated from the deformation fields computed from CT image sequences. Using a threshold classifier on the regional strain magnitudes, the overall ROC curves were computed and cross validations were performed. The results show that the normalised radial strain and the normalised first principal strain in our method had the most potential for identifying areas of disease.

There are a number of benefits to using our pipeline, which combines the use of a cardiac mechanical model with image registration. Image registration alone may face issues including the aperture problem (where there are a number of solutions that fulfil the used similarity criterion), and the problems of falling into local minima of the optimization function (i.e. cost function) (178). The use of a mechanical model can be to help formulate and regularise the problem, therefore improving the accuracy of the strain analysis (210).

An exciting aspect of this methodology is that it is potentially modality-independent and could work with any 3D dataset (it has the potential to be applied to both CMR and 3D echocardiography). In addition, the use of a personalised cardiac model allows for the possibility of integrating other clinical data including electrophysiology (211), Purkinje fibre system (212), coronary anatomy, myocardial fibrosis, etc.. In addition, there is interest in multi-scale (211) extensions of a model which can move from the cellular myofilaments and cellular ionic channels to gross contraction and electrical conduction. Considering all these possibilities will be an important step forwards.

7.6.1 Limitations

This work shows the potential of this method, but further work should be done towards improving the methods, such as incorporating automatic segmentation of the heart chambers, and creating a model for all chambers of the heart. While the LV is the main pumping chamber of the heart, the function of all four chambers is important and is implicated in disease. This will allow for complete analysis of cardiac function. It is our belief that the more automatic a method is, with less user input, the easier it will be for this metric to be incorporated into clinical practice.

In our model, we assumed transversely isotropic tissues to reduce the number of material constants needed, however a more accurate representation would include the hetero-cellular nature of heart muscle (213) (i.e. orthrotropic with respect to mutually orthogonal fibre-sheet (214)).

7.6.2 Conclusion

In this chapter, we pursued a 3D deformable biomechanical model that accounts for the hyperelastic properties of the heart. Radial and ϵ_1 strain were the most accurate single strain parameter in predicting diseased areas of the heart.

"Continuous computed tomographic (CT) scanning of organ volumes during a single breath hold was studied. The authors modified the table feed mechanism of a continuously rotating CT scanner to allow patient transport at low, but accurately controlled, speeds (0.1-11.0 mm/sec) during continuous 1-second scanning. An algorithm was designed to reconstruct artifact-free images for arbitrary table positions from the helical data by interpolating between adjacent scans". Conducted first clinical examine with spiral-CT.

—Kachelriess M. Kalender, 1989 (215)

8 Conclusion

Contents

8.1 Introduction

The current literature, mainly with the modalities of echocardiology and CMR, suggests that cardiac strain analysis can potentially play an important clinical role in assessment of myocardial mechanics, cardiomyopathies, ischaemic heart disease, guidance of CRT, LV diastolic dysfunction and the detecting of sub-clinical myocardial dysfunction in patients with valvular disease or who undergo cardiotoxic chemotherapy (74; 89). Currently, cardiac strain analysis

is not well examined with CT. The thesis took steps to address this by examining the feasibility and utility of strain analysis with CT, improving the CT acquisition protocol, better characterisation of myocardium in CT images, and development of analysis pipeline for 3D strain analysis tailored for CT images. Below are summarises of each of these steps.

8.2 Feasibility and Utility of Strain Analysis in CT

In **Chapter 4**, we evaluated the feasibility of using strain analysis by MDCT to detect subtle disease in cases of normal EF. Our research found that myocardial strain analysis of cine MDCT images identifies differences between control and cardiomyopathy groups ($p = 0.05$ for comparison to both tagged CMR and histologic findings) in a porcine model. Also, our results indicated that MDCT regional strain analysis has the potential to detect abnormalities in myocardial function in cardiomyopathy in a manner similar to standard of CMR strain analysis. *Putting this into the context of patient care, our work suggest that myocardial strain analysis by MDCT has the potential to identify and quantify regional wall motion abnormalities and should be considered a potential imaging modality for such analysis.*

8.3 Improving CT Imaging Acquisition for Regional Cardiac Functional Analysis

In **Chapter 5**, we developed an image acquisition protocol with low radiation dose. By using a 320-detector row CT scanner with a 16-cm wide volume coverage and a gantry rotation time of 275 msec, we were able to acquire one mSv range cine CT images with high (<50 millisecond) temporal resolution. In our study, median radiation dose was 1.27 mSv; the radiation dose was less than 1 mSv in 8% of the CT examines (4 of 52 patients), less than 1.5 mSv in 84.6% (44 of 52 patients), and less than 2 mSv in 96.2% (50 of 52

patients). Overall, high (<50 millisecond) temporal resolution imaging of the cardiac myocardium is feasible at low (one mSv range) radiation doses. This is a dramatic improvement from the previous target of 6.32 mSv (4.69-8.89 mSv) for cine CT. *In the context of patient care, with the feasibility of high temporal resolution, low dose cine MDCT, comprehensive evaluation of cardiac function and coronary anatomy can be performed with the potential for routine cardiovascular health monitoring.*

8.4 Better Characterisation of Cardiac Tissue in CCT as Potential Marker in Functional CT Analysis

In **Chapter 6**, we developed a method to better characterize myocardial tissue deformation in 2D+t images. We specifically evaluated the potential use of feature-based attribute vectors to better characterize pixels for image registration in CCT. We found that by developing a suitable attribute vector as a morphological fingerprint for distinct points in the cardiac image sequence, we achieved a more accurate cardiac registration and subsequently derived more reliable motion estimations than registration based on either intensity or FA alone. *Putting this research into a larger context, there is potential to better characterise the homogeneous appears of myocardium in CT and the use of feature-based attribute vectors should be considered a potential route for improving functional CT analysis.*

8.5 Development and Evaluation of 3D Pipeline for Functional CT Analysis

Finally, in **Chapter 7**, we focus on the development of an image processing pipeline enabling the use of cardiac modelling towards 3D+t CCT functional analysis. We specifically examined a pipeline that incorporates a deformable 3D biomechanical model that accounts for the hyperelastic properties of the

heart. With this method, we showed that regional myocardial strains can be calculated in 3D+t space and can detect areas of infarction. When such a process is used, radial and principal ϵ_1 strain were the most accurate strain parameters in predicting diseased areas of the heart. *Putting this research into a greater context, full 3D modelling and analysis of cardiac function is feasible with CT and given the innate 3D nature of CCT will be pursued.*

8.6 Thesis Conclusions

As methods for function analysis are developed for CCT, the possibility emerges of CCT becoming a "one-stop shop" for adult cardiovascular imaging, providing information on anatomy, function, perfusion and viability (216). Clinical research has shown the potential utility of strain analysis from CCT, and has optimized the clinical protocols for patient use. Technical research has shown that a tailored image processing pipeline can be developed to better enable strain analysis with MDCT. While we have taken steps towards this possibility in the thesis, continued efforts on both the clinical and technical fronts will be necessary for CT regional functional analysis to become a reality for routine patient care.

"Specified regions of the myocardium can be labeled in magnetic resonance (MR) imaging to serve as markers during contraction. The technique is based on locally perturbing the magnetization of the myocardium with selective radio-frequency (RF) saturation of multiple, thin tag planes during diastole followed by conventional, orthogonal-plane imaging during systole." First tagged CMR examination.

—Elias Zerhouni, 1988 (7; 42)

9 Future Directions

Contents

9.1 Introduction

We anticipate a bright future for the field of cardiac imaging, especially with interdisciplinary and global research efforts. In this chapter, we provide a short summary of the current clinical situation of cardiac deformation analysis, a prediction of two key target areas for research in the field of regional cardiac analysis, and an overall prediction for the field the next five years (to 2020 and beyond).

9.2 Current Clinical Situation of Clinical Strain Analysis

Regional wall motion is useful for physicians as a quantitative surrogate for regional function. Abnormal strain can result from a variety of disorders including myocardial infarction, cardiomyopathies and arrhythmias. Tagged MR is typically considered the standard of reference for strain imaging, however its use is primarily confined to a limited number of academic centres. Echocardiography strain analysis is widely available for clinical applications. Reproducibility and differences in strain assessment between vendors will need to be addressed to help facilitate its use in clinical practice. CCT is the newest imaging modality that is potentially capable of strain analysis. The focus with CCT has been in imaging coronary artery anatomy. There is now an increased interest in investigating other potential uses of CCT due to the widespread availability of this modality.

9.3 Key Target Areas for the Field of Regional Strain Analysis

9.3.1 Standardisation and Transparency of the Cardiac Strain Field

The field of strain imaging currently suffers from a lack of systematic standardisation between vendors, and modalities. This lack of standard makes it difficult to apply results from the literature to clinical practice. Areas of variability include differences in the terminology describing myocardial mechanics, the type of stored data which is used (i.e. standard DICOM vs proprietary formats), the modality and physical means of measuring strain analysis (TDI, tagged MR, feature-tracking, etc.), proprietary algorithms of calculating strain, and non-standard cardiac segmentation (1).

To address these issues, consensus statements such as those issued by the EACVI, ASE and industry leaders (1) will be implemented and expanded upon.

Similar efforts of standardisation have been taking for CMR by the SCMR Board of Trustees Task Force (114) and by teams of scientist (217). The SCMR recognises the evolving nature of the field of cardiac strain and have postponed issuing a consensus document to a later date (114).

As stated previously, the use of CCT in strain imaging is in its incipience and the feasibility of such studies are still being established. As further work is done with CCT strain imaging, there will be a need to develop guidelines similar to those of echocardiography and CMR.

While efforts are being made to standardise strain imaging within each modality, the next logical and necessary step will be standardisation across modalities. It is our belief that in order to move the field forward, a cross modality consensus statement needs and will be created. Research has been done to establish agreement between modalities (218). However continued work should be done to establish guidelines for all imaging modalities to follow.

In addition, current efforts of standardisation have focused on 2D imaging. As 3D functional analysis develops (16; 219), standardization of terminology and methodology will need to be performed. 3D analysis is inherently different, potentially factoring in through-plane motion. Accounting for these differences between 2D and 3D analysis, especially when it comes to clinical literature, will be important when moving forward.

Another concern which needs to be addressed is the inter-vendor consistency and reproducibility of strain measurements. Research in this area shows that strain values are highly vendor-dependent and that continued work is necessary (220; 221; 222). For instance, (221) showed that variation in strain can occur even when two different software packages are used to analyse the same data set. This variability is beyond the intrinsic variability of each software package, suggesting that the variability is due to the specific details of the analysis technique (221). Continued efforts towards increased transparency of analysis methods and/or standardisation across vendors will be important to have impact on the care of patients.

9.3.2 Towards User-Independent Analysis

Echoing (223), continued efforts will be made community to automate the analysis and acquisition for functional analysis. A key concern of clinical strain analysis is the time consuming nature of semi-automatic tracking. In addition, this adds a level of training necessary for accurate analysis. In order to avoid these issues, integration of a completely automatic segmentation of the myocardial wall be pursued. In addition, standardised measurement of tracking quality will be implemented to help the image processing pipeline.

9.4 View for 2020 and Beyond

In terms of regional wall motion analysis, further research will continue to be done with all three modalities. As discovered in (48), techniques can take a surprising amount of time to develop from the initial idea until implementation in clinical patient care, and we expect a similar situation in this field. While tagged MR is considered the standard of comparison in regional wall motion, it has not been translated out of academic centres to clinical practice due to higher cost and long processing times. Continued research needs to be done to address these issues. For both CMR and echocardiography, issues with variability will continue to be addressed including accounting for differences between vendor platforms. Effort towards user-independent regional strain analysis will also be taken.

Regional wall motion analysis with CCT has only recently been investigated and developed. While not currently a standard method for obtaining regional strain, the use of CCT will continue to evolve both clinically and technically. In our opinion the use of CMR, CCT, and echocardiography should not be considered to be in direct competition. We would like to emphasise that these methods can complement one another depending on the clinical situation, and will complement each other as these methods are investigated further. Standardisation and automaticity efforts will occur across modalities.

With the progress made with CCT methods in terms of resolution and reduction of radiation dose, it appears highly likely that the number of CCT studies performed will continue to increase, as will the demand for improved image analysis capabilities. Cardiac regional wall deformation analysis will be a key factor in improving CCT capabilities. In addition, we expect other measures including torsion and strain rate to be investigated. We expect to see an increase in CCT use both for coronary and non-coronary applications such as myocardial function assessment. As all these efforts are made, the reality of regional functional analysis with CCT will be realised towards improving patient care.

Appendices

"A technique has been developed for producing images of the velocity of tissue motion within the myocardium. It has been demonstrated that Colour Flow Doppler imagers can be operated to depict the velocities within the myocardium rather than moving blood in the cardiac chambers". First Tissue Doppler Imaging.

—McDicken, 1992 (224)

A Computed Tomography

A.1 Introduction

CT, previously referred to as computerised axial tomography (CAT), is a diagnostic imaging procedure that uses X-rays to create cross-sectional slices, and more recently volumes, of the body. Additional information about CT can be found at (225), with history of CCT being found at (226).

CT is based on the principle that the density of the tissue that an X-ray beam passes through can be measured from the calculation of the linear attenuation coefficient, μ[1]. We will now discuss the physical processes that lead to attenuation.

A.2 Mechanisms Causing Attenuation of an Incident X-Ray Beam

Attenuation of X-rays can occur through three processes: photoelectric interaction, Compton scattering, and pair production. These phenomena are

[1] Attenuation is defined as the reduction in intensity of an X-ray beam as it passes through a material.

collectively represented by a single attenuation coefficient μ. We shall now discuss each of these processes.

Photoelectric interaction, or photoelectric absorption (PEA), occurs when an X-ray is absorbed by an atom, resulting in its ionisation (i.e. the release of electrons from the outer shell of the atom). This ionised atom returns to the neutral (non-ionised) state by emitting an X-ray photon, which generally does not contribute to the X-ray image.

Compton scattering occurs when the incident X-ray photon is deflected rather than absorbed by the interaction with an electron in the material. The electron gains energy and is ejected from its electron orbital. The incident (original) photon loses energy (i.e. develops a longer wavelength), creating a low-energy scattered X-ray photon which continues travelling in an alternative path.

Pair production occurs when the photon interacts with the nucleus of an atom, instead of the electron. In this case, the photon gives its energy to the nucleus leading to the creation of a pair of positively and negatively charged electrons (i.e. an electron and a positron). These two particles usually annihilate each other. This process often requires higher energy levels (greater than 1.02 Megaelectron-volts (MeV)) and occurs more often when the the high energy photon passes through a high atomic number material.

There are other interacting phenomena, including Thomson scattering (i.e. Rayleigh, coherent, or classical scattering), and photodisintegration. Thomson scattering occurs when the X-ray photon interacts with the entire atom so that the photon is scattered without any change in internal energy of the atom, nor production of a new X-ray photon. Photodisintegration occurs when the X-ray photon is captured by the nucleus of the atom, with the ejection of a particle from the nucleus. The contribution of these processes to μ is negligible in the context of clinical imaging.

In general, contrast agents have higher μ, but these differences are much more apparent at low energies. This explains why lowering kV improves image

contrast.

A.3 K-Edge

Photoelectric interaction and Compton scattering are the main phenomena that lead to attenuation in diagnostic imaging. The probability of either of these phenomena occurring decreases as the energy of the photon increases. However, the decrease in the photoelectric effect is more rapid than the decrease in the Compton scattering.

With the photoelectric effect, it is important to note that there is a periodic increase in attenuation. This increase corresponds to the orbital shells in which electrons are bound. The highest energy where the attenuation jumps is known as the K-edge, which corresponds to the binding energy of the innermost and tightest bound electrons (i.e. K-shell electrons). There are other absorption edges at lower energies, corresponding to more loosely bound electrons in the outer shell. The K-shell effect is particularly important when considering contrast media.

A.4 Hounsfield Units

As previously discussed, CT measures spatial distributions of the linear attenuation coefficients $\mu(x, y)$. However, $\mu(x, y)$ is strongly dependent on the spectral energy used and therefore lacks physical meaning on its own. In order to decouple $u(x, y)$ from the spectral energy, the computed attenuation coefficients are adjusted to the attenuation of water to yield a quantity called Hounsfield unit, (HU). The calculation is performed as follows:

$$CTvalue = \frac{\mu_m - \mu_{water}}{\mu_{water}} * 1000HU \tag{A.1}$$

where μ_m is the attenuation coefficient for an arbitrary material being imaged, and μ_{water} is the attenuation coefficient of water. The attenuation coefficient of water is 0 HU by definition. Since μ_{air} is approximately 0, air has a CT value

of -1000 HU. These two values are independent of the energy of the X-rays and therefore are good fixed points for CT values.

Examining this scale further, low density tissues (like lung tissue and fat tissue) exhibit negative CT values. Most body tissues will exhibit positive CT values. Bones and calcifications, of high density, will typically exhibit even higher CT values of approximately 2000 HU. CT values of bone or contrast media are more strongly dependent on the energy of the X-ray. Therefore, with increase in voltage settings, these materials have a particularly noticeable change in μ.

While there is a lower limit of -1000 HU, there is no upper limit on the Hounsfield scale. For medical imaging scanners the range is typically from -1024 HU to +3071 HU (with a total of 4096 values). Therefore, with, 4096 different grey values $4096 = 2^{12}$, 12 bits per pixel (bbp) are required. This calculation in explained in section **??**.

A.4.1 Grey Scale

Grey-scale resolution refers to the change in the shades or levels of grey in an image, and is dependent on the bits of data per pixel (bpp). It is calculated via the following equation:

$$L = 2^k \tag{A.2}$$

where L refers to the number of grey levels (i.e. the shades of grey), and k refers to bpp or bits per pixel. This equations results from the fact that image pixels are stored in binary quantized form.

For reference, the typical computer screen display is 8 bpp, and therefore allows 256 different intensities (i.e., shades of grey) to be recorded. This is already significantly higher than the 60-80 grey levels distinguishable by the naked human eye. In order to minimise numerical round-off errors in computing, medical imaging is often done in 10 to 12 bpp.

A.4.2 Windowing

As mentioned, medical CT scanners have the CT value range from -1024 HU to +3071, HU with 4096 grey levels; far beyond displayable ranges of normal computer monitors, films, or visible by the human eye. The complete grey scale is therefore often assigned the CT values for the window of interest. This process is called windowing. A few typical window ranges include: -1450 HU to +250 HU for lung imaging, -250 HU to +150 HU for mediastinal imaging, and -250 HU to +2250 HU for bone imaging.

"This paper introduces a two-dimensional (2-D) generalization of the analytic signal. This novel approach is based on the Riesz transform, which is used instead of the Hilbert transform. The combination of a 2-D signal with the Riesz transformed one yields a sophisticated 2-D analytic signal: the monogenic signal." Developed the monogenic signal.

—Michael Felsberg, 2001 (173)

B
Normal Strain Values

B.1 Introduction

The routine application of myocardial strain in clinical practice requires the definition of a normal range. However, a recurring issue with the use of cardiac strain is the lack of standardised normal values. In this Appendix, we will review the current literature on standardisation of normal cardiac strain values. This appendix is broken into literature from echocardiography and CMR, as there is currently no literature on standard strain values from CCT. We shall discuss the research development towards obtaining normal strain values in echocardiography. With tagged MR being consider the reference standard, we will discuss the process of study selection and the presentation of the data.

B.2 Echocardiography

B.2.1 Establishing Normal Strain Values

A number of attempts at establishing normal strain values have been performed in echocardiography. Dalen *et al* (227; 228) conducted a large scale study, analysing 1266 healthy individuals to create cardiac strain reference values for

everyday clinical settings based on echocardiography (see Table B.1 and Table B.2). In this study, they divided the heart into six segments, as represented by Figure 2.2. Longitudinal strain values decrease with age. With this knowledge that strain varies with age, reference values for children for strain and strain rate have also been reported in (229).

A recent meta-analysis, which identified 2597 subjects from 24 studies, attempted to re-establish normal strain values obtained from echocardiography (230). This study found that global longitudinal strain (GLS) and global circumferential strain (GCS) showed the narrowest confidence intervals. However, there was significant inter-study heterogeneity and inconsistency (230). To address the issues of the significant differences between studies, (231) performed a multi-centre trial, which established structural guidelines in terms of modality, specific scanner, and analysis method. They found that it is possible to produce consistent results when these factors are controlled for. These consistent results showed that there are differences in normal strain between genders, age groups, and different segments of the heart. This functional non-uniformity indicates that when considering cardiac strain, segment-specific normal ranges must be considered. However, this still does not address the issues of different vendors, technical methodology and modalities. This is an important consideration as technical is continuously improving and changing, and a metric to be used clinical would ideally be independent of such changes.

B.3 CMR

CMR is the standard reference modality for strain measurement due to its accuracy and reproducibility (96). However, even though this modality and imaging protocol is considered the standard, work continues to be done in order to establish normal values.

In (232), in order to develop a better sense of normal values, researchers synthesised the results of a number of articles (with sample sizes ranging from

	Inferoseptum	Anterolateral	Inferior	Anterior	Inferolateral	Anteroseptum	Mean
Apical	17.8 (3.9)	14.6 (4.0)	17.6 (4.3)	14.3 (4.7)	15.5 (4.3)	16.1 (3.9)	16.4 (4.3)[2,3]
Mid-ventricle	17.9 (3.5)	16.4 (3.5)	17.3 (3.7)	17.4 (3.6)	17.0 (3.8)	17.1 (3.5)	17.3 (3.6)[1,3]
Basal	14.6 (3.9)	19.2 (3.7)	15.9 (3.9)	17.7 (4.1)	17.0 (4.0)	13.9 (4.5)	16.2 (4.3)[1,2]
Mean	16.8 (4.0)[8,9]	16.6 (4.1)[6,9]	17.0 (4.0)[5,8,9]	16.8 (4.3)[9]	16.5 (4.1)[4,6,9]	16.0 (4.1)[4 *to* 8]	16.7 (4.1)

Table B.1: ***Segmental Longitudinal End-Systolic Strain (Ses).*** *Ses (%), mean (SD), Footnotes refer to significant difference between the respective level/wall of the left ventricle (LV) and [1] apical, [2] mid-ventricular, and [3] basal level of LV and [4] inferoseptum, [5] anterolateral, [6] inferior, [7] anterior, [8] inferolateral, and [9] anteroseptal myocardial wall. Level of significance $P < 0.05$ [one-way ANOVA (post hoc Bonferroni)].*

	$Female^1$	$Male^1$
<40 $years^2$ (208 women; 126 men)	17.9 (2.1)	16.8 (2.0)
40 to 60 $years^2$ (336 women; 327 men)	17.6 (2.1)	15.8 (2.2)
>60 $years$ (119 women; 150 men)	15.9 (2.4)	15.4 (2.4)
$Mean^3$	17.4 (2.3)	15.9 (2.3)

Table B.2: ***Global Longitudinal Peak End-Systolic Strain Divided into Age Group and Gender.*** *Mean (SD). Global longitudinal peak end-systolic strain was obtained from a 16-segment model of left ventricle (LV).* [1] *P <0.0001 for significance of difference between youngest and oldest age group for both deformation indices and both genders.* [2] *P ≤ 0.01 for significance of difference between genders in the two youngest age groups. There was no significant difference between genders in the oldest age group.* [3] *Overall very highly significant difference (P <0.0001) for deformation indices between genders.*

10-87 healthy individuals), producing normal radial, circumferential and longitudinal strain values. In this study the researchers divided the heart into three slices (apical, middle, and basal) and four segments (septal, anterior, lateral and inferior). We provide here an extension of the consolidation work done by (232) in Table B.3, updating it with more recent studies.

The magnitude of radial strain values was greater than that of longitudinal and circumferential strain. The disparity in the quantification results of the different CMR studies can be explained by population inhomogeneity, variation in slice levels, use of different motion estimation, and use of different quantification methods.

B.3.1 Study Inclusion Criteria

Multiple studies have presented cohorts of normal individuals for determining normal dimensions of the LV. For the purpose of this review, only cohorts of 30 or more normal subjects using SPAMM tagging have been included. Feature tracking methods of SSFP images have been examined (233; 234), but as they

are currently not considered the reference standard, they were not included in our table. Inclusion criteria included a full description of the subject cohort (including the analysis methods used), age and gender of subjects. Table B.3 represents a summary of publications reporting normal values for midwall strain that fit the criteria (188; 235; 236).

With tagged MR, normal midwall circumferential (47; 235), radial (47; 188; 237; 238; 239; 240; 241) and longitudinal (188; 235; 237; 242) strain values are more comparable between studies. This is thought to be due to the higher tag density in these directions. Currently, with tagged MR there is more uncertainty with normal strain values in the radial direction (188; 236; 237; 238; 242; 243). It has been noted that the greater variability between different studies is in part due to the lower tag density in the radial direction (188).

B.3.2 Influencing Factors

Imaging modality and image analysis methodology can play a role in the specific cardiac strain values produced (37; 43; 243). With our current standard of tagged MR, it has been noted that age is associated with a decrease in peak circumferential or longitudinal shortening (244; 245). In tagged MR studies, gender also affects normal values. Cardiac strain in females has been noted to be higher than in males (233; 238).

B.3.3 Image Evaluation

Consistent manual tracing of the endo- and epi-cardial contours is necessary to reproduce strain results. With tagged MR, midwall strain is preferred to epi- and endo-cardial strain to maximise the amount of tagging data available for strain calculations (96; 188). With HARP analysis such as that used in the MESA trial (116), careful selection of the first harmonic is necessary.

Author	n	Age (yrs)	Acquis. method	Estimation method	Tagged resol.	FS (T)	base	mid	ap	sept	ant	lat	inf
Circumferential Strain													
Moore (2000) (188)	31	37 ± 11	SPAMM	FindTags	6mm	1.5	-0.19 ± 0.04	-0.19 ± 0.05	-0.22 ± 0.05	-0.17 ± 0.03	-0.22 ± 0.05	-0.22 ± 0.04	-0.18 ± 0.05
Cupps (2010) (235)	50	32.8 ± 10.6	SPAMM	finite element model	7mm	1.5	-0.19 ± 0.04	-0.21 ± 0.04	-0.20 ± 0.04	-0.18 ± 0.03	-0.20 ± 0.04	-0.23 ± 0.04	-0.19 ± 0.04
Del-Canto (2013) (236)	36	58.8 ± 11.6	SPAMM	SinMod	7mm	1.5	-0.17 ± 0.03	-0.20 ± 0.03	-0.20 ± 0.03	0.16 ± 0.04	0.20 ± 0.04	0.22 ± 0.04	-0.18 ± 0.04
Venkatesh (2014) (47)	129	58.8 ± 9.3	SPAMM	HARP	7mm	1.5	-0.15 ± 0.03	-0.18 ± 0.02	-0.18 ± 0.02	-0.17 ± 0.04	-0.19 ± 0.04	-0.20 ± 0.04	-0.15 ± 0.05
Longitudinal Strain													
Moore (2000) (188)	31	37 ± 11	SPAMM	FindTags	6mm	1.5	-0.15 ± 0.03	-0.15 ± 0.03	-0.19 ± 0.04	-0.16 ± 0.04	-0.16 ± 0.04	-0.16 ± 0.04	-0.16 ± 0.04
Cupps (2010) (235)	50	32.8 ± 10.6	SPAMM	finite element model	7mm	1.5	-0.13 ± 0.04	-0.15 ± 0.03	-0.18 ± 0.05	-0.16 ± 0.04	0.15 ± 0.04	-0.15 ± 0.04	-0.15 ± 0.05
Radial Strain													
Moore (2000) (188)	31	37 ± 11	SPAMM	FindTags	6mm	1.5	0.45 ± 0.26	0.42 ± 0.26	0.48 ± 0.33	0.41 ± 0.19	0.54 ± 0.28	0.46 ± 0.23	0.38 ± 0.38
Del-Canto (2013) (236)	36	58.8 ± 11.6	SPAMM	SinMod	7mm	1.5	0.13 ± 0.04	0.09 ± 0.04	0.12 ± 0.04	0.09 ± 0.05	0.10 ± 0.05	0.12 ± 0.07	0.14 ± 0.07
Venkatesh (2014) (47)	129	58.8 ± 9.3	SPAMM	HARP	7mm	1.5	0.27 ± 0.06	0.25 ± 0.05	0.23 ± 0.07	0.25 ± 0.14	0.24 ± 0.09	0.23 ± 0.10	0.26 ± 0.10

Table B.3: ***Normal Values According to Previous Tagged CMR Publications.*** *%; mean ± SD. yrs = years; Acquis. = Acquisition; resol. = resolution; FS = field strength; T = Tesla; SPAMM = spatial modulation of the magnetisation; mid = mid-cavity; ap = apical level; sept = septal; ant = anterior; lat = lateral; inf = inferior*

"We sought to assess the feasibility of 2-dimensional strain, a novel software for real-time quantitative echocardiographic assessment of myocardial function". First speckle tracking examination of strain with echocardiography.

—Marina Leitman, 2004 (54)

C Radiation

C.1 Introduction

Radiation exposure is the primary limitation in clinical CT imaging (246). In this section we provide an introduction to this topic in order to develop a better understanding of what it means to be exposed to radiation. Specifically we cover the following topics: definition of radiation, X-rays, clinical measurement of radiation, standard levels of radiation exposure, and finally the biological effects of radiation.

C.2 Radiation Introduction

Radiation is a general term that refers to any sort of energy that can travel through space either as a wave or a high speed particle. Radiation comes in two different forms, non-ionising radiation and ionising radiation, which together forms the electromagnetic spectrum. Examples of non-ionising radiation include radiowaves, microwaves, infrared, and visible light. Ionising radiation includes ultraviolet (used in tanning booths), X-rays, alpha rays, and gamma

rays. When radiation is discussed in medical imaging, one typically refers to ionising radiation, and more specifically X-rays.

C.3 X-Rays for Medical Imaging

X-rays are a type of ionising radiation that possess short enough wavelengths to allows passage through solid matter. It is this property that makes X-rays useful for medical imaging. X-rays are produced when an electron release some of its energy to either the nucleus or an orbital electron. This occurs two main mechanisms: the Bremsstrahlung process and the K-shell emission process.

During the Bremsstrahlung process, a high velocity free electron are slowed down as it interact with a target material, often composed of atoms with a high atomic number. The slowing of electrons leads to release of electromagnetic energy in the form of X-rays.

During the K-shell emission process, a high-velocity free electron knock out an electron from the inner orbital (K-shell) of the target atoms. This causes higher energy electrons from the target atom's outer orbits to descend to fill in the space created by the loss of inner k-shell electrons. This descent releases electromagnetic energy in the form of X-rays.

C.4 X-Ray Tubes

In both cases described above, high-velocity free electrons are shot at a target material such as Tungsten, which has a high atomic number (for Tungsten, n=74). In medical imaging, this process is occurs within a vacuum X-ray tube, in which electrons are accelerated from the cathode to anode across a potential difference.

In CT imaging, the anode is often a rotating anode disk, which increases the area heated by the beam and therefore helps to prevent overheating. The minimum voltage to produce X-rays in a vacuum tube is approximately 20 kV. The typical range used in clinical practice for CT is from 80-140 kV.

C.5 Measurements of Radiation

Radiation dose in medical imaging is often expressed as either absorbed dose or biologically equivalent dose. Absorbed dose is a measurement of the radiation energy absorbed by a specific object or tissue. The Systeme International d'Unites (SI) units for absorbed dose is the Gray, which equals 1 joule of ionising radiation absorbed by 1 kilogram of matter (i.e. $1Gy = 1\frac{J}{kg}$). In the United States, the absorbed dose is often reported as rads. The conversion between the units can be seen in Table C.1. However, it is important to remember that not all ionising radiation has the same effect on human tissue. For example, alpha particles, which are a different type of ionising radiation, are about 20 times more likely to lead to cellular damage than X-rays for an equivalent absorbed dose. To account for this, radiation may be measured in "biological equivalents".

Biologically equivalent dose is determined by taking the absorbed dose and multiplying it by a relative harm factor for that type of radiation. Sieverts (Sv) are the SI unit of measurement for biologically effective dose; in the United States the traditional unit is rems. Table C.1 below shows how to convert between rems and sieverts.

Radiation Measurement	SI unit	Traditional unit	Equivalency
Absorbed dose	Gray (Gy)	Rad	1 Gray = 100 Rad
Biologically effective dose	Sievert (Sv)	Rem	1 Sievert = 100 Rems

Table C.1: ***Radiation Dose Units.*** *Showing the conversion factors between SI and traditional units of both absorbed and biologically effective doses.*

C.6 Average Radiation Exposure

Radiation exposure is a normal occurrence; everyone on earth having a baseline level of radiation exposure of approximately 3 mSv per year. Exposure varies by geographic location, air travel, occupation, etc. The International Commission

on Radiological Protection (ICRP) and Enviromental Protection Agency (EPA) recommend limiting artificial irradiation. For occupational exposure, the limit is 50 mSv in a single year with a maximum of 100 mSv in a consecutive five-year period, and for the public an average of one mSv (0.001 Sv) of effective dose per year, not including medical and occupational exposures (3).

C.7 Biological Effects of Radiation

The energy content of radiation is directly related to its ability to harm. This process can lead to serious damage via a number of mechanisms, including the production of free radicals (molecules with an unpaired electron). Free radicals are capable of breaking important chemical bonds found in various macromolecules such as proteins and DNA, and creating harmful chemical bonds that interfere with normal functions.

The biological effects of radiation can be broken down into stochastic and deterministic effects. Stochastic effects (i.e. cancer inducting and DNA damaging effects) are inherently based on probability. Currently, there is no consensus on the specific radiation dose leading to the stochastic effects (247), with large epidemiological studies (248) continuously being performed to examine this effect. These sorts of studies led to the conservative limits of 50 mSv in a single year, with a maximum of 100 mSv in a consecutive five-year period (3).

Deterministic effects (i.e. acute tissue effect) are effects that are considered inevitable in all individuals who received the same high dose. Conservative estimates have been established relating radiation dose to health effects. Table C.2, provided by the United States' Environmental Protection Agency, shows estimated cumulative exposure, measured in mSv, necessary to lead to specific deterministic physiological effects (4).

Exposure(mSv)	Health Effect	Time to Onset
50-100	Dhanges in blood chemistry	
500	Nausea	Hours
550	Natigue	
700	Vomiting	
750	Hair loss	2-3 weeks
900	Diarrhea	
1000	Hemorrhage	
4000	Possible Death	Within 2 months
10,000	Destruction of intestinal lining	
	Internal bleeding	
	Death	1-2 weeks
20,000	Damage to central nervous system	
	Loss of consciousness	Minutes
	Death	Hours to days

Table C.2: ***Deterministic Health Effect of Radiation.*** *Note that the ICRP guideline of 50 mSv stops before any of these symptoms occur. The "Time to Onset" provided refers to the situation where no treatment is given (3; 4).*

C.8 Radiation Absorbed Dose in Computed Tomography

$CTDI_{vol}$, Volume Computed Tomography Dose Index, is a metric reported by manufacturers of CT scanners that provides information regarding the radiation dose of either a 16 cm (for head examination) or 32 cm (for body examinations) diameter acrylic phantom (155). It is considered to be the international standardised parameter to measure CT scanner radiation output, and has units of mGy. However, no information about patient size is included in $CTDI_{vol}$, and it is therefore not representative of patient dose.

The dose length product (DLP) is the $CTDI_{vol}$ multiplied by the scan length in centimetres, and is measured in mGy.cm. DLP is used to calculate effective dose by a conversion factor of 0.014 $\frac{mSv}{mGy.cm}$ for the chest, according to standard methodology outlined in the most recent guidelines for chest scans (146; 156). This conversion factor accounts for the exposed body region (i.e. abdomen vs head), but not the patient's age, sex or size.

C.9 Size-Specific Dose Estimate

A noted issue with $CTDI_{vol}$ and DLP is that for a small or large patient, at a given scanner setting, the value provided by the scanner is the same. The AAPM report 204 (157) describes a method to account for patient size using a metric called size specific dose estimate (SSDE). These patient size metrics are the anterior-posterior (AP) width, lateral width, and combination of AP and lateral measurements. Subsequent studies suggest using a combination of AP and lateral measurements whenever possible for the most accurate results (158). $SSDE$ is calculated as,

$$SSDE = f_{size} \cdot CTDI_{vol} \tag{C.1}$$

where $SSDE$ is size specific dose estimate, f_{size} is tabulated size-dependent conversion factors provided in (157), and $CTDI_{vol}$ is Volume Computed Tomography Dose Index.

It is important to know that $SSDE$ is still not the exact patient dose as other factors including scan length and tissue composition may differ from the assumptions used in calculating $SSDE$. This leads to reporting of all the following metrics: $CTDI_{vol}$, DLP, effective dose and $SSDE$.

References

[1] J.-U. Voigt, G. Pedrizzetti, P. Lysyansky, T. H. Marwick, H. Houle, R. Baumann, S. Pedri, Y. Ito, Y. Abe, S. Metz, J. H. Song, J. Hamilton, P. P. Sengupta, T. J. Kolias, J. d'Hooge, G. P. Aurigemma, J. D. Thomas, and L. P. Badano, "Definitions for a common standard for 2d speckle tracking echocardiography: consensus document of the EACVI/ASE/Industry Task Force to standardize deformation imaging," *European Heart Journal - Cardiovascular Imaging*, p. jeu184, Dec. 2014. Recognizing the critical need for standardization in strain imaging, in 2010, the European Association of Echocardiography (now the European Association of Cardiovascular Imaging, EACVI) and the American Society of Echocardiography (ASE) invited technical representatives from all interested vendors to participate in a concerted effort to reduce intervendor variability of strain measurement. As an initial product of the work of the EACVI/ASE/Industry initiative to standardize deformation imaging, we prepared this technical document which is intended to provide definitions, names, abbreviations, formulas, and procedures for calculation of physical quantities derived from speckle tracking echocardiography and thus create a common standard.

[2] T. P. Abraham, V. L. Dimaano, and H.-Y. Liang, "Role of Tissue Doppler and Strain Echocardiography in Current Clinical Practice," *Circulation*, vol. 116, pp. 2597–2609, Nov. 2007.

[3] ICRP, "The 2007 Recommendations of the International Commission on Radiological Protection," *Annals of the ICRP*, vol. 103, no. 37, 2007.

[4] O. US EPA, "Health Effects," Aug. 1997.

[5] A. J. Taylor, M. Cerqueira, J. M. Hodgson, D. Mark, J. Min, P. O'Gara, and G. D. Rubin, "ACCF/SCCT/ACR/AHA/ASE/ASNC/NASCI/SCAI/SCMR 2010 Appropriate Use Criteria for Cardiac Computed Tomography: A Report of the American College of Cardiology Foundation Appropriate Use Criteria Task Force, the Society of Cardiovascular Computed Tomography, the American College of Radiology, the American Heart Association, the American Society of Echocardiography, the American Society of Nuclear Cardiology, the North American Society for Cardiovascular Imaging, the Society for Cardiovascular Angiography and Interventions, and the Society for Cardiovascular Magnetic Resonance," *Journal of the American College of Cardiology*, vol. 56, pp. 1864–1894, Nov. 2010.

[6] W. Walker, B. Friemel, and G. Trahey, "Real-time imaging of tissue vibration using a two-dimensional speckle tracking system," in *Ultrasonics Symposium, 1993. Proceedings., IEEE 1993*, pp. 873–877 vol.2, Oct. 1993.

[7] E. A. Zerhouni, D. M. Parish, W. J. Rogers, A. Yang, and E. P. Shapiro, "Human heart: tagging with MR imaging–a method for noninvasive assessment of myocardial motion.," *Radiology*, vol. 169, pp. 59–63, Oct. 1988.

[8] A. Pourmorteza, K. H. Schuleri, D. A. Herzka, A. C. Lardo, and E. R. McVeigh, "A New Method for Cardiac Computed Tomography Regional Function AssessmentClinical Perspective Stretch Quantifier for

Endocardial Engraved Zones (SQUEEZ)," *Circulation: Cardiovascular Imaging*, vol. 5, pp. 243–250, Mar. 2012.

[9] J. Radon, "ber die Bestimmung von Funktionen durch ihre In-te-gral-werte lngs gewisser Mannigfaltigkeiten," *Ber. Verh. Schs. Akad. Wiss.*, vol. 69, pp. 262–277, 1917.

[10] R. Lozano, M. Naghavi, K. Foreman, S. Lim, K. Shibuya, V. Aboyans, J. Abraham, T. Adair, R. Aggarwal, S. Y. Ahn, M. A. AlMazroa, M. Alvarado, H. R. Anderson, L. M. Anderson, K. G. Andrews, C. Atkinson, L. M. Baddour, S. Barker-Collo, D. H. Bartels, M. L. Bell, E. J. Benjamin, D. Bennett, K. Bhalla, B. Bikbov, A. B. Abdulhak, G. Birbeck, F. Blyth, I. Bolliger, S. Boufous, C. Bucello, M. Burch, P. Burney, J. Carapetis, H. Chen, D. Chou, S. S. Chugh, L. E. Coffeng, S. D. Colan, S. Colquhoun, K. E. Colson, J. Condon, M. D. Connor, L. T. Cooper, M. Corriere, M. Cortinovis, K. C. de Vaccaro, W. Couser, B. C. Cowie, M. H. Criqui, M. Cross, K. C. Dabhadkar, N. Dahodwala, D. De Leo, L. Degenhardt, A. Delossantos, J. Denenberg, D. C. Des Jarlais, S. D. Dharmaratne, E. R. Dorsey, T. Driscoll, H. Duber, B. Ebel, P. J. Erwin, P. Espindola, M. Ezzati, V. Feigin, A. D. Flaxman, M. H. Forouzanfar, F. G. R. Fowkes, R. Franklin, M. Fransen, M. K. Freeman, S. E. Gabriel, E. Gakidou, F. Gaspari, R. F. Gillum, D. Gonzalez-Medina, Y. A. Halasa, D. Haring, J. E. Harrison, R. Havmoeller, R. J. Hay, B. Hoen, P. J. Hotez, D. Hoy, K. H. Jacobsen, S. L. James, R. Jasrasaria, S. Jayaraman, N. Johns, G. Karthikeyan, N. Kassebaum, A. Keren, J.-P. Khoo, L. M. Knowlton, O. Kobusingye, A. Koranteng, R. Krishnamurthi, M. Lipnick, S. E. Lipshultz, S. L. Ohno, J. Mabweijano, M. F. MacIntyre, L. Mallinger, L. March, G. B. Marks, R. Marks, A. Matsumori, R. Matzopoulos, B. M. Mayosi, J. H. McAnulty, M. M. McDermott, J. McGrath, Z. A. Memish, G. A. Mensah, T. R. Merriman, C. Michaud, M. Miller, T. R.

Miller, C. Mock, A. O. Mocumbi, A. A. Mokdad, A. Moran, K. Mulholland, M. N. Nair, L. Naldi, K. M. V. Narayan, K. Nasseri, P. Norman, M. O'Donnell, S. B. Omer, K. Ortblad, R. Osborne, D. Ozgediz, B. Pahari, J. D. Pandian, A. P. Rivero, R. P. Padilla, F. Perez-Ruiz, N. Perico, D. Phillips, K. Pierce, C. A. Pope III, E. Porrini, F. Pourmalek, M. Raju, D. Ranganathan, J. T. Rehm, D. B. Rein, G. Remuzzi, F. P. Rivara, T. Roberts, F. R. De Len, L. C. Rosenfeld, L. Rushton, R. L. Sacco, J. A. Salomon, U. Sampson, E. Sanman, D. C. Schwebel, M. Segui-Gomez, D. S. Shepard, D. Singh, J. Singleton, K. Sliwa, E. Smith, A. Steer, J. A. Taylor, B. Thomas, I. M. Tleyjeh, J. A. Towbin, T. Truelsen, E. A. Undurraga, N. Venketasubramanian, L. Vijayakumar, T. Vos, G. R. Wagner, M. Wang, W. Wang, K. Watt, M. A. Weinstock, R. Weintraub, J. D. Wilkinson, A. D. Woolf, S. Wulf, P.-H. Yeh, P. Yip, A. Zabetian, Z.-J. Zheng, A. D. Lopez, and C. J. Murray, "Global and regional mortality from 235 causes of death for 20 age groups in 1990 and 2010: a systematic analysis for the Global Burden of Disease Study 2010," *The Lancet*, vol. 380, pp. 2095–2128, Dec. 2012.

[11] V. L. Roger, A. S. Go, D. M. Lloyd-Jones, E. J. Benjamin, J. D. Berry, W. B. Borden, D. M. Bravata, S. Dai, E. S. Ford, C. S. Fox, H. J. Fullerton, C. Gillespie, S. M. Hailpern, J. A. Heit, V. J. Howard, B. M. Kissela, S. J. Kittner, D. T. Lackland, J. H. Lichtman, L. D. Lisabeth, D. M. Makuc, G. M. Marcus, A. Marelli, D. B. Matchar, C. S. Moy, D. Mozaffarian, M. E. Mussolino, G. Nichol, N. P. Paynter, E. Z. Soliman, P. D. Sorlie, N. Sotoodehnia, T. N. Turan, S. S. Virani, N. D. Wong, D. Woo, and M. B. Turner, "Heart Disease and Stroke Statistics2012 Update A Report From the American Heart Association," *Circulation*, vol. 125, pp. e2–e220, Jan. 2012.

[12] P. A. Cain, R. Ahl, E. Hedstrom, M. Ugander, A. Allansdotter-Johnsson, P. Friberg, and H. Arheden, "Age and gender specific normal values of left ventricular mass, volume and function for gradient echo magnetic resonance imaging: a cross sectional study," *BMC Medical Imaging*, vol. 9, p. 2, Jan. 2009.

[13] F. R. de Graaf, J. D. Schuijf, J. E. van Velzen, G. Nucifora, L. J. Kroft, A. de Roos, M. J. Schalij, J. W. Jukema, E. E. van der Wall, and J. J. Bax, "Assessment of global left ventricular function and volumes with 320-row multidetector computed tomography: A comparison with 2d-echocardiography," *Journal of Nuclear Cardiology: Official Publication of the American Society of Nuclear Cardiology*, vol. 17, pp. 225–231, Apr. 2010.

[14] H. Doan, L. J. M. Kroft, J. J. Bax, J. D. Schuijf, R. J. van der Geest, J. Doornbos, and A. de Roos, "MDCT assessment of right ventricular systolic function," *AJR. American journal of roentgenology*, vol. 186, pp. S366–370, June 2006.

[15] J. D. Schuijf, J. J. Bax, L. P. Salm, J. W. Jukema, H. J. Lamb, E. E. van der Wall, and A. de Roos, "Noninvasive coronary imaging and assessment of left ventricular function using 16-slice computed tomography," *The American Journal of Cardiology*, vol. 95, pp. 571–574, Mar. 2005.

[16] A. F. Frangi, W. J. Niessen, and M. A. Viergever, "Three-dimensional modeling for functional analysis of cardiac images, a review," *IEEE Transactions on Medical Imaging*, vol. 20, pp. 2–5, Jan. 2001.

[17] T. E. Owan, D. O. Hodge, R. M. Herges, S. J. Jacobsen, V. L. Roger, and M. M. Redfield, "Trends in Prevalence and Outcome of Heart Failure with Preserved Ejection Fraction," *New England Journal of Medicine*, vol. 355, pp. 251–259, July 2006.

[18] A. Desai and J. C. Fang, "Heart Failure with Preserved Ejection Fraction: Hypertension, Diabetes, Obesity/Sleep Apnea, and Hypertrophic and Infiltrative Cardiomyopathy," *Heart Failure Clinics*, vol. 4, pp. 87–97, Jan. 2008.

[19] D. E. Bild, D. A. Bluemke, G. L. Burke, R. Detrano, A. V. Diez Roux, A. R. Folsom, P. Greenland, D. R. JacobsJr., R. Kronmal, K. Liu, J. C. Nelson, D. OLeary, M. F. Saad, S. Shea, M. Szklo, and R. P. Tracy, "Multi-Ethnic Study of Atherosclerosis: Objectives and Design," *American Journal of Epidemiology*, vol. 156, pp. 871 –881, Nov. 2002.

[20] K. Ogawa, T. Hozumi, K. Sugioka, Y. Matsumura, M. Nishiura, R. Kanda, Y. Abe, Y. Takemoto, M. Yoshiyama, and J. Yoshikawa, "Usefulness of Automated Quantitation of Regional Left Ventricular Wall Motion by a Novel Method of Two-Dimensional Echocardiographic Tracking," *The American Journal of Cardiology*, vol. 98, pp. 1531–1537, Dec. 2006.

[21] J. D'hooge, A. Heimdal, F. Jamal, T. Kukulski, B. Bijnens, F. Rademakers, L. Hatle, P. Suetens, and G. R. Sutherland, "Regional strain and strain rate measurements by cardiac ultrasound: principles, implementation and limitations," *European journal of echocardiography: the journal of the Working Group on Echocardiography of the European Society of Cardiology*, vol. 1, pp. 154–170, Sept. 2000.

[22] J. P. A. Kuijer, J. T. Marcus, M. J. W. Gtte, A. C. van Rossum, and R. M. Heethaar, "Three-dimensional myocardial strains at end-systole and during diastole in the left ventricle of normal humans," *Journal of cardiovascular magnetic resonance: official journal of the Society for Cardiovascular Magnetic Resonance*, vol. 4, no. 3, pp. 341–351, 2002.

[23] M. J. Gtte, T. Germans, I. K. Rssel, J. J. Zwanenburg, J. T. Marcus, A. C. van Rossum, and D. J. van Veldhuisen, "Myocardial Strain and

Torsion Quantified by Cardiovascular Magnetic Resonance Tissue TaggingStudies in Normal and Impaired Left Ventricular Function," *Journal of the American College of Cardiology*, vol. 48, pp. 2002–2011, Nov. 2006.

[24] M. Ashraf, A. Myronenko, T. Nguyen, A. Inage, W. Smith, R. I. Lowe, K. Thiele, C. A. Gibbons Kroeker, J. V. Tyberg, J. F. Smallhorn, D. J. Sahn, and X. Song, "Defining Left Ventricular Apex-to-Base Twist Mechanics Computed From High-Resolution 3d Echocardiography: Validation Against Sonomicrometry," *JACC: Cardiovascular Imaging*, vol. 3, pp. 227–234, Mar. 2010.

[25] P. P. Sengupta, J. Korinek, M. Belohlavek, J. Narula, M. A. Vannan, A. Jahangir, and B. K. Khandheria, "Left Ventricular Structure and Function: Basic Science for Cardiac Imaging," *Journal of the American College of Cardiology*, vol. 48, pp. 1988–2001, Nov. 2006.

[26] V. Delgado, C. Ypenburg, R. J. van Bommel, L. F. Tops, S. A. Mollema, N. A. Marsan, G. B. Bleeker, M. J. Schalij, and J. J. Bax, "Assessment of Left Ventricular Dyssynchrony by Speckle Tracking Strain Imaging: Comparison Between Longitudinal, Circumferential, and Radial Strain in Cardiac Resynchronization Therapy," *Journal of the American College of Cardiology*, vol. 51, pp. 1944–1952, May 2008.

[27] E. J. Cho, P. Jiamsripong, A. M. Calleja, M. S. Alharthi, E. M. McMahon, B. K. Khandheria, and M. Belohlavek, "Right Ventricular Free Wall Circumferential Strain Reflects Graded Elevation in Acute Right Ventricular Afterload," *American Journal of Physiology - Heart and Circulatory Physiology*, vol. 296, pp. H413–H420, Feb. 2009.

[28] K. D. Horton, R. W. Meece, and J. C. Hill, "Assessment of the right ventricle by echocardiography: a primer for cardiac sonographers,"

Journal of the American Society of Echocardiography: Official Publication of the American Society of Echocardiography, vol. 22, pp. 776–792; quiz 861–862, July 2009.

[29] J. T. Marcus, M. J. W. Gtte, A. C. van Rossum, J. P. A. Kuijer, R. M. Heethaar, L. Axel, and C. A. Visser, "Myocardial function in infarcted and remote regions early after infarction in man: Assessment by magnetic resonance tagging and strain analysis," *Magnetic Resonance in Medicine*, vol. 38, no. 5, pp. 803–810, 1997.

[30] L. K. Waldman, Y. C. Fung, and J. W. Covell, "Transmural myocardial deformation in the canine left ventricle. Normal in vivo three-dimensional finite strains.," *Circulation Research*, vol. 57, pp. 152–163, July 1985.

[31] B. P. Cupps, B. J. Pomerantz, M. D. Krock, J. Villard, J. Rogers, N. Moazami, and M. K. Pasque, "Principal Strain Orientation in the Normal Human Left Ventricle," *The Annals of Thoracic Surgery*, vol. 79, pp. 1338–1343, Apr. 2005.

[32] C. Szmigielski, K. Rajpoot, V. Grau, S. G. Myerson, C. Holloway, J. A. Noble, R. Kerber, and H. Becher, "Real-time 3d fusion echocardiography," *JACC. Cardiovascular imaging*, vol. 3, pp. 682–690, July 2010.

[33] K. Rajpoot, V. Grau, J. A. Noble, C. Szmigielski, and H. Becher, "Multiview fusion 3-D echocardiography: improving the information and quality of real-time 3-D echocardiography," *Ultrasound in Medicine & Biology*, vol. 37, pp. 1056–1072, July 2011.

[34] G. Piella, M. D. Craene, C. Butakoff, V. Grau, C. Yao, S. Nedjati-Gilani, G. P. Penney, and A. F. Frangi, "Multiview diffeomorphic registration: Application to motion and strain estimation

from 3d echocardiography," *Medical Image Analysis*, vol. 17, pp. 348–364, Apr. 2013.

[35] V. Grau, H. Becher, and J. A. Noble, "Registration of multiview real-time 3-D echocardiographic sequences," *IEEE transactions on medical imaging*, vol. 26, pp. 1154–1165, Sept. 2007.

[36] G. Danelius, "Cross-sectional Radiography of the Heart," *Radiology*, vol. 32, pp. 190–194, Feb. 1939.

[37] H. Wang and A. A. Amini, "Cardiac motion and deformation recovery from MRI: a review," *IEEE Transactions on Medical Imaging*, vol. 31, pp. 487–503, Feb. 2012.

[38] K. N. Hor, W. M. Gottliebson, C. Carson, E. Wash, J. Cnota, R. Fleck, J. Wansapura, P. Klimeczek, H. R. Al-Khalidi, E. S. Chung, D. W. Benson, and W. Mazur, "Comparison of Magnetic Resonance Feature Tracking for Strain Calculation With Harmonic Phase Imaging Analysis," *JACC: Cardiovascular Imaging*, vol. 3, pp. 144–151, Feb. 2010.

[39] J. G. Bosch, S. C. Mitchell, B. P. Lelieveldt, F. Nijland, O. Kamp, M. Sonka, and J. H. Reiber, "Automatic segmentation of echocardiographic sequences by active appearance motion models," *IEEE Transactions on Medical Imaging*, vol. 21, pp. 1374–1383, Nov. 2002.

[40] D. A. Herzka, M. A. Guttman, and E. R. McVeigh, "Myocardial tagging with SSFP," *Magnetic Resonance in Medicine: Official Journal of the Society of Magnetic Resonance in Medicine / Society of Magnetic Resonance in Medicine*, vol. 49, pp. 329–340, Feb. 2003.

[41] S. Ubbink, P. Bovendeerd, T. Delhaas, T. Arts, and F. van de Vosse, "Towards model-based analysis of cardiac MR tagging data: Relation

between left ventricular shear strain and myofiber orientation," *Medical Image Analysis*, vol. 10, pp. 632–641, Aug. 2006.

[42] L. Axel and L. Dougherty, "MR imaging of motion with spatial modulation of magnetization.," *Radiology*, vol. 171, pp. 841–845, June 1989.

[43] L. Axel, A. Montillo, and D. Kim, "Tagged magnetic resonance imaging of the heart: a survey," *Medical Image Analysis*, vol. 9, pp. 376–393, Aug. 2005.

[44] J. L. Prince and E. R. McVeigh, "Motion estimation from tagged MR image sequences," *IEEE Transactions on Medical Imaging*, vol. 11, pp. 238–249, June 1992.

[45] M. Elliot R, "MRI of myocardial function: motion tracking techniques," *Magnetic Resonance Imaging*, vol. 14, no. 2, pp. 137–150, 1996.

[46] E. Castillo, N. F. Osman, B. D. Rosen, I. El-Shehaby, L. Pan, M. Jerosch-Herold, S. Lai, D. A. Bluemke, and J. A. C. Lima, "Quantitative assessment of regional myocardial function with MR-tagging in a multi-center study: interobserver and intraobserver agreement of fast strain analysis with Harmonic Phase (HARP) MRI," *Journal of cardiovascular magnetic resonance: official journal of the Society for Cardiovascular Magnetic Resonance*, vol. 7, no. 5, pp. 783–791, 2005.

[47] B. A. Venkatesh, S. Donekal, K. Yoneyama, C. Wu, V. R. Fernandes, B. D. Rosen, M. L. Shehata, R. McClelland, D. A. Bluemke, and J. A. Lima, "Regional myocardial functional patterns: Quantitative tagged magnetic resonance imaging in an adult population free of cardiovascular risk factors: The multi-ethnic study of atherosclerosis (MESA)," *Journal of Magnetic Resonance Imaging*, pp. n/a–n/a, 2014.

[48] A. de Roos and C. B. Higgins, "Cardiac Radiology: Centenary Review," *Radiology*, vol. 273, pp. S142–S159, Nov. 2014.

[49] D. C. Peters, F. H. Epstein, and E. R. McVeigh, "Myocardial Wall Tagging With Undersampled Projection Reconstruction," *Magnetic resonance in medicine : official journal of the Society of Magnetic Resonance in Medicine / Society of Magnetic Resonance in Medicine*, vol. 45, pp. 562–567, Apr. 2001.

[50] N. F. Osman, E. R. McVeigh, and J. L. Prince, "Imaging heart motion using harmonic phase MRI," *IEEE transactions on medical imaging*, vol. 19, pp. 186–202, Mar. 2000.

[51] K. N. Hor, R. Baumann, G. Pedrizzetti, G. Tonti, W. M. Gottliebson, M. Taylor, W. Benson, and W. Mazur, "Magnetic Resonance Derived Myocardial Strain Assessment Using Feature Tracking," *Journal of Visualized Experiments : JoVE*, Feb. 2011.

[52] A. Kempny, R. Fernndez-Jimnez, S. Orwat, P. Schuler, A. C. Bunck, D. Maintz, H. Baumgartner, and G. P. Diller, "Quantification of biventricular myocardial function using cardiac magnetic resonance feature tracking, endocardial border delineation and echocardiographic speckle tracking in patients with repaired tetralogy of fallot and healthy controls," *Journal of cardiovascular magnetic resonance: official journal of the Society for Cardiovascular Magnetic Resonance*, vol. 14, p. 32, May 2012.

[53] H. Geyer, G. Caracciolo, H. Abe, S. Wilansky, S. Carerj, F. Gentile, H.-J. Nesser, B. Khandheria, J. Narula, and P. P. Sengupta, "Assessment of Myocardial Mechanics Using Speckle Tracking Echocardiography: Fundamentals and Clinical Applications," *Journal of the American Society of Echocardiography*, vol. 23, pp. 351–369, Apr. 2010.

[54] M. Leitman, P. Lysyansky, S. Sidenko, V. Shir, E. Peleg, M. Binenbaum, E. Kaluski, R. Krakover, and Z. Vered, "Two-dimensional strain-a novel software for real-time quantitative echocardiographic assessment of myocardial function," *Journal of the American Society of Echocardiography: Official Publication of the American Society of Echocardiography*, vol. 17, pp. 1021–1029, Oct. 2004.

[55] W. Yu, P. Yan, A. J. Sinusas, K. Thiele, and J. S. Duncan, "Towards pointwise motion tracking in echocardiographic image sequences–comparing the reliability of different features for speckle tracking," *Medical Image Analysis*, vol. 10, pp. 495–508, Aug. 2006.

[56] M. Dandel, H. Lehmkuhl, C. Knosalla, N. Suramelashvili, and R. Hetzer, "Strain and Strain Rate Imaging by Echocardiography Basic Concepts and Clinical Applicability," *Current Cardiology Reviews*, vol. 5, pp. 133–148, May 2009.

[57] M. Mulet-Parada and J. Noble, "2d+T acoustic boundary detection in echocardiography," *Medical Image Analysis*, vol. 4, pp. 21–30, Mar. 2000.

[58] G. Coppini, R. Poli, and G. Valli, "Recovery of the 3-D shape of the left ventricle from echocardiographic images," *IEEE Transactions on Medical Imaging*, vol. 14, pp. 301–317, June 1995.

[59] Y. Zhu, X. Papademetris, A. J. Sinusas, and J. S. Duncan, "A coupled deformable model for tracking myocardial borders from real-time echocardiography using an incompressibility constraint," *Medical Image Analysis*, vol. 14, pp. 429–448, June 2010.

[60] X. Papademetris, A. J. Sinusas, D. P. Dione, R. T. Constable, and J. S. Duncan, "Estimation of 3-D left ventricular deformation from medical

images using biomechanical models," *IEEE Transactions on Medical Imaging*, vol. 21, pp. 786–800, July 2002.

[61] X. Papademetris, A. J. Sinusas, D. P. Dione, and J. S. Duncan, "Estimation of 3d left ventricular deformation from echocardiography," *Medical Image Analysis*, vol. 5, pp. 17–28, Mar. 2001.

[62] G. Jacob, J. A. Noble, C. Behrenbruch, A. D. Kelion, and A. P. Banning, "A shape-space-based approach to tracking myocardial borders and quantifying regional left-ventricular function applied in echocardiography," *IEEE Transactions on Medical Imaging*, vol. 21, pp. 226–238, Mar. 2002.

[63] F. Orderud and S. I. Rabben, "Real-time 3d segmentation of the left ventricle using deformable subdivision surfaces," in *IEEE Conference on Computer Vision and Pattern Recognition, 2008. CVPR 2008*, pp. 1–8, IEEE, June 2008.

[64] M. K. Kalra and T. J. Brady, "Current status and future directions in technical developments of cardiac computed tomography," *Journal of Cardiovascular Computed Tomography*, vol. 2, pp. 71–80, Mar. 2008.

[65] T. G. Flohr, U. Joseph Schoepf, and B. M. Ohnesorge, "Chasing the Heart," *Journal of Thoracic Imaging*, vol. 22, pp. 4–16, Feb. 2007.

[66] M. W. Itagaki, R. D. Suh, and J. G. Goldin, "Cardiac CT Research: Exponential Growth1," *Radiology*, vol. 252, pp. 468–476, Aug. 2009.

[67] A. de Roos, L. J. M. Kroft, J. J. Bax, and J. Geleijns, "Applications of multislice computed tomography in coronary artery disease," *Journal of magnetic resonance imaging: JMRI*, vol. 26, pp. 14–22, July 2007.

[68] A. de Roos, "CT and MRI of Coronary Artery Disease: Established and Emerging Applications," *Journal of Thoracic Imaging*, vol. 29, pp. 131–132, May 2014.

[69] G. Pundziute, J. D. Schuijf, J. W. Jukema, A. de Roos, E. E. van der Wall, and J. J. Bax, "Advances in the noninvasive evaluation of coronary artery disease with multislice computed tomography," *Expert Review of Medical Devices*, vol. 3, pp. 441–451, July 2006.

[70] J. D. Schuijf, G. Pundziute, J. W. Jukema, H. J. Lamb, B. L. van der Hoeven, A. de Roos, E. E. van der Wall, and J. J. Bax, "Diagnostic accuracy of 64-slice multislice computed tomography in the noninvasive evaluation of significant coronary artery disease," *The American Journal of Cardiology*, vol. 98, pp. 145–148, July 2006.

[71] R. Thompson and S. Cullom, "Issues regarding radiation dosage of cardiac nuclear and radiography procedures," *Journal of Nuclear Cardiology*, vol. 13, no. 1, pp. 19–23, 2006.

[72] S. Achenbach, "Limiting radiation exposure in coronary CT angiography: much can be achieved with little extra effort," *The International Journal of Cardiovascular Imaging (formerly Cardiac Imaging)*, vol. 25, no. 4, pp. 421–423, 2009.

[73] A. M. Cormack, "Representation of a Function by Its Line Integrals, with Some Radiological Applications," *Journal of Applied Physics*, vol. 34, no. 9, p. 2722, 1963.

[74] S. Mondillo, M. Galderisi, D. Mele, M. Cameli, V. S. Lomoriello, V. Zac, P. Ballo, A. DAndrea, D. Muraru, M. Losi, E. Agricola, A. DErrico, S. Buralli, S. Sciomer, S. Nistri, and L. Badano, "Speckle-Tracking Echocardiography," *Journal of Ultrasound in Medicine*, vol. 30, pp. 71–83, Jan. 2011.

[75] R. Citro, E. Bossone, B. Kuersten, G. Gregorio, and A. Salustri, "Tissue Doppler and strain imaging: anything left in the echo-lab?," *Cardiovascular Ultrasound*, vol. 6, p. 54, Oct. 2008.

[76] G. R. Sutherland, G. Di Salvo, P. Claus, J. D'hooge, and B. Bijnens, "Strain and strain rate imaging: a new clinical approach to quantifying regional myocardial function," *Journal of the American Society of Echocardiography: Official Publication of the American Society of Echocardiography*, vol. 17, pp. 788–802, July 2004.

[77] D. Y. Leung and A. C. Ng, "Emerging Clinical Role of Strain Imaging in Echocardiography," *Heart, Lung and Circulation*, vol. 19, pp. 161–174, Mar. 2010.

[78] G. C. Nesbitt, S. Mankad, and J. K. Oh, "Strain imaging in echocardiography: methods and clinical applications," *The international journal of cardiovascular imaging*, vol. 25 Suppl 1, pp. 9–22, Apr. 2009.

[79] S. Kutty, S. Rangamani, J. Venkataraman, L. Li, A. Schuster, S. E. Fletcher, D. A. Danford, and P. Beerbaum, "Reduced global longitudinal and radial strain with normal left ventricular ejection fraction late after effective repair of aortic coarctation: a CMR feature tracking study," *The International Journal of Cardiovascular Imaging*, vol. 29, pp. 141–150, May 2012.

[80] U. T. Truong, X. Li, C. S. Broberg, H. Houle, M. Schaal, M. Ashraf, P. Kilner, F. H. Sheehan, C. A. Sable, S. Ge, and D. J. Sahn, "Significance of Mechanical Alterations in Single Ventricle Patients on Twisting and Circumferential Strain as Determined by Analysis of Strain from Gradient Cine Magnetic Resonance Imaging Sequences," *The American Journal of Cardiology*, vol. 105, pp. 1465–1469, May 2010.

[81] A. A. W. Roest and A. de Roos, "Imaging of patients with congenital heart disease," *Nature Reviews. Cardiology*, vol. 9, pp. 101–115, Feb. 2012.

[82] R. W. C. Scherptong, S. A. Mollema, N. A. Blom, L. J. M. Kroft, A. de Roos, H. W. Vliegen, E. E. van der Wall, J. J. Bax, and E. R. Holman, "Right ventricular peak systolic longitudinal strain is a sensitive marker for right ventricular deterioration in adult patients with tetralogy of Fallot," *The International Journal of Cardiovascular Imaging*, vol. 25, pp. 669–676, Oct. 2009.

[83] N. Fallah-Rad, J. R. Walker, A. Wassef, M. Lytwyn, S. Bohonis, T. Fang, G. Tian, I. D. Kirkpatrick, P. K. Singal, M. Krahn, D. Grenier, and D. S. Jassal, "The Utility of Cardiac Biomarkers, Tissue Velocity and Strain Imaging, and Cardiac Magnetic Resonance Imaging in Predicting Early Left Ventricular Dysfunction in Patients With Human Epidermal Growth Factor Receptor IIPositive Breast Cancer Treated With Adjuvant Trastuzumab Therapy," *Journal of the American College of Cardiology*, vol. 57, pp. 2263–2270, May 2011.

[84] L. C. Afonso, J. Bernal, J. J. Bax, and T. P. Abraham, "Echocardiography in hypertrophic cardiomyopathy: the role of conventional and emerging technologies," *JACC. Cardiovascular imaging*, vol. 1, pp. 787–800, Nov. 2008.

[85] P. Heermann, D. M. Hedderich, M. Paul, C. Schlke, J. R. Kroeger, B. Baeler, T. Wichter, D. Maintz, J. Waltenberger, W. Heindel, and A. C. Bunck, "Biventricular myocardial strain analysis in patients with arrhythmogenic right ventricular cardiomyopathy (ARVC) using cardiovascular magnetic resonance feature tracking," *Journal of Cardiovascular Magnetic Resonance*, vol. 16, p. 75, Oct. 2014.

[86] J.-O. Choi, S. W. Cho, Y. B. Song, S. J. Cho, B. G. Song, S.-C. Lee, and S. W. Park, "Longitudinal 2d strain at rest predicts the presence of left main and three vessel coronary artery disease in patients without regional wall motion abnormality," *European Journal of*

Echocardiography: The Journal of the Working Group on Echocardiography of the European Society of Cardiology, vol. 10, pp. 695–701, July 2009.

[87] R. Citro and M. Galderisi, "Myocardial Postsystolic Motion in Ischemic and Not Ischemic Myocardium: The Clinical Value of Tissue Doppler," *Echocardiography*, vol. 22, pp. 525–532, July 2005.

[88] T. Edvardsen, H. Skulstad, S. Aakhus, S. Urheim, and H. Ihlen, "Regional myocardial systolic function during acute myocardial ischemia assessed by strain Doppler echocardiography," *Journal of the American College of Cardiology*, vol. 37, pp. 726–730, Mar. 2001.

[89] M. S. Suffoletto, K. Dohi, M. Cannesson, S. Saba, and J. Gorcsan, 3rd, "Novel speckle-tracking radial strain from routine black-and-white echocardiographic images to quantify dyssynchrony and predict response to cardiac resynchronization therapy," *Circulation*, vol. 113, pp. 960–968, Feb. 2006.

[90] G. Ansalone, P. Giannantoni, R. Ricci, P. Trambaiolo, F. Fedele, and M. Santini, "Doppler myocardial imaging to evaluate the effectiveness of pacing sites in patients receiving biventricular pacing," *J Am Coll Cardiol*, vol. 39, pp. 489–499, Feb. 2002.

[91] M. Saito, H. Okayama, T. Yoshii, H. Higashi, H. Morioka, G. Hiasa, T. Sumimoto, S. Inaba, K. Nishimura, K. Inoue, A. Ogimoto, Y. Shigematsu, M. Hamada, and J. Higaki, "Clinical significance of global two-dimensional strain as a surrogate parameter of myocardial fibrosis and cardiac events in patients with hypertrophic cardiomyopathy," *European Heart Journal Cardiovascular Imaging*, Jan. 2012.

[92] F. Weidemann, S. Herrmann, S. Strk, M. Niemann, S. Frantz, V. Lange, M. Beer, S. Gattenlhner, W. Voelker, G. Ertl, and J. M. Strotmann, "Impact of myocardial fibrosis in patients with symptomatic severe aortic stenosis," *Circulation*, vol. 120, pp. 577–584, Aug. 2009.

[93] F. Weidemann, M. Niemann, S. Herrmann, M. Kung, S. Strk, C. Waller, M. Beer, F. Breunig, C. Wanner, W. Voelker, G. Ertl, B. Bijnens, and J. M. Strotmann, "A new echocardiographic approach for the detection of non-ischaemic fibrosis in hypertrophic myocardium," *European Heart Journal*, vol. 28, pp. 3020–3026, Dec. 2007.

[94] M. Cameli, F. M. Righini, M. Lisi, and S. Mondillo, "Right ventricular strain as a novel approach to analyze right ventricular performance in patients with heart failure," *Heart Failure Reviews*, vol. 19, pp. 603–610, Nov. 2013.

[95] S. G. Portnoy and L. G. Rudski, "Echocardiographic evaluation of the right ventricle: a 2014 perspective," *Current Cardiology Reports*, vol. 17, p. 578, Apr. 2015.

[96] M. L. Shehata, S. Cheng, N. F. Osman, D. A. Bluemke, and J. A. Lima, "Myocardial tissue tagging with cardiovascular magnetic resonance," *Journal of Cardiovascular Magnetic Resonance*, vol. 11, p. 55, Dec. 2009.

[97] M. Tee, J. A. Noble, and D. A. Bluemke, "Imaging techniques for cardiac strain and deformation: comparison of echocardiography, cardiac magnetic resonance and cardiac computed tomography," *Expert review of cardiovascular therapy*, vol. 11, pp. 221–231, Feb. 2013.

[98] T. M. Helle-Valle, W.-C. Yu, V. R. Fernandes, B. D. Rosen, and J. A. Lima, "Usefulness of Radial Strain Mapping by Multidetector Computer Tomography to Quantify Regional Myocardial Function in

Patients With Healed Myocardial Infarction," *The American Journal of Cardiology*, vol. 106, pp. 483–491, Aug. 2010.

[99] M. I. S, A. de Roos, J. J. M. Westenberg, and L. J. M. Kroft, "Imaging techniques in cardiac resynchronization therapy," *The International Journal of Cardiovascular Imaging*, vol. 24, pp. 89–105, Jan. 2008.

[100] Q. A. Truong, J. P. Singh, C. P. Cannon, A. Sarwar, K. Nasir, A. Auricchio, F. F. Faletra, A. Sorgente, C. Conca, T. Moccetti, M. Handschumacher, T. J. Brady, and U. Hoffmann, "Quantitative Analysis of Intraventricular Dyssynchrony Using Wall Thickness by Multidetector Computed Tomography," *J Am Coll Cardiol Img*, vol. 1, pp. 772–781, Nov. 2008.

[101] M. F. Saeed, S. Premecz, V. Goyal, P. K. Singal, and D. S. Jassal, "Catching broken hearts: pre-clinical detection of doxorubicin and trastuzumab mediated cardiac dysfunction in the breast cancer setting," *Canadian Journal of Physiology and Pharmacology*, vol. 92, pp. 546–550, Jan. 2014.

[102] T. Ohtani, S. F. Mohammed, K. Yamamoto, S. M. Dunlay, S. A. Weston, Y. Sakata, R. J. Rodeheffer, V. L. Roger, and M. M. Redfield, "Diastolic stiffness as assessed by diastolic wall strain is associated with adverse remodelling and poor outcomes in heart failure with preserved ejection fraction," *European Heart Journal*, vol. 33, pp. 1742–1749, July 2012.

[103] Y.-H. Lai, C.-I. Lo, K.-T. Sung, J.-Y. Kuo, Y.-J. Wu, H.-I. Yeh, and C.-L. Hung, "THE CLINICAL USEFULNESS AND UTILIZATION OF TISSUE DOPPLER IMAGING, LONGITUDINAL AND CIRCUMFERENTIAL STRAIN AND STRAIN RATE IN THE DIAGNOSTIC ACCURACY FOR DIFFERENT PHENOTYPES OF

HEART FAILURE," *Journal of the American College of Cardiology*, vol. 61, Mar. 2013.

[104] E. Kraigher-Krainer, A. M. Shah, D. K. Gupta, A. Santos, B. Claggett, B. Pieske, M. R. Zile, A. A. Voors, M. P. Lefkowitz, M. Packer, J. J. V. McMurray, S. D. Solomon, and PARAMOUNT Investigators, "Impaired systolic function by strain imaging in heart failure with preserved ejection fraction," *Journal of the American College of Cardiology*, vol. 63, pp. 447–456, Feb. 2014.

[105] T. Edvardsen, T. Helle-Valle, and O. A. Smiseth, "Systolic Dysfunction in Heart Failure with Normal Ejection Fraction: Speckle-Tracking Echocardiography," *Progress in Cardiovascular Diseases*, vol. 49, pp. 207–214, Dec. 2006.

[106] F. Xie, Q. Zhou, Z. Zhou, G. Xu, H. Guan, and F. Liu, "[Evaluation of subclinical left ventricular systolic and diastolic function with velocity vector imaging in patients with latent autoimmune diabetes in adults]," *Zhong Nan Da Xue Xue Bao. Yi Xue Ban = Journal of Central South University. Medical Sciences*, vol. 34, pp. 1017–1022, Oct. 2009.

[107] H. Tsutsui, M. Tsuchihashi, and A. Takeshita, "Mortality and readmission of hospitalized patients with congestive heart failure and preserved versus depressed systolic function," *The American Journal of Cardiology*, vol. 88, pp. 530–533, Sept. 2001.

[108] N. Mewton, C. Y. Liu, P. Croisille, D. Bluemke, and J. A. Lima, "Assessment of Myocardial Fibrosis With Cardiovascular Magnetic Resonance," *Journal of the American College of Cardiology*, vol. 57, pp. 891–903, Feb. 2011.

[109] Z. B. Popovi, D. H. Kwon, M. Mishra, A. Buakhamsri, N. L. Greenberg, M. Thamilarasan, S. D. Flamm, J. D. Thomas, H. M. Lever,

and M. Y. Desai, "Association Between Regional Ventricular Function and Myocardial Fibrosis in Hypertrophic Cardiomyopathy Assessed by Speckle Tracking Echocardiography and Delayed Hyperenhancement Magnetic Resonance Imaging," *Journal of the American Society of Echocardiography*, vol. 21, pp. 1299–1305, Dec. 2008.

[110] S. Kuruvilla, R. Janardhanan, P. Antkowiak, E. C. Keeley, N. Adenaw, J. Brooks, F. H. Epstein, C. M. Kramer, and M. Salerno, "Increased Extracellular Volume and Altered Mechanics Are Associated With LVH inHypertensive Heart Disease, NotHypertension Alone," *JACC. Cardiovascular imaging*, vol. 8, pp. 172–180, Feb. 2015.

[111] J. A. Hiemstra, S. Liu, M. A. Ahlman, K. H. Schuleri, A. C. Lardo, C. P. Baines, K. C. Dellsperger, D. A. Bluemke, and C. A. Emter, "A new twist on an old idea: a two-dimensional speckle tracking assessment of cyclosporine as a therapeutic alternative for heart failure with preserved ejection fraction," *Physiological Reports*, vol. 1, no. 7, p. e00174, 2013.

[112] K. D. Marshall, B. N. Muller, M. Krenz, L. M. Hanft, K. S. McDonald, K. C. Dellsperger, and C. A. Emter, "Heart failure with preserved ejection fraction: chronic low-intensity interval exercise training preserves myocardial O2 balance and diastolic function," *Journal of applied physiology (Bethesda, Md.: 1985)*, vol. 114, pp. 131–147, Jan. 2013.

[113] C. A. Emter, D. L. Tharp, J. R. Ivey, V. K. Ganjam, and D. K. Bowles, "Low-intensity interval exercise training attenuates coronary vascular dysfunction and preserves Ca-sensitive K current in miniature swine with LV hypertrophy," *American journal of physiology. Heart and circulatory physiology*, vol. 301, pp. H1687–1694, Oct. 2011.

[114] J. Schulz-Menger, D. A. Bluemke, J. Bremerich, S. D. Flamm, M. A. Fogel, M. G. Friedrich, R. J. Kim, F. v. Knobelsdorff-Brenkenhoff, C. M. Kramer, D. J. Pennell, S. Plein, and E. Nagel, "Standardized image interpretation and post processing in cardiovascular magnetic resonance: Society for Cardiovascular Magnetic Resonance (SCMR) Board of Trustees Task Force on Standardized Post Processing," *Journal of Cardiovascular Magnetic Resonance*, vol. 15, p. 35, May 2013.

[115] M. D. Cerqueira, N. J. Weissman, V. Dilsizian, A. K. Jacobs, S. Kaul, W. K. Laskey, D. J. Pennell, J. A. Rumberger, T. Ryan, and M. S. Verani, "Standardized Myocardial Segmentation and Nomenclature for Tomographic Imaging of the Heart A Statement for Healthcare Professionals From the Cardiac Imaging Committee of the Council on Clinical Cardiology of the American Heart Association," *Circulation*, vol. 105, pp. 539–542, Jan. 2002.

[116] N. F. Osman, W. S. Kerwin, E. R. McVeigh, and J. L. Prince, "Cardiac motion tracking using CINE harmonic phase (HARP) magnetic resonance imaging," *Magnetic Resonance in Medicine: Official Journal of the Society of Magnetic Resonance in Medicine / Society of Magnetic Resonance in Medicine*, vol. 42, pp. 1048–1060, Dec. 1999.

[117] F. Cademartiri, K. Nieman, A. van der Lugt, R. H. Raaijmakers, N. Mollet, P. M. T. Pattynama, P. J. de Feyter, and G. P. Krestin, "Intravenous Contrast Material Administration at 16Detector Row Helical CT Coronary Angiography: Test Bolus versus Bolus-tracking Technique," *Radiology*, vol. 233, pp. 817–823, Dec. 2004.

[118] B. R. Annuar, C. K. Liew, S. P. Chin, T. K. Ong, M. T. Seyfarth, W. L. Chan, Y. Y. Fong, C. K. Ang, N. Lin, H. B. Liew, and K. H. Sim, "Assessment of global and regional left ventricular function using

64-slice multislice computed tomography and 2d echocardiography: a comparison with cardiac magnetic resonance," *European journal of radiology*, vol. 65, pp. 112–119, Jan. 2008.

[119] C. Asferg, L. Usinger, T. S. Kristensen, and J. Abdulla, "Accuracy of multi-slice computed tomography for measurement of left ventricular ejection fraction compared with cardiac magnetic resonance imaging and two-dimensional transthoracic echocardiography: a systematic review and meta-analysis," *European journal of radiology*, vol. 81, pp. e757–762, May 2012.

[120] Y.-W. Wu, E. Tadamura, M. Yamamuro, S. Kanao, S. Okayama, N. Ozasa, M. Toma, T. Kimura, M. Komeda, and K. Togashi, "Estimation of global and regional cardiac function using 64-slice computed tomography: A comparison study with echocardiography, gated-SPECT and cardiovascular magnetic resonance," *International Journal of Cardiology*, vol. 128, pp. 69–76, Aug. 2008.

[121] J. J. Bax, "Imaging: Myocardial thinning is not always transmural scarring," *Nature Reviews Cardiology*, vol. 10, pp. 370–371, July 2013.

[122] Shah DJ, Kim HW, James O, and et al, "PRevalence of regional myocardial thinning and relationship with myocardial scarring in patients with coronary artery disease," *JAMA*, vol. 309, pp. 909–918, Mar. 2013.

[123] T. P. Abraham and R. A. Nishimura, "Myocardial strain: can we finally measure contractility?," *J Am Coll Cardiol*, vol. 37, pp. 731–734, Mar. 2001.

[124] J. Dez, "Mechanisms of Cardiac Fibrosis in Hypertension," *The Journal of Clinical Hypertension*, vol. 9, pp. 546–550, July 2007.

[125] R. Martos, J. Baugh, M. Ledwidge, C. O'Loughlin, N. F. Murphy, C. Conlon, A. Patle, S. C. Donnelly, and K. McDonald, "Diagnosis of heart failure with preserved ejection fraction: improved accuracy with the use of markers of collagen turnover," *European Journal of Heart Failure*, vol. 11, pp. 191–197, Feb. 2009.

[126] G. Olivetti, G. Giordano, D. Corradi, M. Melissari, C. Lagrasta, S. R. Gambert, and P. Anversa, "Gender differences and aging: effects on the human heart," *Journal of the American College of Cardiology*, vol. 26, pp. 1068–1079, Oct. 1995.

[127] G. N. Hounsfield, "Computerized transverse axial scanning (tomography): Part 1. Description of system," *The British Journal of Radiology*, vol. 46, pp. 1016–1022, Dec. 1973.

[128] E. J. Hall and D. J. Brenner, "Cancer risks from diagnostic radiology: the impact of new epidemiological data," *The British Journal of Radiology*, vol. 85, pp. e1316–e1317, Dec. 2012.

[129] F. R. de Graaf, J. E. van Velzen, A. J. Witkowska, J. D. Schuijf, N. van der Bijl, L. J. Kroft, A. de Roos, J. H. C. Reiber, J. J. Bax, G. J. de Grooth, J. W. Jukema, and E. E. van der Wall, "Diagnostic performance of 320-slice multidetector computed tomography coronary angiography in patients after coronary artery bypass grafting," *European Radiology*, vol. 21, pp. 2285–2296, Nov. 2011.

[130] K. Nikolaou, A. Knez, C. Rist, B. J. Wintersperger, A. Leber, T. Johnson, M. F. Reiser, and C. R. Becker, "Accuracy of 64-MDCT in the Diagnosis of Ischemic Heart Disease," *American Journal of Roentgenology*, vol. 187, pp. 111–117, July 2006.

[131] J. Hausleiter, S. Martinoff, M. Hadamitzky, E. Martuscelli, I. Pschierer, G. M. Feuchtner, P. Cataln-Sanz, B. Czermak, T. S. Meyer, F. Hein,

B. Bischoff, M. Kuse, A. Schmig, and S. Achenbach, "Image quality and radiation exposure with a low tube voltage protocol for coronary CT angiography results of the PROTECTION II Trial," *JACC. Cardiovascular imaging*, vol. 3, pp. 1113–1123, Nov. 2010.

[132] M. Y. Chen, S. M. Shanbhag, and A. E. Arai, "Submillisievert Median Radiation Dose for Coronary Angiography with a Second-Generation 320Detector Row CT Scanner in 107 Consecutive Patients," *Radiology*, vol. 267, pp. 76–85, Apr. 2013.

[133] M. K. Tung, J. D. Cameron, J. M. Casan, M. Crossett, J. M. Troupis, I. T. Meredith, and S. K. Seneviratne, "Radiation dose in 320-slice multidetector cardiac CT: A single center experience of evolving dose minimization," *Journal of Cardiovascular Computed Tomography*, vol. 7, pp. 157–166, May 2013.

[134] J. Hausleiter, T. Meyer, F. Hermann, M. Hadamitzky, M. Krebs, T. C. Gerber, C. McCollough, S. Martinoff, A. Kastrati, A. Schmig, and S. Achenbach, "Estimated radiation dose associated with cardiac CT angiography," *JAMA*, vol. 301, pp. 500–507, Feb. 2009.

[135] T. Knickelbine, J. R. Lesser, T. S. Haas, E. R. Brandenburg, B. K. Gleason-Han, B. Flygenring, T. F. Longe, R. S. Schwartz, and B. J. Maron, "Identification of unexpected nonatherosclerotic cardiovascular disease with coronary CT angiography," *JACC. Cardiovascular imaging*, vol. 2, pp. 1085–1092, Sept. 2009.

[136] W. R. Hendee and M. K. O'Connor, "Radiation risks of medical imaging: separating fact from fantasy," *Radiology*, vol. 264, pp. 312–321, Aug. 2012.

[137] C.-M. Chen, Y.-C. Liu, C.-C. Chen, M.-S. Wen, C.-F. Hung, and Y.-L. Wan, "Radiation dose exposure of patients undergoing 320-row cardiac

CT for assessing coronary angiography and global left ventricular function," *The International Journal of Cardiovascular Imaging*, vol. 28, pp. 1–5, June 2012.

[138] A. Ng and J. Swanevelder, "Resolution in ultrasound imaging," *Continuing Education in Anaesthesia, Critical Care & Pain*, vol. 11, pp. 186–192, Oct. 2011.

[139] G. S. Slavin and D. A. Bluemke, "Spatial and Temporal Resolution in Cardiovascular MR Imaging: Review and Recommendations," *Radiology*, vol. 234, pp. 330–338, Feb. 2005.

[140] H. Brodoefel, U. Kramer, A. Reimann, C. Burgstahler, S. Schroeder, A. Kopp, and M. Heuschmid, "Dual-Source CT with Improved Temporal Resolution in Assessment of Left Ventricular Function: A Pilot Study," *American Journal of Roentgenology*, vol. 189, pp. 1064–1070, Nov. 2007.

[141] A. H. Mahnken, C. Hohl, C. Suess, H. Bruder, G. Muhlenbruch, M. Das, R. W. Gunther, and J. E. Wildberger, "Influence of Heart Rate and Temporal Resolution on Left-Ventricular Volumes in Cardiac Multislice Spiral Computed Tomography: A Phantom Study," *Investigative Radiology May 2006*, vol. 41, no. 5, pp. 429–435, 2006.

[142] S. Miller, O. P. Simonetti, J. Carr, U. Kramer, and J. P. Finn, "MR Imaging of the heart with cine true fast imaging with steady-state precession: influence of spatial and temporal resolutions on left ventricular functional parameters," *Radiology*, vol. 223, pp. 263–269, Apr. 2002.

[143] B. Bischoff, F. Hein, T. Meyer, M. Hadamitzky, S. Martinoff, A. Schmig, and J. Hausleiter, "Impact of a reduced tube voltage on CT

angiography and radiation dose: results of the PROTECTION I study," *JACC. Cardiovascular imaging*, vol. 2, pp. 940–946, Aug. 2009.

[144] J. Blobel, H. Baartman, P. Rogalla, J. Mews, and A. Lembcke, "[Spatial and temporal resolution with 16-slice computed tomography for cardiac imaging]," *RFo: Fortschritte Auf Dem Gebiete Der Rntgenstrahlen Und Der Nuklearmedizin*, vol. 175, pp. 1264–1271, Sept. 2003.

[145] M. Mahesh and D. D. Cody, "Physics of Cardiac Imaging with Multiple-Row Detector CT1," *Radiographics*, vol. 27, pp. 1495–1509, Sept. 2007.

[146] S. S. Halliburton, S. Abbara, M. Y. Chen, R. Gentry, M. Mahesh, G. L. Raff, L. J. Shaw, J. Hausleiter, and Society of Cardiovascular Computed Tomography, "SCCT guidelines on radiation dose and dose-optimization strategies in cardiovascular CT," *Journal of Cardiovascular Computed Tomography*, vol. 5, pp. 198–224, Aug. 2011.

[147] R. A. P. Takx, A. Moscariello, U. J. Schoepf, J. M. Barraza, J. W. Nance, G. Bastarrika, M. Das, M. Meyer, J. E. Wildberger, S. O. Schoenberg, C. Fink, and T. Henzler, "Quantification of left and right ventricular function and myocardial mass: comparison of low-radiation dose 2nd generation dual-source CT and cardiac MRI," *European Journal of Radiology*, vol. 81, pp. e598–604, Apr. 2012.

[148] M. Dewey, E. Zimmermann, F. Deissenrieder, M. Laule, H.-P. Dbel, P. Schlattmann, F. Knebel, W. Rutsch, and B. Hamm, "Noninvasive Coronary Angiography by 320-Row Computed Tomography With Lower Radiation Exposure and Maintained Diagnostic Accuracy Comparison of Results With Cardiac Catheterization in a Head-to-Head Pilot Investigation," *Circulation*, vol. 120, pp. 867–875, Sept. 2009.

[149] A. Pursnani, A. M. Lee, T. Mayrhofer, M. Panagia, U. Sharma, U. Hoffmann, S. Abbara, and B. Ghoshhajra, "Feasibility of a Radiation Dose Conserving CT Protocol for Myocardial Function Assessment," *The British Journal of Radiology*, p. 20130755, June 2014.

[150] N. US Department of Commerce, "NIST: X-Ray Mass Attenuation Coefficients."

[151] Y. Yamada, M. Jinzaki, T. Hosokawa, Y. Tanami, H. Sugiura, T. Abe, and S. Kuribayashi, "Dose reduction in chest CT: Comparison of the adaptive iterative dose reduction 3d, adaptive iterative dose reduction, and filtered back projection reconstruction techniques," *European Journal of Radiology*, vol. 81, pp. 4185–4195, Dec. 2012.

[152] M. Y. Chen, M. L. Steigner, S. W. Leung, K. K. Kumamaru, K. Schultz, R. T. Mather, A. E. Arai, and F. J. Rybicki, "Simulated 50 % radiation dose reduction in coronary CT angiography using adaptive iterative dose reduction in three-dimensions (AIDR3d)," *The International Journal of Cardiovascular Imaging*, vol. 29, pp. 1167–1175, Feb. 2013.

[153] K. Kitagawa, R. T. George, A. Arbab-Zadeh, J. A. C. Lima, and A. C. Lardo, "Characterization and correction of beam-hardening artifacts during dynamic volume CT assessment of myocardial perfusion," *Radiology*, vol. 256, pp. 111–118, July 2010.

[154] D. S. Gierada, A. J. Bierhals, C. K. Choong, S. T. Bartel, J. H. Ritter, N. A. Das, C. Hong, T. K. Pilgram, K. T. Bae, B. R. Whiting, J. C. Woods, J. C. Hogg, B. A. Lutey, R. J. Battafarano, J. D. Cooper, B. F. Meyers, and G. A. Patterson, "Effects of CT section thickness and reconstruction kernel on emphysema quantification relationship to the magnitude of the CT emphysema index," *Academic Radiology*, vol. 17, pp. 146–156, Feb. 2010.

[155] M. F. McNitt-Gray, "AAPM/RSNA Physics Tutorial for Residents: Topics in CT," *RadioGraphics*, vol. 22, pp. 1541–1553, Nov. 2002.

[156] G. Bongartz, S. Golding, and A. Jurik, "European Guidelines for Multislice Computed Tomography: Appendix C. Funded by the European Commission. Contract No. FIGM-CT2000-20078-CT-TIP.," *Luxembourg:European Commission*, Mar. 2004.

[157] J. Boone, K. Strauss, and D. Cody, "Size specific dose estimates (SSDE) in pediatric and adult body CT examinations. Report of American Association of Physicists in Medicine (AAPM) Task Group 204. College Park, Md, American Association of Physicists in Medicine.," 2011.

[158] S. L. Brady and R. A. Kaufman, "Investigation of American Association of Physicists in Medicine Report 204 Size-specific Dose Estimates for Pediatric CT Implementation," *Radiology*, vol. 265, pp. 832–840, Dec. 2012.

[159] J. P. Earls and J. Leipsic, "Cardiac Computed Tomography Technology and Dose-reduction Strategies," *Radiologic Clinics of North America*, vol. 48, pp. 657–674, July 2010.

[160] H. J. Otero, M. L. Steigner, and F. J. Rybicki, "The "post-64" era of coronary CT angiography: understanding new technology from physical principles," *Radiologic clinics of North America*, vol. 47, pp. 79–90, Jan. 2009.

[161] H. Xue, P. Kellman, G. LaRocca, A. E. Arai, and M. S. Hansen, "High spatial and temporal resolution retrospective cine cardiovascular magnetic resonance from shortened free breathing real-time acquisitions," *Journal of Cardiovascular Magnetic Resonance*, vol. 15, p. 102, Nov. 2013.

[162] A. Gervaise, B. Osemont, S. Lecocq, A. Noel, E. Micard, J. Felblinger, and A. Blum, "CT image quality improvement using adaptive iterative dose reduction with wide-volume acquisition on 320-detector CT," *European Radiology*, vol. 22, pp. 295–301, Feb. 2012.

[163] K. T. Bae, "Intravenous Contrast Medium Administration and Scan Timing at CT: Considerations and Approaches," *Radiology*, vol. 256, pp. 32–61, July 2010.

[164] K. T. Bae, J. P. Heiken, and J. A. Brink, "Aortic and hepatic contrast medium enhancement at CT. Part II. Effect of reduced cardiac output in a porcine model.," *Radiology*, vol. 207, pp. 657–662, June 1998.

[165] B. Ruzsics, H. Lee, P. L. Zwerner, M. Gebregziabher, P. Costello, and U. J. Schoepf, "Dual-energy CT of the heart for diagnosing coronary artery stenosis and myocardial ischemia-initial experience," *European Radiology*, vol. 18, pp. 2414–2424, Nov. 2008.

[166] I. Mirsky and W. W. Parmley, "Assessment of Passive Elastic Stiffness for Isolated Heart Muscle and the Intact Heart," *Circulation Research*, vol. 33, pp. 233–243, Aug. 1973.

[167] W. S. Kerwin, W. S. Kerwin, J. L. Prince, and J. L. Prince, *Cardiac Material Markers from Tagged MR Images*. 1998.

[168] D. Shen and C. Davatzikos, "HAMMER: Hierarchical attribute matching mechanism for elastic registration," *IEEE Transactions on Medical Imaging*, vol. 21, no. 11, pp. 1421–1439, 2002.

[169] D. Shen, H. Sundar, Z. Xue, Y. Fan, and H. Litt, "Consistent estimation of cardiac motions by 4d image registration," in *In Proc. MICCAI*, pp. 902–910, 2005.

[170] K. Rajpoot, A. Noble, V. Grau, and N. M. Rajpoot, "Feature Detection from Echocardiography Images Using Local Phase Information," 2008.

[171] K. Rajpoot, V. Grau, and J. Noble, "Local-phase based 3d boundary detection using monogenic signal and its application to real-time 3-D echocardiography images," in *IEEE International Symposium on Biomedical Imaging: From Nano to Macro, 2009. ISBI '09*, pp. 783 –786, July 2009.

[172] Q. Wang, G. Wu, P.-T. Yap, and D. Shen, "Attribute vector guided groupwise registration," *NeuroImage*, vol. 50, pp. 1485–1496, May 2010.

[173] M. Felsberg and G. Sommer, "The monogenic signal," *IEEE Transactions on Signal Processing*, vol. 49, pp. 3136 –3144, Dec. 2001.

[174] G. Carneiro and A. D. Jepson, "Phase-Based Local Features," in *Computer Vision ECCV 2002* (A. Heyden, G. Sparr, M. Nielsen, and P. Johansen, eds.), no. 2350 in Lecture Notes in Computer Science, pp. 282–296, Springer Berlin Heidelberg, Jan. 2002.

[175] S. Arivazhagan, V. Mani, and G. Prema, "Nonrigid image registration using spatial and multiresolution techniques," in *2011 International Conference on Signal Processing, Communication, Computing and Networking Technologies (ICSCCN)*, pp. 818–823, 2011.

[176] S. S. Sagel, E. S. Weiss, R. G. Gillard, G. N. Hounsfield, G. T. Jost, R. J. Stanley, and M. M. Ter-Pogossian, "Gated computed tomography of the human heart," *Investigative Radiology*, vol. 12, pp. 563–566, Dec. 1977.

[177] M. J. Lipton, C. B. Higgins, and D. P. Boyd, "Computed tomography of the heart: evaluation of anatomy and function," *Journal of the American College of Cardiology*, vol. 5, pp. 55S–69S, Jan. 1985.

[178] P. Lamata, R. Casero, V. Carapella, S. A. Niederer, M. J. Bishop, J. E. Schneider, P. Kohl, and V. Grau, "Images as drivers of progress in cardiac computational modelling," *Progress in Biophysics and Molecular Biology*, vol. 115, pp. 198–212, Aug. 2014.

[179] T. McInerney and D. Terzopoulos, "Deformable models in medical image analysis," in *, Proceedings of the Workshop on Mathematical Methods in Biomedical Image Analysis, 1996*, pp. 171–180, IEEE, June 1996.

[180] A. Nealen, M. Mller, R. Keiser, E. Boxerman, and M. Carlson, "Physically Based Deformable Models in Computer Graphics," *Computer Graphics Forum*, vol. 25, pp. 809–836, Dec. 2006.

[181] M. Kass, A. Witkin, and D. Terzopoulos, "Snakes: Active contour models," *International Journal of Computer Vision*, vol. 1, pp. 321–331, Jan. 1988.

[182] D. Rueckert, L. I. Sonoda, C. Hayes, D. L. G. Hill, M. O. Leach, and D. J. Hawkes, "Nonrigid registration using free-form deformations: Application to breast MR images," *IEEE Transactions on Medical Imaging*, vol. 18, pp. 712–721, 1999.

[183] D. Metaxas and D. Terzopoulos, "Constrained deformable superquadrics and nonrigid motion tracking," in *, IEEE Computer Society Conference on Computer Vision and Pattern Recognition, 1991. Proceedings CVPR '91*, pp. 337–343, June 1991.

[184] N. Paragios and R. Deriche, "Geodesic active contours and level sets for the detection and tracking of moving objects," *IEEE Transactions on Pattern Analysis and Machine Intelligence*, vol. 22, pp. 266–280, Mar. 2000.

[185] X. Papademetris, A. J. Sinusas, D. P. Dione, R. T. Constable, and J. S. Duncan, "Estimating 3d Strain from 4d Cine-MRI and Echocardiography: In-Vivo Validation," in *Medical Image Computing and Computer-Assisted Intervention MICCAI 2000* (S. L. Delp, A. M. DiGoia, and B. Jaramaz, eds.), no. 1935 in Lecture Notes in Computer Science, pp. 678–686, Springer Berlin Heidelberg, 2000.

[186] R. Jasaityte, B. Heyde, and J. Dhooge, "Current State of Three-Dimensional Myocardial Strain Estimation Using Echocardiography," *Journal of the American Society of Echocardiography*, vol. 26, pp. 15–28, Jan. 2013.

[187] Y. Chen and A. A. Amini, "A MAP framework for tag line detection in SPAMM data using Markov random fields on the B-spline solid," *IEEE Transactions on Medical Imaging*, vol. 21, pp. 1110–1122, Sept. 2002.

[188] C. C. Moore, C. H. Lugo-Olivieri, E. R. McVeigh, and E. A. Zerhouni, "Three-dimensional Systolic Strain Patterns in the Normal Human Left Ventricle: Characterization with Tagged MR Imaging1," *Radiology*, vol. 214, pp. 453–466, Feb. 2000.

[189] J. Huang, D. Abendschein, V. G. Dvila-Romn, and A. A. Amini, "Spatio-temporal tracking of myocardial deformations with a 4-D B-spline model from tagged MRI," *IEEE transactions on medical imaging*, vol. 18, pp. 957–972, Oct. 1999.

[190] M. Sermesant, C. Forest, X. Pennec, H. Delingette, and N. Ayache, "Deformable biomechanical models: Application to 4d cardiac image analysis," *Medical Image Analysis*, vol. 7, pp. 475–488, Dec. 2003.

[191] K.-J. Bathe, *Finite Element Procedures*. Klaus-Jurgen Bathe, 2006.

[192] Q. Fang and D. A. Boas, "Tetrahedral mesh generation from volumetric binary and grayscale images," in *Biomedical Imaging: From Nano to*

Macro, 2009. ISBI'09. IEEE International Symposium on, pp. 1142–1145, IEEE, 2009.

[193] A. McCulloch, J. Bassingthwaighte, P. Hunter, and D. Noble, "Computational biology of the heart: from structure to function," *Progress in biophysics and molecular biology*, vol. 69, no. 0, pp. 153–155, 1998.

[194] K. Wong, L. Wang, H. Zhang, H. Liu, and P. Shi, "Physiological Fusion of Functional and Structural Images for Cardiac Deformation Recovery," *IEEE Transactions on Medical Imaging*, vol. 30, no. 4, pp. 990–1000, 2011.

[195] A. Sotiras, C. Davatzikos, and N. Paragios, "Deformable medical image registration: a survey," *IEEE transactions on medical imaging*, vol. 32, pp. 1153–1190, July 2013.

[196] L. Glass, P. Hunter, and A. McCulloch, eds., *Theory of Heart*. Institute for Nonlinear Science, New York, NY: Springer New York, 1991.

[197] G. Holzapfel, *Nonlinear Solid Mechanics: A Continuum Approach for Engineering*. John Wiley & Sons Ltd., 2000.

[198] A. K. Slone, C. Bailey, and M. Cross, "Dynamic solid mechanics using finite volume methods," *Applied Mathematical Modelling*, vol. 27, pp. 69–87, Feb. 2003.

[199] J. S. Chuang, A. Zemljic-Harpf, R. S. Ross, L. R. Frank, A. D. McCulloch, and J. H. Omens, "Determination of Three-Dimensional Ventricular Strain Distributions in Gene-Targeted Mice Using Tagged MRI," *Magnetic Resonance in Medicine*, vol. 64, pp. 1281–1288, Nov. 2010.

[200] A. H. Mahnken, P. Bruners, M. Katoh, J. E. Wildberger, R. W. Gnther, and A. Buecker, "Dynamic multi-section CT imaging in acute myocardial infarction: preliminary animal experience," *European Radiology*, vol. 16, pp. 746–752, Mar. 2006.

[201] M. Yamamuro, E. Tadamura, S. Kubo, H. Toyoda, T. Nishina, M. Ohba, R. Hosokawa, T. Kimura, N. Tamaki, M. Komeda, T. Kita, and J. Konishi, "Cardiac functional analysis with multi-detector row CT and segmental reconstruction algorithm: comparison with echocardiography, SPECT, and MR imaging," *Radiology*, vol. 234, pp. 381–390, Feb. 2005.

[202] M. Dewey, M. Mller, S. Eddicks, D. Schnapauff, F. Teige, W. Rutsch, A. C. Borges, and B. Hamm, "Evaluation of global and regional left ventricular function with 16-slice computed tomography, biplane cineventriculography, and two-dimensional transthoracic echocardiography: comparison with magnetic resonance imaging," *Journal of the American College of Cardiology*, vol. 48, pp. 2034–2044, Nov. 2006.

[203] M. M. Henneman, J. D. Schuijf, J. W. Jukema, E. R. Holman, H. J. Lamb, A. de Roos, E. E. van der Wall, and J. J. Bax, "Assessment of global and regional left ventricular function and volumes with 64-slice MSCT: A comparison with 2d echocardiography," *Journal of Nuclear Cardiology*, vol. 13, pp. 480–487, July 2006.

[204] M. M. Henneman, J. J. Bax, J. D. Schuijf, J. W. Jukema, E. R. Holman, M. P. M. Stokkel, H. J. Lamb, A. de Roos, and E. E. van der Wall, "Global and regional left ventricular function: a comparison between gated SPECT, 2d echocardiography and multi-slice computed tomography," *European Journal of Nuclear Medicine and Molecular Imaging*, vol. 33, pp. 1452–1460, Dec. 2006.

[205] L. P. Salm, J. D. Schuijf, A. de Roos, H. J. Lamb, H. W. Vliegen, J. W. Jukema, R. Joemai, E. E. van der Wall, and J. J. Bax, "Global and regional left ventricular function assessment with 16-detector row CT: comparison with echocardiography and cardiovascular magnetic resonance," *European Journal of Echocardiography: The Journal of the Working Group on Echocardiography of the European Society of Cardiology*, vol. 7, pp. 308–314, Aug. 2006.

[206] J. Butler, M. D. Shapiro, D. S. Jassal, D. Jassal, T. G. Neilan, T. Neilan, J. Nichols, M. Ferencik, T. J. Brady, U. Hoffmann, and R. C. Cury, "Comparison of multidetector computed tomography and two-dimensional transthoracic echocardiography for left ventricular assessment in patients with heart failure," *The American Journal of Cardiology*, vol. 99, pp. 247–249, Jan. 2007.

[207] A. Nasis, S. Moir, S. K. Seneviratne, J. D. Cameron, and P. M. Mottram, "Assessment of left ventricular volumes, ejection fraction and regional wall motion with retrospective electrocardiogram triggered 320-detector computed tomography: a comparison with 2d-echocardiography," *The International Journal of Cardiovascular Imaging*, vol. 28, pp. 955–963, Apr. 2012.

[208] R. Fischbach, K. U. Juergens, M. Ozgun, D. Maintz, M. Grude, H. Seifarth, W. Heindel, and T. Wichter, "Assessment of regional left ventricular function with multidetector-row computed tomography versus magnetic resonance imaging," *European Radiology*, vol. 17, pp. 1009–1017, Apr. 2007.

[209] R. C. Cury, K. Nieman, M. D. Shapiro, J. Butler, C. H. Nomura, M. Ferencik, U. Hoffmann, S. Abbara, D. S. Jassal, T. Yasuda, H. K. Gold, I.-K. Jang, and T. J. Brady, "Comprehensive assessment of myocardial perfusion defects, regional wall motion, and left ventricular

function by using 64-section multidetector CT," *Radiology*, vol. 248, pp. 466–475, Aug. 2008.

[210] M. Sermesant, H. Delingette, and N. Ayache, "An electromechanical model of the heart for image analysis and simulation," *IEEE Transactions on Medical Imaging*, vol. 25, pp. 612–625, May 2006.

[211] N. A. Trayanova, "Whole-Heart Modeling Applications to Cardiac Electrophysiology and Electromechanics," *Circulation Research*, vol. 108, pp. 113–128, Jan. 2011.

[212] E. J. Vigmond and C. Clements, "Construction of a Computer Model to Investigate Sawtooth Effects in the Purkinje System," *IEEE Transactions on Biomedical Engineering*, vol. 54, pp. 389–399, Mar. 2007.

[213] Y. Xie, A. Garfinkel, P. Camelliti, P. Kohl, J. N. Weiss, and Z. Qu, "Effects of fibroblast-myocyte coupling on cardiac conduction and vulnerability to reentry: A computational study," *Heart Rhythm: The Official Journal of the Heart Rhythm Society*, vol. 6, pp. 1641–1649, Nov. 2009.

[214] G. A. Holzapfel and R. W. Ogden, "Constitutive modelling of passive myocardium: a structurally based framework for material characterization," *Philosophical Transactions. Series A, Mathematical, Physical, and Engineering Sciences*, vol. 367, pp. 3445–3475, Sept. 2009.

[215] W. A. Kalender, W. Seissler, E. Klotz, and P. Vock, "Spiral volumetric CT with single-breath-hold technique, continuous transport, and continuous scanner rotation," *Radiology*, vol. 176, pp. 181–183, July 1990.

[216] M. C. Williams, J. H. Reid, G. McKillop, N. W. Weir, E. J. R. v. Beek, N. G. Uren, and D. E. Newby, "Cardiac and coronary CT

comprehensive imaging approach in the assessment of coronary heart disease," *Heart*, vol. 97, pp. 1198–1205, Aug. 2011.

[217] M. G. Friedrich, C. Bucciarelli-Ducci, J. A. White, S. Plein, J. C. Moon, A. G. Almeida, C. M. Kramer, S. Neubauer, D. J. Pennell, S. E. Petersen, R. Y. Kwong, V. A. Ferrari, J. Schulz-Menger, H. Sakuma, E. B. Schelbert, r. Larose, I. Eitel, I. Carbone, A. J. Taylor, A. Young, A. de Roos, and E. Nagel, "Simplifying cardiovascular magnetic resonance pulse sequence terminology," *Journal of Cardiovascular Magnetic Resonance: Official Journal of the Society for Cardiovascular Magnetic Resonance*, vol. 16, p. 3960, 2014.

[218] S. A. Kleijn, W. P. Brouwer, M. F. A. Aly, I. K. Rssel, G. J. d. Roest, A. M. Beek, A. C. v. Rossum, and O. Kamp, "Comparison between three-dimensional speckle-tracking echocardiography and cardiac magnetic resonance imaging for quantification of left ventricular volumes and function," *European Heart Journal Cardiovascular Imaging*, p. jes030, Feb. 2012.

[219] K. Saito, H. Okura, N. Watanabe, A. Hayashida, K. Obase, K. Imai, T. Maehama, T. Kawamoto, Y. Neishi, and K. Yoshida, "Comprehensive Evaluation of Left Ventricular Strain Using Speckle Tracking Echocardiography in Normal Adults: Comparison of Three-Dimensional and Two-Dimensional Approaches," *Journal of the American Society of Echocardiography*, vol. 22, pp. 1025–1030, Sept. 2009.

[220] L. P. Badano, U. Cucchini, D. Muraru, O. A. Nono, C. Sarais, and S. Iliceto, "Use of three-dimensional speckle tracking to assess left ventricular myocardial mechanics: inter-vendor consistency and reproducibility of strain measurements," *European Heart Journal - Cardiovascular Imaging*, p. jes184, Sept. 2012.

[221] E. Gayat, H. Ahmad, L. Weinert, R. M. Lang, and V. Mor-Avi, "Reproducibility and inter-vendor variability of left ventricular deformation measurements by three-dimensional speckle-tracking echocardiography," *Journal of the American Society of Echocardiography: Official Publication of the American Society of Echocardiography*, vol. 24, pp. 878–885, Aug. 2011.

[222] T. H. Marwick, "Consistency of myocardial deformation imaging between vendors," *European Journal of Echocardiography: The Journal of the Working Group on Echocardiography of the European Society of Cardiology*, vol. 11, pp. 414–416, June 2010.

[223] J. Aguado-Sierra, A. Krishnamurthy, C. Villongco, J. Chuang, E. Howard, M. J. Gonzales, J. Omens, D. E. Krummen, S. Narayan, R. C. Kerckhoffs, and A. D. McCulloch, "Patient-Specific Modeling of Dyssynchronous Heart Failure: A Case Study," *Progress in biophysics and molecular biology*, vol. 107, pp. 147–155, Oct. 2011.

[224] W. N. McDicken, G. R. Sutherland, C. M. Moran, and L. N. Gordon, "Colour doppler velocity imaging of the myocardium," *Ultrasound in Medicine & Biology*, vol. 18, no. 67, pp. 651–654, 1992.

[225] J. Hsieh, *Computed Tomography, Second Edition*. 1000 20th Street, Bellingham, WA 98227-0010 USA: SPIE, Oct. 2009.

[226] G. S. Hurlock, H. Higashino, and T. Mochizuki, "History of cardiac computed tomography: single to 320-detector row multislice computed tomography," *The International Journal of Cardiovascular Imaging*, vol. 25 Suppl 1, pp. 31–42, Apr. 2009.

[227] H. Dalen, A. Thorstensen, S. A. Aase, C. B. Ingul, H. Torp, L. J. Vatten, and A. Stoylen, "Segmental and global longitudinal strain and strain rate based on echocardiography of 1266 healthy individuals: the

HUNT study in Norway," *European Journal of Echocardiography: The Journal of the Working Group on Echocardiography of the European Society of Cardiology*, vol. 11, pp. 176–183, Mar. 2010.

[228] H. Dalen, A. Thorstensen, L. J. Vatten, S. A. Aase, and A. Stoylen, "Reference Values and Distribution of Conventional Echocardiographic Doppler Measures and Longitudinal Tissue Doppler Velocities in a Population Free From Cardiovascular DiseaseClinical Perspective," *Circulation: Cardiovascular Imaging*, vol. 3, pp. 614–622, Sept. 2010.

[229] S. M. Lorch, A. Ludomirsky, and G. K. Singh, "Maturational and growth-related changes in left ventricular longitudinal strain and strain rate measured by two-dimensional speckle tracking echocardiography in healthy pediatric population," *Journal of the American Society of Echocardiography: Official Publication of the American Society of Echocardiography*, vol. 21, pp. 1207–1215, Nov. 2008.

[230] T. Yingchoncharoen, S. Agarwal, Z. B. Popovi, and T. H. Marwick, "Normal ranges of left ventricular strain: a meta-analysis," *Journal of the American Society of Echocardiography: Official Publication of the American Society of Echocardiography*, vol. 26, pp. 185–191, Feb. 2013.

[231] S. A. Kleijn, N. G. Pandian, J. D. Thomas, L. Perez de Isla, O. Kamp, M. Zuber, P. Nihoyannopoulos, T. Forster, H.-J. Nesser, A. Geibel, W. Gorissen, and J. L. Zamorano, "Normal reference values of left ventricular strain using three-dimensional speckle tracking echocardiography: results from a multicentre study," *European Heart Journal Cardiovascular Imaging*, vol. 16, pp. 410–416, Apr. 2015.

[232] C. Petitjean, N. Rougon, and P. Cluzel, "Assessment of myocardial function: a review of quantification methods and results using tagged MRI," *Journal of cardiovascular magnetic resonance: official journal of*

the Society for Cardiovascular Magnetic Resonance, vol. 7, no. 2, pp. 501–516, 2005.

[233] D. Augustine, A. J. Lewandowski, M. Lazdam, A. Rai, J. Francis, S. Myerson, A. Noble, H. Becher, S. Neubauer, S. E. Petersen, and P. Leeson, "Global and regional left ventricular myocardial deformation measures by magnetic resonance feature tracking in healthy volunteers: comparison with tagging and relevance of gender," *Journal of Cardiovascular Magnetic Resonance*, vol. 15, p. 8, Jan. 2013.

[234] R. J. Taylor, W. E. Moody, F. Umar, N. C. Edwards, T. J. Taylor, B. Stegemann, J. N. Townend, K. N. Hor, R. P. Steeds, W. Mazur, and F. Leyva, "Myocardial strain measurement with feature-tracking cardiovascular magnetic resonance: normal values," *European Heart Journal Cardiovascular Imaging*, Feb. 2015.

[235] B. P. Cupps, A. K. Taggar, L. M. Reynolds, J. S. Lawton, and M. K. Pasque, "Regional myocardial contractile function: multiparametric strain mapping," *Interactive CardioVascular and Thoracic Surgery*, vol. 10, pp. 953–957, June 2010.

[236] I. Del-Canto, M. P. Lpez-Lereu, J. V. Monmeneu, P. Croisille, P. Clarysse, F. J. Chorro, V. Bod, and D. Moratal, "Characterization of normal regional myocardial function by MRI cardiac tagging," *Journal of Magnetic Resonance Imaging*, pp. n/a–n/a, Dec. 2013.

[237] J. P. A. Kuijer, J. T. Marcus, M. J. W. Gtte, A. C. v. Rossum, and R. M. Heethaar, "Three-Dimensional Myocardial Strains at End-Systole and During Diastole in the Left Ventricle of Normal Humans," July 2009.

[238] J. S. Lawton, B. P. Cupps, A. K. Knutsen, N. Ma, B. D. Brady, L. M. Reynolds, and M. K. Pasque, "Magnetic resonance imaging detects

significant sex differences in human myocardial strain," *BioMedical Engineering OnLine*, vol. 10, p. 76, Aug. 2011.

[239] C. A. Miller, A. Borg, D. Clark, C. D. Steadman, G. P. McCann, P. Clarysse, P. Croisille, and M. Schmitt, "Comparison of local sine wave modeling with harmonic phase analysis for the assessment of myocardial strain," *Journal of Magnetic Resonance Imaging*, vol. 38, pp. 320–328, Aug. 2013.

[240] J. Bogaert and F. E. Rademakers, "Regional nonuniformity of normal adult human left ventricle," *American journal of physiology. Heart and circulatory physiology*, vol. 280, pp. H610–620, Feb. 2001.

[241] M.-Y. Jeung, P. Germain, P. Croisille, S. E. ghannudi, C. Roy, and A. Gangi, "Myocardial Tagging with MR Imaging: Overview of Normal and Pathologic Findings," *Radiographics*, vol. 32, pp. 1381–1398, Sept. 2012.

[242] A. A. Young, C. M. Kramer, V. A. Ferrari, L. Axel, and N. Reichek, "Three-dimensional left ventricular deformation in hypertrophic cardiomyopathy," *Circulation*, vol. 90, pp. 854–867, Aug. 1994.

[243] E. Castillo, N. F. Osman, B. D. Rosen, I. El-Shehaby, L. Pan, M. Jerosch-Herold, S. Lai, D. A. Bluemke, and J. A. C. Lima, "Quantitative Assessment of Regional Myocardial Function with MR-Tagging in a Multi-Center Study: Interobserver and Intraobserver Agreement of Fast Strain Analysis with Harmonic Phase (HARP) MRI," July 2009.

[244] C. G. Fonseca, H. C. Oxenham, B. R. Cowan, C. J. Occleshaw, and A. A. Young, "Aging alters patterns of regional nonuniformity in LV strain relaxation: a 3-D MR tissue tagging study," *American journal of*

physiology. Heart and circulatory physiology, vol. 285, pp. H621–630, Aug. 2003.

[245] H. C. Oxenham, A. A. Young, B. R. Cowan, T. L. Gentles, C. J. Occleshaw, C. G. Fonseca, R. N. Doughty, and N. Sharpe, "Age-related changes in myocardial relaxation using three-dimensional tagged magnetic resonance imaging," *Journal of cardiovascular magnetic resonance: official journal of the Society for Cardiovascular Magnetic Resonance*, vol. 5, pp. 421–430, July 2003.

[246] D. J. Brenner and E. J. Hall, "Computed Tomography An Increasing Source of Radiation Exposure," *New England Journal of Medicine*, vol. 357, pp. 2277–2284, Nov. 2007.

[247] UNSCEAR, *Effects of Ionizing Radiation: UNSCEAR 2006 Report to the General Assembly, with Scientific Annexes*. United Nations Publications, 2009.

[248] A. Sodickson, P. F. Baeyens, K. P. Andriole, L. M. Prevedello, R. D. Nawfel, R. Hanson, and R. Khorasani, "Recurrent CT, Cumulative Radiation Exposure, and Associated Radiation-induced Cancer Risks from CT of Adults," *Radiology*, vol. 251, pp. 175–184, Apr. 2009.